Strongly Correlated Systems: Transport, Entanglement, and Dynamics

DISSERTATION

zur Erlangung des akademischen Grades

Doctor of Philosophy
(Ph.D.)

vorgelegt

dem Bereich Mathematik und Naturwissenschaften
der Technischen Universität Dresden

von

YOUNES JAVANMARD

Max-Planck-Institut für Physik komplexer Systeme
Condensed Matter Physics

Die Dissertation wurde in der Zeit von Oct/2013 bis Aug/2018 angefertigt.

TECHNISCHE UNIVERSITÄT DRESDEN

mpipks

Acknowledgment:

I would like to thank Max Planck Institute for my solid academic training.

I would like to express my gratitude to Prof. Roderich Mössner for the strong support, freedom to pursue various projects and the insightful discussions during research.

I would like to express my sincere gratitude to my advisor, Prof. Jens H. Bardarson, for his support, patience, and encouragement throughout my graduate studies. It is not often that one finds an advisor and friend that always finds the time for listening to the little problems and roadblocks that unavoidably crop up in the course of performing research. His technical and editorial advice was essential to the completion of this dissertation and has taught me innumerable lessons and insights on the workings of academic research in general.

I am very grateful to Prof. Markus Heyl for his great scientific advice and knowledge and many insightful discussions and suggestions. He is one of my primary resource for getting my science questions answered.

I would like to thank Prof. Stefan Kirchner for all his help and guidance that he has gaven me in the beginning of my PhD study.

I would especially like to thank my parents and my family for the love, support, and constant encouragement I have gotten over the years.

I also thank my friends (too many to list here but you know who you are!) for providing support and friendship that I needed.

Abstract

Strongly correlated systems, i.e., quantum materials for which the interactions between its constituents are strong, are good candidates for the development of applications based on quantum-mechanical principles, such as quantum computers. Two paradigmatic models of strongly correlated systems are heavy-fermionic systems and one-dimensional spin-$\frac{1}{2}$ systems, with and without quenched disorder. In the past decade, improvement in computational methods and a vast enhancement in computational power has made it possible to study these systems in a a non-perturbative manner. In this thesis we present state-of-the-art numerical methods to investigate the properties of strongly correlated systems, and we apply these methods to solve a couple of selected problems in quantum condensed matter theory.

We start by revisiting the phase diagram of the Falicov-Kimball model on the square lattice which can be considered as a heavy-fermionic systems. This model describes an interplay between conduction electrons and heavy electrons and reveals several distinct metal-insulator phase transitions. Using a lattice Monte-Carlo method, we study the transport properties of the model. Our analysis describes the role of temperature and interaction strength on the metal-insulator phase transitions in the Falicov-Kimball model.

The second part of the thesis investigate the spatial structure of the entanglement in ground and thermal statesof the transverse-field Ising chain. We use the logarithmic negativity as a measure for the entanglement between two disjoint blocks. We investigate how logarithmic negativity depends on the spatial separation between two blocks, which can be viewed as the entanglement analog of a spatial correlation function. We find sharp entanglement thresholds at a critical distance beyond which the logarithmic negativity vanishes exactly and thus the two blocks become unentangled. Our results hold even in the presence of long-ranged quantum correlations, i.e., at the system's quantum critical point. Using Time-Evolving Block Decimation (TEBD), we explore this feature as a function of temperature and size of the two blocks. We present a simple model to describe our numerical observations.

In the last part of this thesis, we introduce an order parameter for a many-body localized spin-glass (MBL-SG) phase. We show that many-body localized spin-glass order can also be detected from two-site reduced density matrices, which we use to construct an eigenstate spin-glass order parameter. We find that this eigenstate spin-glass order parameter captures spin-glass phases in random Ising chains, both in many-body eigenstates as well as in the nonequilibrium dynamics, from a local in time measurement. We discuss how our results can be used to observe MBL-SG order within current experiments in Rydberg atoms and trapped ion systems.

Contents

Chapter 1

Introduction

1.1 Collective phenomena

Nature provides us with plenty of collective phenomenon in essentially every aspect of our everyday life. For instance, we are used to the fact that matter (a system of many particles) can organize itself into a variety of *phases* with different degrees of order. Each of these ordered states constitutes a collective behavior of many particles. These phases can transform to other phases through a so-called phase transition. The understanding of these states enables us to predict and control several properties that a material in a given phase will have. This understanding, therefore, is the base of the most important technological advancements achieved in the last century. Therefore, at the heart of condensed matter physics is the necessity to understand how to cope with systems consisting of many (more than three) interacting particles, for which exact calculations become impractical. The emergence of many-body effects gives rise to many of the collective phenomena which are the result of electron correlations – when each electron's view of its surroundings is influenced by the presence of other electrons. To understand and manipulate such phenomena is the challenge faced by condensed matter physicists.

A general criterion for the phenomena of ordering in matter was first formulated by L. D. Landau who recognized that *symmetries* can be used to characterize phases of a system[1, 2]. This constituted the first modern theory for phase transitions. Based on this, a successful program followed over several decades which consisted of the proposal of specific models (simple enough for us to perform calculations/simulations) and the explicit investigation of how the phenomena of phase transitions according to Landau's criterion is captured by them.

Depending on the nature of the phase transition, the transitions come in two types: *classical* and *quantum*[2, 3, 4].

1.1.1 Classical phase transitions

Classical Phase transitions (CPT), also called thermal phase transitions, are characterized by cusp in the thermodynamic properties of a system. The interplay between the energy of a system and the entropy of its thermal fluctuations will lead to a CPT. In 1933, Paul Ehrenfest introduced the first classification of of phase transitions on the basis of jumps in derivatives of the thermodynamic free energy with respect to

other thermodynamic variables. Although Ehrenfest's classification has been found to be an incomplete method of classifying phase transitions, it was the starting point.

There are two types of phase transition that are important in condensed matter physics: *first order (discontinuous)* and *second order (continuous)*[2, 4, 5].

First-order phase transitions exhibit a discontinuity in the first derivative of the free energy with respect to some thermodynamic variable. During the transition, the system undergoes a latent heat, which means the system either absorbs or releases a fixed (and typically large) amount of energy per volume. In this process, the temperature of the system will stay constant as heat is added and the system is in a *coexistence-phase regime* in which some parts of the system have completed the transition and others have not.

Second-order phase transitions (continuous phase transition) are continuous in the first derivative but exhibit discontinuity in a second derivative of the free energy. A continuous phase transition can usually be characterized by an order parameter[1], a concept first introduced by Landau. An order parameter is a quantity[2] that is zero in one phase, *unordered phase*, and non-zero and non-unique in the other *ordered* phase. For instance, the magnetization can be considered the order parameter at a ferromagnetic-paramagnetic phase transition. Note that finding an appropriate order parameter can be a complicated problem by itself.

The critical behavior at a phase transition is completely characterized by the set of critical exponents. One of the features of continuous phase transitions is universality, i.e., the critical exponents are the same for entire classes of phase transitions which may occur in very different physical systems. For example in chapter 3, the Falicov Kimball model has the same universality class as the classical Ising model at strong interaction limits. The associated exponents are characteristic for the continuous phase transitions regardless of being classical or quantum.

Important quantity that grows to infinity at the transition is the correlation length ξ. It quantifies the correlations between spatially separated parts of the system.

In the vicinity of criticality for both classical and quantum cases we have

$$\xi = t^{-\nu}, \tag{1.1}$$

where ν is the correlation length critical exponent and t is the dimensionless distance from the critical point. For CPT, t is the reduced temperature $t = |T - T_c|/T_c$.

1.1.2 Quantum phase transitions

Quantum phase transitions (QPT) occur when a system changes its state of matter at zero temperature due to quantum fluctuations (compared to thermal fluctuations in CPT). Such a QPT influences large area of the phase diagram, as compared with thermal fluctuations. The generic phase diagram for QPT is depicted in Fig. 1.1[2]. Such states of matter can be characterized by an order parameter. Often, we are

[1] One can also define a order parameter for a first order phase transition

[2] It can be a thermodynamic quanity

interested in the continuous quantum phase transitions where the order parameter vanishes continuously upon approaching the QPT from the ordered side[2, 4]. In this case, the transition is called quantum critical since a number of physical quantities diverge at the critical point in a power-law fashion. Often there are many competing interactions (repulsive or attractive) in the vicinity of a quantum critical point so that tiny change in the control parameter will favor one type of order over another. Since QPT happens at zero temperature and system is at its ground state, one might think that such phase transitions are not relevant to the real world. However one should note that many finite temperature properties of a system can be explained by understanding its quantum critical point (QCP). A QCP is a point at which the ground state energy of the system is a non-analytic function of some parameter which is different from temperature. For example in the case of the transverse field Ising model (TFIM) with nearest neighbour interaction,

$$\mathcal{H}_{TFIM} = -\frac{1}{2}\sum_i (J\sigma_i^x\sigma_{i+1}^x + g\sigma_i^z), \tag{1.2}$$

this parameter is the transverse field g. For TFIM at QCP, the the energy difference Δ between the ground state and the first excited state (known as the energy gap) vanishes. When g in the Hamiltonian of the system increases from zero, Δ decreases till it vanishes at the QCP as

$$\Delta \propto |g - g_c|^{\nu z}, \tag{1.3}$$

where ν and z are the critical exponents related to the QCP. This means that system is gapless at QCP. Fig. 1.1 describes the generic phase diagram of a quantum phase transition and also a classical phase transition. In the table 1.1, one can see the critical behaviour and corresponding critical exponents of CPT and QPT.

1.2 Strongly correlated systems

The physical systems which are well understood are those systems that can be modeled with ensemble of free particles. For example semiconductors and most metals can be described as having non-interacting electrons. This is because the interaction (Coulomb) energy of electrons is much smaller than their kinetic energy. However, there are important class of systems so called *strongly correlated systems* for which the interactions between particles are not weak. These interactions play a an important role in the properties of such systems and therefore these interactions should be taking into account.

Lattice models of correlated fermions appear in a wide variety of physical systems, from condensed matter, where they are used to study low-temperatures models of, e.g., transition metals and intermetallic rare earth and actinide compounds, to quantum chemistry and so on. Many of these systems exhibit a number of phases that arise out of the competition between different degrees of freedom which finally

TABLE 1.1: Different critical exponents in classical and quantum phase transitions.

CPT	**QPT**
$\langle\phi(\vec{x})\rangle \begin{cases} \sim (T_c - T)^{\beta} & \text{for } T < T_c \ \& \ (T \to T_c^-) \\ = 0 & \text{for } T \geq T_c \end{cases}$ with $\langle\phi(\vec{x})\rangle$ as thermal expectation value of the ordered parameter	$\phi \begin{cases} \sim (g_c - g)^{\beta} & \text{for } g < g_c \ \& \ (g \to g_c^-) \\ = 0 & \text{for } g \geq g_c \end{cases}$
$\xi \sim (T - T_c)^{-\nu}$ with ν for correlation length exponent	$\xi \sim (g - g_c)^{-\nu}$
two-point correlation function $\langle\phi(\vec{x}_1)\phi(\vec{x}_2)\rangle \sim e^{-\lvert\vec{x}_1 - \vec{x}_2\rvert/\xi}$ for $T \geq T_c$ at large distances	equal-time connected correlation function $G(r) = \langle\phi(0,t)\phi(r,t)\rangle - \langle\phi(0,t)\rangle\langle\phi(r,t)\rangle \sim \frac{e^{-r/\xi}}{r^{d-2+\eta}}$
$C_v \sim (T - T_c)^{-\alpha}$ The specific heat diverges as $T \to T_c^+$	$C_v \sim (g - g_c)^{-\alpha}$ as $g \to g_c^+$
$\chi = \lim_{h\to 0} \frac{d\langle\phi(\vec{x})\rangle}{dh} \sim (T - T_c)^{-\gamma}$ The zero field susceptibility diverges as $T \to T_c^+$ (response of the system to external field)	$\chi \sim (g - g_c)^{-\gamma}$
In the external field h, $\langle\phi(\vec{x})\rangle \sim \lvert h\rvert^{1/\delta}$ exactly at $T = T_c$ as $h \to 0$	$\phi \sim \lvert g_L\rvert^{1/\delta}$ for $g_L \to 0$ and $g = g_c$ with g_L as a longitudinal field
two-point correlation function $\langle\phi(\vec{x}_1)\phi(\vec{x}_2)\rangle \sim \lvert\vec{x}_1 - \vec{x}_2\rvert^{-(d-2+\eta)}$ exactly at $T = T_c$ at large distances	$G(r) \sim \lvert r\rvert^{-d+2-\eta}$ at $g = g_c$
dynamical critical exponent z $\xi_\tau \propto \xi^z$ as $T \to T_c^+$ with τ as response time (response of the system to a time-dependent filed)	$\xi_\tau \sim \xi^z \sim \lvert g - g_c\rvert^{-\nu z}$

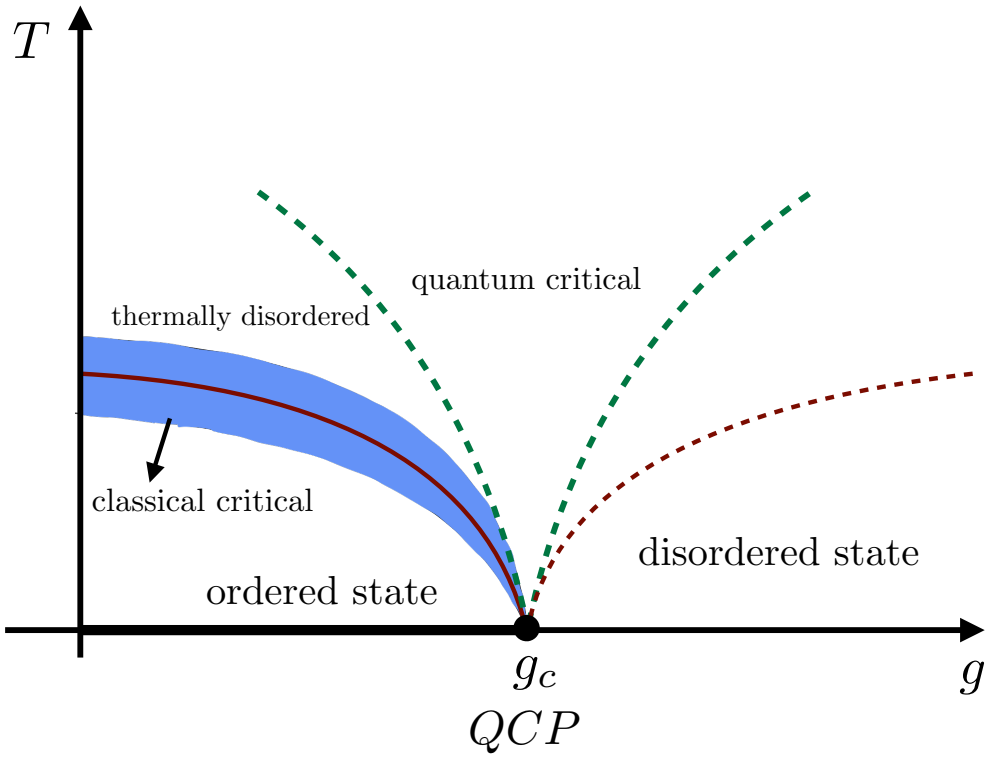

FIGURE 1.1: Phase diagram of a general quantum phase transition (QPT).

can lead to a phase transition. Understanding the possible orders that characterize these phases is of primary interest in current many-body physics.

The two classes of strongly correlated systems that interest us are heavy fermionic (electronic) systems and one-dimensional spin-$\frac{1}{2}$ systems in presence and absence of disorder.

Heavy-electron materials are a subset of the intermetallic compounds containing elements with localized electrons. Historically, the term Heavy-fermion was first used by Steglich and his collaborators in the late 1970's[6]. A heavy fermion metal can develop electron masses (density of states) 1000 times bigger than copper. It can also develop unconventional superconductivity, transform into new forms of quantum order, exhibit quantum critical and topological behavior. In the periodic table, the most strongly interacting electrons reside in orbitals that are well localized. In order of increasing localization, partially filled orbitals are ordered as following[7, 8]

$$5d < 4d < 3d < 5f < 4f \tag{1.4}$$

In the present thesis, we select and study some of the collective phenomena in the systems of many-body condensed matter physics which their components are strongly correlated with each other. First, we introduce these phenomena and later we give a short survey on these phases and systems.

1.2.1 Metal-insulator transitions

One interesting class of quantum phase transitions is metal-insulator transitions[9, 10]. They usually originates from two effects

- lattice effects for models of non-interacting electrons
- the interaction between electrons

At the metal-insulator transitions, the conductivity vanishes

$$\sigma = (\frac{\partial n}{\partial \mu})D \to 0 \tag{1.5}$$

Two examples are the *Anderson transition* (Anderson localization) which is due to lattice effects in a model of non-interacting electrons and *Mott transitions* which is due to the interaction between electrons. In Anderson transitions, the electronic charge diffusivity D is driven to zero by quenched disorder while in the Mott transition the thermodynamic density susceptibility $\partial n/\partial \mu$ vanishes. Note that a sharp distinction between metal and insulator is possible only at $T = 0$.

Another metal-insulator transition which has recently attracted great attention is the *many-body localization* (MBL) transition. This phenomena occurs for a closed quantum system and is due to the presence of the interaction among electrons in the Anderson localization [11].

In this thesis, we deal with several Metal-Insulator transitions in strongly correlated systems. Therefore in the following, we present a short introduction to the above phenomena.

Mott transition

The band theory of solids provides a successful description of metals, insulators and their transitions. After the discovery of quantum mechanics, physicists could give a basic distinction between metals and insulators based on their band structures.

However in 1937, several simple transition-metal oxides with a partially filled d-electron band were found to be insulators. In this class of materials, the strong Coulomb repulsion between electrons (electron-electron interactions) is the source of the unusual insulating behavior called Mott insulator [12, 13]. In other words, under strong on-site interaction U, the original band will split into two bands with energy gap U and due to this, the system will become an insulator.

The transition from a metal to an insulator due to strong electron-electron interactions is called a Mott transition[14]. In this transition, the electronic state will

change. In the vicinity of the Mott transition, a wide variety of interesting phenomena, such as high-temperature superconductivity and large thermoelectric effects, arise due to the interplay between charges, spins, and orbital degrees of freedom.

Before explaining the other two types of metal-insulator transitions, we give a short introduction to some concepts that are required to underestand these transitions.

1.2.2 Close quantum system

Consider a closed many-body quantum system with a short-ranged Hamiltonian $\mathcal{H}$, which means that the Hamiltonian is local in real space. Such a system can consist of cold atoms, traped ions, photons, electrons, spins, qubits etc. The states of such a system can be studied using density matrices. We work in the Schrödinger representation, where the density operator $\rho(t)$ evolves in time according to

$$\begin{aligned} \rho(t) &= e^{\frac{-i\mathcal{H}t}{\hbar}}\rho(0)e^{\frac{i\mathcal{H}t}{\hbar}}, \\ i\hbar\frac{d\rho(t)}{dt} &= [\mathcal{H}(t),\rho(t)], \\ \mathrm{Tr}\{\rho\} &= 1. \end{aligned} \tag{1.6}$$

One can compute the expectation value of an operator corresponding to an operator $\hat{O}$ as $\langle\hat{O}\rangle_t = \mathrm{Tr}\left\{\hat{O}\rho(t)\right\}$. The systems that we study are the quantum spin$-1/2$ systems which can be considered as a special case of general quantum two-state systems. Each spin is located at a point in real space which can be randomly located or form a specific configuration. Such quantum spin system can be described by four linearly independent operators. In the case of spin$-1/2$ systems these operatores can be represented by 2×2 matrices: the identity matrix $\mathbb{I}_i$ and the three Pauli matrices σ_i^x, σ_i^y, σ_i^z for spin at site i. A general mixed state ρ_i can be written as a linear combination of these operators as will be mentioned in Eq. 4.29 in section 4.7. The Hamiltonian of the system is a sum of local operators. The system may have some other extensive conserved quantities that are also sums of local operators. Spin and particle are examples for these conserved quantities. Such quantities can be transported by the systems dynamics such as the energy. these dynamics are governed by the Hamiltonian of the system as shown Eq. 1.6. Two cases are very interesting

- time independent Hamiltonian $H(t) = H$

$$U(t) = \exp(-iHt), \tag{1.7}$$

  with $U(t)$ being the time evolution operator associated with the Hamiltonian of the systems H.

- Floquet systems (periodically driven systems) $H(t) = H(t+T)$ and one can use the general definition of unitary time evolution to compute $U(t)$

$$U(t) = Te^{-\int_0^t H(\tau)d\tau}. \tag{1.8}$$

  where T is the time-ordering operator.

Note that the off-diagonal terms of the density matrix $\rho(t)$ give rise to the system dynamics in the eigenbasis of the Hamiltonian. In other words if the $\rho(t)$ is one of the eigenstates of the Hamiltonian, then the problem it trivial, because there is no dynamics.

1.2.3 Non-equilibrium dynamics of isolated quantum systems

In recent years, physicists have tried to study the non-equilibrium dynamics of isolated quantum systems. Theoretically and experimentally, it is challenging and it causes many fundamental questions in the various areas of quantum mechanics. In this thesis, non-equilibrium dynamics are investigated from a quantum quench perspective[15, 16]. Quantum quench provides a way to access the excited states of the systems which are required to study a nonequilibrium problem. This perspective is characterized by initializing the system in a state $\rho_0 = |\psi_0\rangle\langle\psi_0|$, which can be the ground state of a local Hamiltonian. Then by sudden global change of the system parameters and letting the state to be evolved in time by a unitary time evolution under some local Hamiltonian H

$$|\psi(t)\rangle = e^{-iHt}|\psi_0\rangle. \tag{1.9}$$

After the quench, the initial state changed to a different state at each time t with different properties. The expectation value of observable A at a later time t will be

$$\langle A(t)\rangle = \mathrm{Tr}(e^{-iHt}\rho_0 e^{iHt}A) \tag{1.10}$$

Non-equilibrium dynamics of closed quantum systems enable us to study and discover different features of correlated systems in order to answer fundamental questions which arise from it. There are several concepts in condensed matter and statistical physics that one can use non-equilibrium dynamics to understand, for example, thermalization, transport, entanglement, dynamics of quantum phase transition and so on. But in this thesis, we use quantum quench in the context of many-body localizations and will visit and study the localized phase where it hosts another interesting phase called spin-glass phase.

In the following, we explain some of the concepts that non-equilibrium dynamics of a quantum system can enable us to study.

1.2.4 Quantum thermalization

A usual quantum statistical mechanical assumption is that the system goes to thermal equilibrium in the long time limit, i.e., $t \to \infty$. This (quantum) system in thermal equilibrium is fully characterized by a small number of parameters (temperature, chemical potential, etc.: one parameter for each extensive conserved quantity), suggesting that the process of going to thermal equilibrium is associated with the erasure of the system's memory of all other details about its initial state. This means that one can wait long enough time such that the system is in thermal equilibrium and then by usuing equilibrium statistical mechanics, study the behaviour of the system without solving the dynamics. When such a situation happens the system is a *bath* to itself and brings the subsystems to thermal equilibrium. However this assumption is not true for MBL phases. This requires a more precise definition of thermalization.

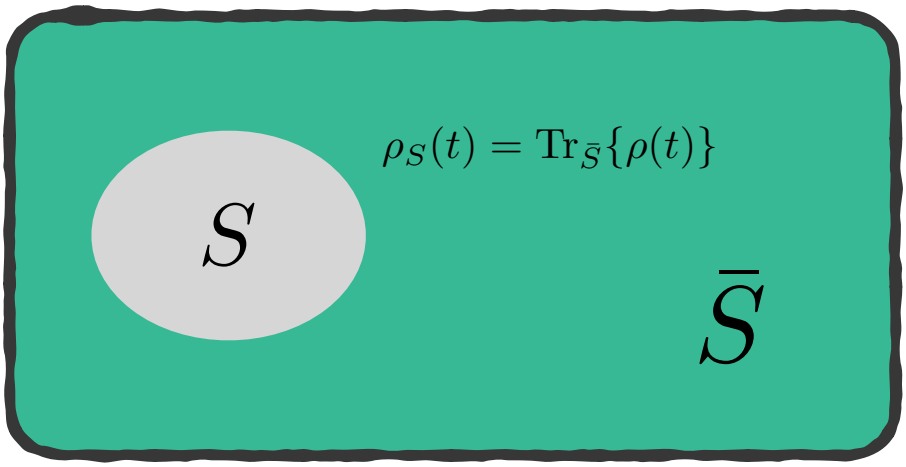

FIGURE 1.2: Statistical mechanics of a closed quantum system undergoing unitary time evolution. There is no external reservoir. It can be useful to partition the closed quantum system into a S subsystem and its environment. If the system quantum thermalizes, then $\bar{S}$ is able to act as a bath for the subsystem S. S defined by a finite set of microscopic degrees of freedom and the $\bar{S}$ is the rest of the system such that $\rho_S(t) = \mathrm{Tr}_{\bar{S}}\{\rho(t)\}$.

To define quantum thermalization, we consider the exact dynamic of the closed quantum system which is given by unitary time evolution of the system

$$\rho(t) = U(t)\rho(0)U^{\dagger}(t). \tag{1.11}$$

The dynamics in Eq. 1.11 is reversible which means that any information that is in the initial state is still present at time t but hidden. The full system does not

forget about its initial state. Thus the state of the full system does not go to the one of thermal equilibrium distributions and consequently does not thermalize. The dynamics of the system in the basis of U's eigenstates is trivial. The only thing that happens is that each off-diagonal term of ρ picks up a phase

$$\begin{aligned} \rho_{n,n}(t) &= \rho_{n,n}(0) \\ \rho_{n,m}(t) &= e^{i(\phi_n - \phi_m)}\rho_{n,m}(0). \end{aligned} \tag{1.12}$$

As the conclusion of this section one can say that *thermalization is of subsystems* which means the system goes to thermal equilibrium for $T \to \infty$ such that the state of its subsystem goes to thermal equilibrium as it is shown in Fig. 1.2.

Now we can have a more precise definition of thermalization such that holds for large number of systems as follows

For all subsystems S and all initial states $\rho(0)$, we have

$$\lim_{\substack{\bar{S}\to\infty \\ t\to\infty}} \rho_S(t) = \rho_S^{(eq)}(T,\mu,h,\ldots) \equiv \mathrm{Tr}_{\bar{S}}\left(\frac{e^{-\beta(\mathcal{H}-\mu N+\ldots)}}{\mathcal{Z}}\right), \tag{1.13}$$

where $\rho_S^{(eq)}(T,\mu,h,\ldots)$ is the state of the subsystem at thermal equilibrium which can depend on temperature T, chemical potential μ, field h and so on.

1.2.5 The Eigenstate Thermalization Hypothesis

According to the Eigenstate Thermalization Hypothesis (ETH), thermalization occurs at the level of individual eigenstates of a given Hamiltonian, which means each eigenstate of the Hamiltonian implicitly contains a thermal state[17, 18]. If we look at one eigenstate of the Hamiltonian

$$\mathcal{H}|E_n\rangle = E_n|E_n\rangle, \tag{1.14}$$

where E_n is the thermal equilibrium energy corresponds to temperature T_n, such that $E_n = \langle H\rangle_{T_n}$ is the expectation value of the Hamiltonian at the single eigenstate $|E_n\rangle$. Imagine the full system is in this eigenstate, thus

$$\begin{aligned} \rho = \rho^{(n)} &= |E_n\rangle\langle E_n|, \\ \rho_S^{(n)} &= \mathrm{Tr}_{\bar{S}}\{|E_n\rangle\langle E_n|\}, \end{aligned} \tag{1.15}$$

where $\rho_S^{(n)}$ is the state of the subsystem S. Based on the ETH, sub-system S is at thermal equilibrium in the thermodynamic limit

$$\rho_S^{(n)} = \rho_S^{(eq)}(T_n). \tag{1.16}$$

The ETH can provide a new set of ensembles in quantum statistical mechanics, namely the single-eigenstate ensemble, that each contains of a single eigenstate of the full system Hamiltonian. When ETH holds then these ensembles all give the correct thermal equilibrium characteristic of the subsystem. To describe this clearly, consider a typical pure state, when it is restricted to a small subsystem, is well approximated by the microcanonical ensemble [19, 20, 21, 22]. In other words, for a system contains of a sufficiently small subsystem S and its complement $\bar{S}$, for any random pure state Ψ from an energy shell $(E, E + \Delta E)$

$$|\Psi\rangle = \sum_a E_n |E_n\rangle, \quad E_n \in (E, E + \Delta E), \tag{1.17}$$

the corresponding reduced density matrix $\rho_\Psi^{(S)} = \mathrm{Tr}_{\bar{S}} |\Psi\rangle\langle\Psi|$ can be considered microcanonical with some approximation[22]. Now in the limit of very small energy window $\Delta E \to 0$, this microcanoical ensemble reduces to a microcanonical ensemble which consisting only one eigenstate and therefore single-eigenstate ensemble and consquently we have Eq. (1.16).

1.2.6 Anderson localization

The study of the conductance of electrons is at the very heart of condensed-matter physics. The classical Drude theory of electronic conductivity is based on the idea of free electrons scattered by positive ions in metal lattice sites. A key concept in this description is the mean free path, i.e., the average length an electron travels before it collides with an ion. According to classical theory, the electronic conductivity should be directly proportional to the mean free path, which experiment has shown is large in metal (around 100 nm). This means that the mean free path can be several orders of magnitude larger than the lattice constant.

Physicists had to wait for the discovery of quantum mechanics to understand why electrons apparently do not scatter from ions that occupy regular lattice sites: the wave character of an electron causes the electron to diffract from an ideal crystal. Resistance appears only when electrons scatter from imperfections (disorder) in the crystal. With the quantum mechanical revision, the Drude model can still be used, but in the new picture an electron is considered as zigzagging between impurities or disorder. The stronger the disorder, the smaller the mean free path and the lower the conductivity. Increasing the disorder in a metal will eventually turn it to an insulator in which the extended states of a metal become localized and the conductivity vanishes. This will lead to the phenomena of disorder-induced spatial localization of electrons or Anderson localization[23].

In 1958, Anderson considered the behaviour of electrons in a dirty crystal. This is the quantum mechanical analogue of a random walk in a random environment. Random potential produced by disorder in a lattice of correlated electrons can lead to localization of electrons by disorder. The phenomena of Anderson localization can be considered as one of the most fundamental disorder-related phenomenon.

Fig. 1.3 explains the pictural representation of the phenomena of Anderson localization.

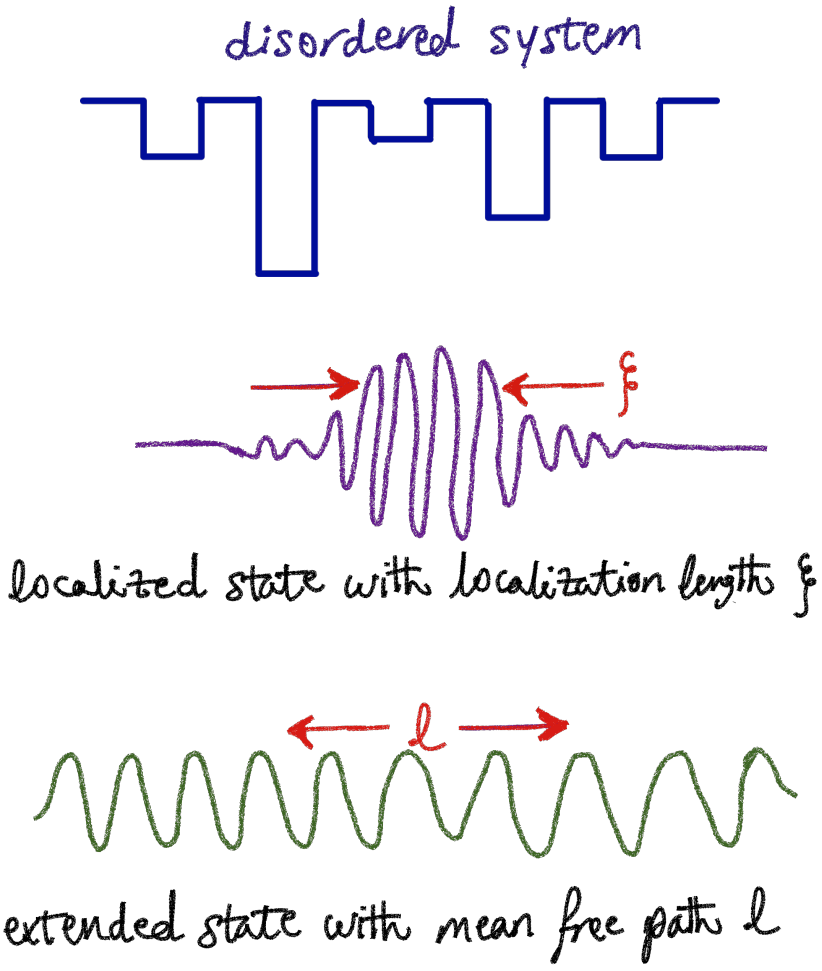

FIGURE 1.3: pictural representation of the Anderson Localization: localization length ξ and mean free path ℓ.

Anderson considered the tight-binding approximation in which the electrons can hop between atoms (lattice sites), and these electrons are subject to an external random potential which models the random environment. As a consequence, in strong enough disorder, such a system should lose all its conductivity properties and become an insulator. This means that electrons in such a system are trapped due to existence of disorder which is in contrast to the behaviour in ideal crystals which are conductors.

As we mentioned above, the model that explain Anderson localization, is a tight-binding model of a single quantum particle (electron) hopping on an infinite lattice

with Hamiltonian

$$H = t \sum_{\langle i,j \rangle} (c_i^\dagger c_j + c_j^\dagger c_i) + \sum_i U_i c_i^\dagger c_i, \tag{1.18}$$

where U_i is a static random onsite potential, t is the hopping parameter between nearest-neighbor sites. $c_i^\dagger$ is creation operator for the particle at site i. For weak-disorder, the eigenstate of this Hamiltonian can be extended over all the sites and particle shows diffusive dynamics. For strong eough disorder, the particle's wave-function get localized and it will be characterize by an exponentially decaying function as

$$|\psi_\alpha(\vec{r})| \sim \exp(|\vec{r} - \vec{r}_\alpha| / \xi) \tag{1.19}$$

where ξ is the localization length which is dependent on the disorder strength and the energy. This means that the state of α of the particle is localized around the position $\vec{r}_\alpha$. In other words the electronic wave function $\psi(\vec{r})$ will have interference with itself such that it will be confined to a small part of the solid and subsequentally the state of the matter is an insulator and does not conduct. In one dimension an arbitrary weak disorder localizes all states[10].

The phenomenta of the Anderson localization can manifest in different systems of correlated fermions. For instance in the Falicov-Kimball model which explains a system of heavy-fermion compounds where the f-electrons hybridize with the conduction electrons. The effective masses of the resulting quasiparticles can reach a thousand times the mass of the bare electron and due to this reason the f-electrons can be seen as frozen particles which don't have any dynamics and random distribution of them can produce a random potential for the c-electrons and the result can be localization of the c-electrons.

1.2.7 Many-body localization

For an isolated quantum system, Anderson localization in the presence of the interaction among particles (electron-electron interaction) will reach to the phenomena of Many-Body Localization(MBL)[11], i.e., one can look at it as an extension of single particle Anderson localization to interacting systems. In other words, MBL is a phenomena which arises from presence of both disorder and iteractions among constitued particles. The interplay between these two key ingredients addresses several fundamental questions on how a quantum system thermalizes or fails to. It is of very fundamental interest to both many-body quantum physics and statistical mechanics. MBL transition is a quantum phase transition between a localized and extended (ergodic) phase which happens at nonzero temperatures. It is a quantum *glass transition* where equilibrium quantum statistical mechanics breaks down. In the localized phase the system fails to thermally equilibrate[24]. Recent experiements on ultra-cold atoms and trapped ions enable physicists to investigate experimentally the non-equilibrium dynamics.

In this thesis we are interested in MBL in the context of spin models which is more simple. Similar the more familiar ground-state quantum phase transitions, this transition is a sharp change in the properties of the many-body eigenstates of the Hamiltonian[24, 25, 26]. The distinctions between the two phases all are due to differences in the properties of the many-body eigenstates of the Hamiltonian, which of course enter in determining the dynamics of the isolated system. In the ergodic phase, the many-body eigenstates are thermal. This means the isolated quantum system can relax to thermal equilibrium under the dynamics due to its Hamiltonian. In the thermodynamic limit ($L \to \infty$), the system thus successfully serves as its own heat bath in the ergodic phase. In a thermal eigenstate, the reduced density operator of a finite subsystem converges to the equilibrium thermal distribution for $L \to \infty$. Thus the entanglement entropy between a finite subsystem and the remainder of the system is, for $L \to \infty$, the thermal equilibrium entropy of the subsystem. At nonzero temperature, this entanglement entropy is extensive, proportional to the number of degrees of freedom in the subsystem. In the many-body localized phase , on the other hand, the many-body eigenstates are not thermal[11], i.e., ETH is false in the localized phase[27, 17, 18, 28]. Thus in the localized phase, the isolated quantum system does not relax to thermal equilibrium under the dynamics of its Hamiltonian. The infinite system fails to be a heat bath that can equilibrate itself. It is a *glass* whose local configurations at all times are set by the initial conditions. In the present thesis we are interested in the localized side of the transition where it hosts MBL spin-glass phase. In the recent years there have been many studies on MBL phase transition in both side of the transition. We can summarize both sides of the transition in the table 1.2.

1.3 Entanglement

One of the central principles of quantum mechanics is entanglement. During last years, Entanglement plays a central role in quantum many-body theory. Exotic quantum phases such as spin liquids [29, 30], topological [31, 32], or many-body localized systems [33, 34, 35, 36] find their characterization in their entanglement properties. Moreover, quantum phase transitions are signaled by a universal entanglement contribution determined solely by the universality class of the transition [2, 37, 38, 39, 40]. This can be used to detect quantum phase transitions without prior knowledge on the nature of the transition [41], e.g., the order parameter, since entanglement is a general system-independent quantity. In the ongoing efforts to characterize quantum many-body systems via their entanglement properties, the entanglement entropy, measuring the entanglement between a subsystem and its remainder, is taking over a key role. However, a major limitation of the entanglement entropy is that it is a valid entanglement measure only for pure states. This is a particular challenge in view of experiments where thermal excitations or other imperfections leading to mixed states are generally unavoidable. Nevertheless, recent works on quantum simulators have demonstrated that entanglement in quantum many-body systems can be accessible in experiments. In systems of trapped ions,

TABLE 1.2: properties of the two phase, i.e., ergodic or thermal and MBL phase[26].

Ergodic phase	**MBL phase**
Memory of initial conditions hidden in global operators at long times	Some memory of local initial conditions preserved in local observables at long times
Metal: finite DC conductivity	No transport: Zero DC conductivity, even at infinite temperature
Entanglement spreads fast $S(t) \propto t$	Entanglement spreads, but slowly $S(t) \propto \log(t)$
Ergodic states	**MBL states**
Follow ETH	Violate statistical Mechanics
Observables are the same within the same energy shell	Observables differ from eigenstate to eigenstate
Random matrix statistics	Integrable (Poisson) statistics
Eigenstates occupy all configuration space	No delocalization
Entanglement entropy of eigenstates is extensive, i.e., Volume Law for entanglement	Area law for entanglement

full-state tomography provides access to various entanglement measures [42, 43, 44, 45, 46, 47]. In ultra-cold atoms it is possible to measure Renyi entropies [48] as also demonstrated in experiments [49, 50]. Recent theoretical works have outlined new approaches for measuring entanglement using unitary n-designs [51, 52] or machine learning techniques [53].

1.4 Outline of the thesis

In this thesis we deal with the phenomena that we have mentioned above. We aim to address different problems and study them in some special cases using different numerical techniques. For such a systems, analytical solutions only exist for very special setups or weak and strong coupling limits. Semi-analytical infinite partial summation techniques [54] can be applied but are in general uncontrolled. Approximate numerical approaches are known to yield inaccurate critical behavior in two and three dimensions [55, 56]. Therefore, large-scale numerical efforts, e.g., diagonalization, lattice quantum Monte Carlo, large diagrammatic simulations, tensor network methods(DMRG, TEBD, MERA,...) or machine learning techniques are required to lead us to a better understanding of these models[57, 58, 59, 60, 61, 62, 63, 64].

The structure of present thesis is as follows: in chapter 2 we introduce the numerical techniques that we have used in the thesis for different problems. It starts with a brief introduction to *Exact diagonalization* methods. Afterwards we introduce our lattice monte carlo method based on metropolis algororithm to sample the different configurations in a lattice of fermionic systems and in last part of the chapter 2, we introduce the TEBD algorithm for spin chains based on matrix product states representation for both pure and mixed state (nonzero temperatures).

In chapter 3, we ain to study a heavy fermionic system and especially investigate the interplay between frozen f-electrons and conduction c-electrons. For this we revisit the phase diagram of finite temperature phase diagram of the two-dimensional Falicov-Kimball model at half-filling using state-of-the-art Lattice Monte Carlo techniques. We show that this model at particle-hole symmetry possesses three distinct thermodynamic insulating phases and exhibits Anderson localization. The previously reported metallic phase is identified as a finite-size feature due to the presence of weak localization. We characterize these phases by their electronic density of states, staggered occupation, conductivity, and the generalized inverse participation ratio. The implications of our findings for other strongly correlated systems will be discussed.

In chapter 4, we aim to map out the spatial entanglement structure of a low-dimensional quantum system, the transverse-field Ising chain, both in the ground state and in thermal states using Time-Evolving Block Decimation (TEBD). For this purpose we use the logarithmic negativity in order to obtain information about the spatial entanglement structure of two disjoint blocks of identical size ℓ. We show that for any fixed size ℓ of the two blocks there exists an entanglement threshold at a distance d^* beyond which the logarithmic negativity vanishes identically and

the two blocks become unentangled. This holds remarkably across the whole phase diagram of the system including also the quantum critical point where the system exhibits long-ranged quantum correlations. We study this entanglement threshod d^* as a function of the system parameters and temperatures.

In chapter 5, we study a specific phase inside MBL regime called MBL spin-glass phase which is challenging to detect dynamically and therefore experimentally. Using two-point reduced density matrices, we construct an eigenstate spin-glass order parameter to detect the MBL spin-glass order. We find that this eigenstate spin-glass order parameter captures spin-glass phases in random Ising chains both in many-body eigenstates as well as in the nonequilibrium dynamics from a local in time measurement.

Chapter 2

Numerical Techniques

The aim of this chapter is to provide an introduction to methods and techniques used in the numerical solution of the problems that interest us.

2.1 Exact diagonalization

The phrase exact diagonalization (ED) is a broader term and generally refers to methods which construct the basis of a given system explicitly. While the actual form of this basis can vary between methods the general scheme is to set up the Hamiltonian of the system under study explicitly and carry out calculations. In this thesis we use ED to solve the systems composed of spins on a 1D chain. In particular we use ED to compute the the eigenvalues and eigenvectors of the Hamiltonian of interest.

Two models that are frequently used as spin systems, are the XXZ model and Transverse field Ising Model. Both describe system of spins where each spin interacts with other spins through coupling coefficients that can be nearest-neighbor or other types. The Hamiltonians that describe these models in 1D are: Transverse field Ising model

$$\hat{H} = -\frac{1}{2}\left(\sum_{i}^{L-1} J_z \sigma_i^z \sigma_{i+1}^z + \sum_{i}^{L-1} J_x \sigma_i^x \sigma_{i+1}^x + \sum_{i}^{L} h_x \sigma_i^x\right), \tag{2.1}$$

where J_z is the nearest-neighbour coupling and h_x is the transverse field and J_x is the coupling in the x-direction which when it has nonzero value, makes the model nonintegrable. $\sigma_i^{n=x,yz}$ are the Pauli matrices with

$$\sigma_i^x = \begin{pmatrix} 0 & 1 \\ 1 & 0 \end{pmatrix}, \ \sigma_i^y = \begin{pmatrix} 0 & i \\ -i & 0 \end{pmatrix}, \ \sigma_i^z = \begin{pmatrix} 1 & 0 \\ 0 & -1 \end{pmatrix}. \tag{2.2}$$

For the XXZ model, the hamiltonian is

$$\hat{H} = \sum_{i}^{L-1} J\left(S_i^x S_{i+1}^x + S_i^y S_{i+1}^y\right) + \sum_{i}^{L-1} \Delta S_i^z S_{i+1}^z + \sum_{i}^{L} h_z S_i^z, \tag{2.3}$$

where J is the coupling and Δ is the anisotropy parameter. For $\Delta = 1.0$, Eq. 2.3 becomes the Heisenberg model. Note that $S_i^{n=x,y,z} = \frac{\hbar}{2}\sigma_i^{n=x,y,z}$.

The size of Hilbert space asscociated to each Hamiltonian is $D = d^L$ local Hilbert space has the dimension $d = 2$ refers to the direction of each spin, i.e., $\sigma_i = |\uparrow\rangle$ or $|\downarrow\rangle$ in the σ^z basis. Note that the basis $\{|\uparrow\rangle, |\downarrow\rangle\}$ also called computational basis. The task of diagonalization of the Hamiltonian becomes to write down the Hamiltonian of the system in the computational basis.

$$\hat{H} = \sum_{\substack{\sigma_1,\ldots,\sigma_i,\ldots\sigma_L \\ \sigma'_1,\ldots,\sigma'_i,\ldots\sigma'_L}} H^{\sigma_1,\ldots,\sigma_i,\ldots\sigma_L}_{\sigma'_1,\ldots,\sigma'_i,\ldots\sigma'_L} |\sigma_1,\ldots,\sigma_i,\ldots\sigma_L\rangle \langle\sigma'_1,\ldots,\sigma'_i,\ldots\sigma'_L| , \tag{2.4}$$

where

$$H^{\sigma_1,\ldots,\sigma_i,\ldots\sigma_L}_{\sigma'_1,\ldots,\sigma'_i,\ldots\sigma'_L} = \langle\sigma_1,\ldots,\sigma_i,\ldots\sigma_L| \hat{H} |\sigma'_1,\ldots,\sigma'_i,\ldots\sigma'_L\rangle \tag{2.5}$$

For this, one should compute each part of the Hamiltonian accurately such that it captures the effect of each site i in the Hamiltonian. For that we need to know the matrix representation of each pauli spin operator $S_i^{n=x,y,z}$ at each site i. The matrix definition for each $\hat{\sigma}_i^{n=x,y,z}$ in a $D = d^L$ space is

$$\hat{\sigma}_i^{n=x,y,z} = \underbrace{\mathbf{I}_2 \otimes \ldots \otimes \mathbf{I}_2 \otimes \hat{\sigma}^{n=x,yz} \otimes \mathbf{I}_2 \otimes \ldots \otimes \mathbf{I}_2}_{d^L \times d^L} . \tag{2.6}$$

This means the Hilbert space of a many-particle system is given by the tensor product of the single-particle Hilbert spaces. By using relation 2.6, we can construct the Hamiltonian matrix of the system, Eq. 2.5, and access its eigenvalues and eigenvectors.

2.2 Lattice Monte Carlo Method

The Monte Carlo method was first developed at Los Alamos during the WWII Manhattan project for the purposes of modeling neutron trajectories during fission. Since that time, the Monte Carlo method has undergone enormous developments and has been numerously applied in virtually every area of science and engineering. Intrinsically as a computationally very demanding method, the Monte Carlo method has naturally become more popular as computers have become faster, less expensive and more accessible.

Originally Lattice Monte Carlo (LMC) was developed for addressing multi-scale phenomenological diffusion problems [65, 66]. In this LMC method, the phenomenological diffusion problem is mapped onto a simple cubic (usually) lattice which is then explored by virtual particles. Depending on the physics of the problem considered, the virtual particles correspond to a fixed amount of matter (mass diffusion analysis), thermal energy (thermal diffusion analysis) or even elastic deformation

energy (elastic analysis)[67]. In the LMC method, geometries are discretized as lattice models. In principle, any topology of lattice can be chosen, for reasons of simplicity normally a primitive cubic arrangement is selected.

Aim of this section is to have a brief overview on the LMC method for the Falikov-Kimball Model (FKM) which will be focused in details in chapter 3. Our LMC method is based on classical Monte Carlo or more specifically Markov Chain Monte Carlo (MCMC) method−which was invented soon after ordinary Monte Carlo at Los Alamos−and consequently using the Metropolis algorithm to sample all configurations which the lattice can possess.

2.2.1 Markov Chain Monte Carlo

Before we explain (MCMC), lets have a short overview on Markov chains.

Markov Chains

A sequence $X_1, X_2, \ldots$ of random elements of some set is a Markov chain if the conditional distribution of X_{t+1} given $X_1, \ldots, X_t$, only depends on X_t. The set in which the X_t take values is called the state space of the Markov chain and follows an evolution law. Note that the index t can be viewed as a kind of discrete time.

People introduced to Markov chains through a typical course on stochastic processes have usually only seen examples where the state space is finite or countable. If the state space is finite, written $\{x_1, \ldots, x_n\}$, then the initial distribution can be associated with a vector $\lambda = (\lambda_1, \ldots, \lambda_n)$ defined by

$$\mathcal{P}_t(x_i) = \mathcal{P}(X_t = x_i) = \lambda_i, \quad i = 1, \ldots, t, \tag{2.7}$$

as the probability to find the value X_t for the random variable in the Markov chain at "time" t.

The transition probabilities can be associated with a matrix P having elements p_{ij} and $0 \leq p_{i,j} \leq 1$, defined by

$$\mathcal{P}(X_{t+1} = x_j \mid X_t = x_i) = p_{ij}, \quad i = 1, \ldots, t \ \ \& \ \ j = 1, \ldots, t. \tag{2.8}$$

and

$$\sum_{x_i} \mathcal{P}(x_i \to x_j) = 1,$$

note that the sum can be replaced by an integral if the variables are continuous.

Now one must have

$$\mathcal{P}_{t+1}(x_j) = \sum_{x_i} \mathcal{P}_t(x_i) \mathcal{P}(X_{t+1} = x_j \mid X_t = x_i) \tag{2.9}$$

A Markov chain has stationary transition probabilities (detailed balance condition) if the conditional distribution of X_{t+1} given X_t does not depend on t.

$$\mathcal{P}_t(x_j)\mathcal{P}(X_{t+1} = x_i \mid X_t = x_j) = \mathcal{P}_t(x_i)\mathcal{P}(X_{t+1} = x_j \mid X_t = x_i) \tag{2.10}$$

This condition expresses the fact that in the evolution the flow of probability going from x_i to x_j is compensated by the opposite flow. This let us expect that a steady state can easily be reached by such Markov chains. This is the main kind of Markov chain of interest in MCMC. So we will restrict to this kind of class of Markov chains.

Metropolis Algorithm

In 1953, Metropolis and colleagues (including Edward Teller) simulated a liquid in equilibrium with its gas phase. The obvious way to find out about the thermodynamic equilibrium is to simulate the dynamics of the system, and let it run until it reaches equilibrium. They realized that they did not need to simulate the exact dynamics; they only needed to simulate some Markov chain having the same equilibrium distribution. Simulations following the scheme of Metropolis et al. (1953) are said to use the Metropolis algorithm. As computers became more widely available, the Metropolis algorithm was widely used by chemists and physicists. A generalized form of the Metropolis algorithm, called the Metropolis–Hastings algorithm which uses the Gibbs sampler to sample each configuration of the system depending on the system parameters. For the FKM we use Metropolis–Hastings algorithm and sample its configurations by Gibbs sampler.

2.2.2 Lattice Monte Carlo for Falikov-Kimball Model

FKM is a system of correlated electrons which describes the interplay between two types of electrons: conduction c-electrons and the f-electrons which are fixed and localized particles, distributed over the lattice and form a specific configuration. We consider FKM in a square lattice. Depending on whether the site i in the lattice is occupied or not, the associated occupation number $n_{i,f}$ is 1 or 0 respectively, see Fig. 3.2 and Sec. 3.2 for more details. This feature of f-electrons provides the neccesary conditions to use MCMC. We can update the configuration of the system from one to another by only changing the $n_{i,f}$ in each site i in the lattice. therefore one can apply the Metropolis algorithm on the FKM by using Gibbs sampling for each configuration.

For applying the Metropolis algorithm to FKM, let us for example calculate the expectation value of the Hermitian operator (observable) O from the model. If we want to calculate this expectation value, i.e., $\langle O \rangle$, exactly, we must sum over $2^{L\times L}$ different configurations. Computationally, this process costs huge time and is almost impossible. With the metropolis algorithm we can just construct a Markov chain based on the model and sample each configuration and let the model to wander around reasonable numbers of configuration.

We denote the statistical weight associated to each configuration as $W(\{n_f\})$ which corresponds to the probablity of system being at specific configuration $\{n_f\}$. By knowing $W(\{n_f\})$, one can apply metropolis algorithm as follow

1. Initialize model in configuration $\{n_f\}$, this configuration has the statistical weight $W(\{n_f\})$.
2. Pick a site i randomly and propose a move by flipping its occupation number $n_{i,f}$ from 0 to 1 or vice versa and call this new configuration $\{n'_f\}$ with statistical weight $W(\{n'_f\})$.
3. Now the process of accepting or rejecting of this movement is as follow:
   - if $P = \frac{W(\{n'_f\})}{W(\{n_f\})} \geq 1$, accept the move and the system transits to a new configuration $\{n'_f\}$
   - if $P = \frac{W(\{n'_f\})}{W(\{n_f\})} < 1$ then select a random number $0 \leq \rho \leq 1$ and if $P \geq \rho$ we accept the move, otherwise not.
4. if it is required to reduce the correlation between configurations, repeat steps 2 and 3.
5. Calculate the value of the observable O for possessed configuration which can be either $\{n_f\}$ or $\{n'_f\}$.
6. Repeat 2 to 5.

One has to repeate the above steps until the system reaches the equilibrium distribution and the intended observable $\langle O \rangle$ converges to its final value.

2.2.3 Error analysis and estimators

After N Monte Carlo cycle (Metropolis algorithm) we have N measurements of observable O which can be expressed as time series of N measurements of a observable O. At this point one can introduce the concept of estimator for the expectation value $\langle O \rangle$ to estimate this quantity as physical output of Monte Carlo simulation, therefore one can calculate the arithmetic mean value of O

$$\bar{O} = \frac{1}{N} \sum_{j=1}^{N} O_j \tag{2.11}$$

We should be aware about the difference between $\langle O \rangle$ which is an ordinary number and $\bar{O}$ is a fluctuating number with variance

$$\sigma^2_{\bar{O}} = \langle [\bar{O} - \langle O \rangle]^2 \rangle = \langle \bar{O}^2 \rangle - \langle \bar{O} \rangle^2 \tag{2.12}$$

Depending on the measurements that we do, we have two type of measurements: *uncorrelated* and *correlated* measurements.

Uncorrelated measurements

When there is no correlations between the measurements or in other words, the measurements are independent, for variance we have

$$\sigma_{\bar{O}}^2 = \sigma_{O_j}^2 / N \tag{2.13}$$

where $\sigma_{O_j}^2 = \langle O_j^2 \rangle - \langle O_j \rangle^2$ is the variance for single measurement. Note that this quantity becomes important when it refers to physical quantities. For example if one consider O as mean energy then this variance for single measurement would be specific heat C_v.

Correlated measurements

One should also consider the correlation between measurements by an additional factor which comes from it

$$\begin{aligned} \sigma_{\bar{O}}^2 = \langle \bar{O}^2 \rangle - \langle \bar{O} \rangle^2 &= \frac{1}{N^2} \Big(\sum_{i,j=1}^{N} \left(\langle O_i O_j \rangle - \langle O_i \rangle \langle O_j \rangle \right) \Big) \\ &= \frac{1}{N^2} \Big(\sum_{i=1}^{N} \left(\langle O_i^2 \rangle - \langle O_i \rangle^2 \right) \Big) \\ &+ \frac{1}{N^2} \Big(\sum_{i \neq j}^{N} \left(\langle O_i O_j \rangle - \langle O_i \rangle \langle O_j \rangle \right) \Big) \end{aligned} \tag{2.14}$$

Now $\sigma_{\bar{O}}^2$ can be reformulated as follow

$$\sigma_{\bar{O}}^2 = \frac{\sigma_{\bar{O}_i}^2}{N} (1 + 2\tau_O) \tag{2.15}$$

that is written as naive variance multiply by factor $(1 + 2\tau_O)/N$ which includes auto-correlation time which has definition as

$$\tau_O = \frac{\sum_{k=1}^{N} \left(\langle O_i O_{i+k} \rangle - \langle O_i \rangle \langle O_i \rangle \right)}{\langle O_i^2 \rangle - \langle O_i \rangle \langle O_i \rangle} \tag{2.16}$$

and its asymptotic behavior when $k \to \infty$ will be

$$\tau_O \to a e^{-k/\tau} \tag{2.17}$$

where τ is exponential auto-correlation time and in general $\tau_O \neq \tau$.

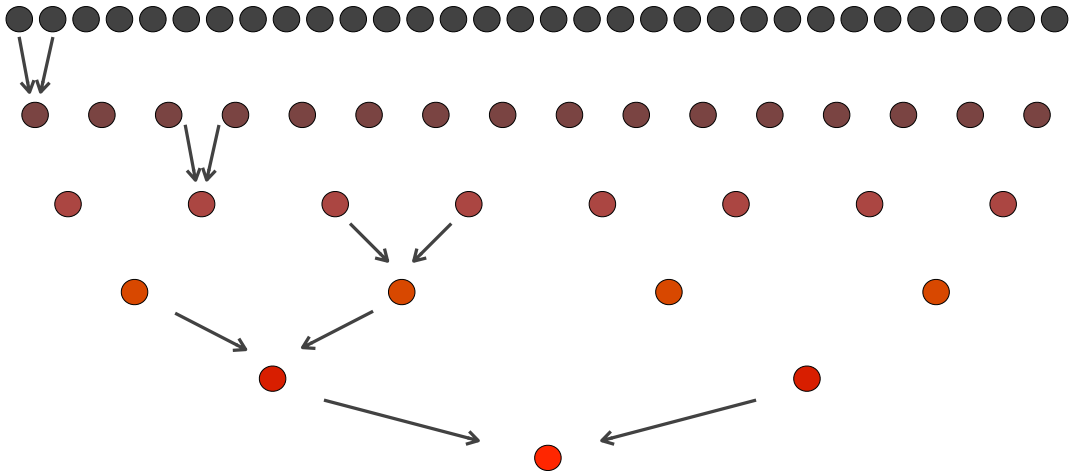

FIGURE 2.1: Binning analysis. Each row represents the datas at each binning length l

Remark the error for quantity O will be $\Delta O = \sqrt{\sigma^2_{\bar{O}}}$

Binning analysis

In the binning analysis[1] one divides the N data to $\frac{N}{2}$ blocks such that each block includes 2 datas point then average on each block , number of $\frac{N}{2}$ data will be produced. By repeating this process, one can estimate the correct error. See Fig. 2.1.

$$O_i^{(l)} = \frac{1}{2}(O_{2l-1}^{(l-1)} + O_{2l}^{(l-1)}) \tag{2.18}$$

where l is the binning length. For each binning length l we have

$$\Delta^{(l)} = \sqrt{\frac{\sigma_O^{2(l)}}{N^{(l)}}} \tag{2.19}$$

and

$$\Delta^{(l)} \xrightarrow{l \longrightarrow \infty} \Delta = \sqrt{(1 + 2\tau_O)\frac{\sigma_O^2}{N}} \tag{2.20}$$

[1]Note that there are other error analysises that we don't describe here, for example Jacknife analysis

with exponential auto-correlation time

$$\tau_O = \lim_{l \longrightarrow \infty} \frac{1}{2} \left(\frac{2^l \sigma_O^{2(l)}}{\sigma_O^{2(0)}} - 1 \right) \tag{2.21}$$

2.3 Tensor Networks Methods

What makes quantum mechanics fundamentally different from classical physics is the different nature of the states: whereas they are points in phase space in classical physics, they are rays in Hilbert space in quantum mechanics. Tensor network methods have become very popular during last years to simulate strongly correlated systems. One of the famous example of these methods is Density Matrix Renormalization Groups (DMRG). In this part of the thesis, we give a short introduction to those methods that we have used in the thesis. Here we explain Matrix Product States representation, Time-Evolving Block Decimation and finite temperature Matrix Product States representation.

2.3.1 Matrix Product States

Consider an arbitrary quantum system composed of L local Hilbert space $\{\sigma_i\}$ each of dimension d. This for example can be interacting spin-$\frac{1}{2}$ where the local states are $|\uparrow\rangle$, $|\downarrow\rangle$ and $d = 2$. For one-dimensional chain with sites 1 through to L, its pure states are then defined on the L^d-dimensional Hilbert space

$$\mathcal{H} = \otimes_{i=1}^{L} \mathcal{H}_i, \tag{2.22}$$

where $\mathcal{H}_i$ is the local Hamiltonian on site i. Now the most general state of such Hamiltonian reads

$$|\psi\rangle = \sum_{\sigma_1,\ldots,\sigma_i,\ldots,\sigma_L} c_{\sigma_1,\ldots,\sigma_i,\ldots,\sigma_L} |\sigma_1 \ldots \sigma_i \ldots \sigma_L\rangle \tag{2.23}$$

To be efficinet we use often abbreviation $\{\sigma\} = \sigma_1, \ldots \sigma_i, \ldots \sigma_L$. The usual problem of numerical simulations is that the number of state coefficients $c_{\{\sigma\}}$ grows exponentially with system size L.

Matrix Product states (MPS) is a clever way to represent a quantum state $|\psi\rangle$ systematically. Using singular value decomposition to decompose the coefficient $c_{\sigma_1,\ldots,\sigma_i,\ldots,\sigma_L}$, one can re-express them as [202]

$$c_{\sigma_1,\ldots,\sigma_i,\ldots,\sigma_L} = \sum_{\substack{\sigma_1,\ldots,\sigma_i,\ldots,\sigma_L \\ \alpha_1 \ldots \alpha_i \ldots \alpha_L}} \lambda^{[0]}_{\alpha_0} \Gamma^{\sigma_1}_{\alpha_0 \alpha_1} \lambda^{[1]}_{\alpha_1} \ldots \Gamma^{\sigma_i}_{\alpha_{i-1} \alpha_i} \lambda^{[i]}_{\alpha_i} \ldots \Gamma^{\sigma_L}_{\alpha_{L-1} \alpha_L} \lambda^{[L]}_{\alpha_L}, \tag{2.24}$$

and the state $|\psi\rangle$ becomes

$$|\psi\rangle = \sum_{\substack{\sigma_1,\ldots,\sigma_i,\ldots,\sigma_L \\ \alpha_1\ldots\alpha_i\ldots\alpha_L}} \lambda^{[0]}_{\alpha_0} \Gamma^{\sigma_1}_{\alpha_0\alpha_1} \lambda^{[1]}_{\alpha_1} \ldots \Gamma^{\sigma_i}_{\alpha_{i-1}\alpha_i} \lambda^{[i]}_{\alpha_i} \ldots \Gamma^{\sigma_L}_{\alpha_{L-1}\alpha_L} \lambda^{[L]}_{\alpha_L} |\sigma_1 \ldots \sigma_i \ldots \sigma_L\rangle, \tag{2.25}$$

where the σ_i's are physical and α's are auxiliary indices. Each $\Gamma^{\sigma_i}_{\alpha_{i-1},\alpha_i}$ is a rank-3 tensor, which therefore depends on the local state $|\sigma_i\rangle$. Note that indices α_{i-1} and α_i refer to the bond dimension on site i and sums over them run from 1 to its maximum value at each bond, χ_{max} with $\alpha_0 = \alpha_L = 1$. χ_{max} either can be chosen to be fixed during the calculations or one can let to changed dynamically based how many states are considered to be kept. Each $\lambda^{[i]}_{\alpha_i}$ is a vector of size α_i that contains the singular values at bond i. They contain information related to entanglement spectrum. In Eq. 2.24, the coefficient $c_{\{\sigma\}}$ is written as sum over product of local tensors Γ^{σ_i} and local vectors $\lambda^{[i]}$. For an infinite chain all $\Gamma^{\sigma_i}_{\alpha_{i-1},\alpha_i}$'s and $\lambda^{[i]}_{\alpha_i}$'s are the same through the chain. Note that any quantum state can be represented as an MPS, although the representation may be numerically inefficient. Nevertheless, it is therefore a mathematical structure of general interest.

In our MPS representation of this thesis, as is shown in Fig. 2.2 we use the following representation

$$|\psi\rangle = \sum_{\substack{\sigma_1\ldots\sigma_L \\ \alpha_1\ldots\alpha_{L-1}}} T^{\sigma_1}_{\alpha_1} \ldots T^{\sigma_i}_{\alpha_{i-1},\alpha_i} \ldots T^{\sigma_L}_{\alpha_{L-1}} \, |\sigma_1 \ldots \sigma_i \ldots \sigma_L\rangle, \tag{2.26}$$

with each $T^{\sigma_i}_{\alpha_{i-1},\alpha_i} = \Gamma^{\sigma_i}_{\alpha_{i-1}\alpha_i} \lambda^{[i]}_{\alpha_i}$ and they obey the right-canonical condition

$$\sum_{\sigma_i} T^{\sigma_i} T^{\sigma_i \dagger} = \mathbf{I}, \tag{2.27}$$

and $T^{\sigma_i}_{\alpha_{i-1},\alpha_i}$ are called right-normalized tensors.

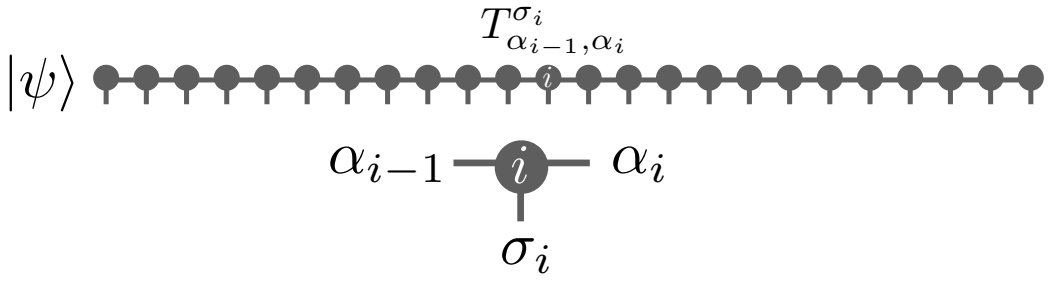

FIGURE 2.2: MPS form for a pure state $|\psi\rangle$.

2.3.2 Time-Evolving Block Decimation

Traditionally, the exposition of DMRG starts with explaining the ground state algorithm, DMRG proper, which for a given Hamiltonian $\mathcal{H}$ looks for its ground state within MPS representation. This reflects the historical course of events: time-dependent DMRG [4–6, 8] (with the variants of TEBD and tMPS, but this is all very much the same) was invented later on after ground state DMRG. In this thesis we use Time-Evolving Block Decimation (TEBD) algorithm to access both ground state and real time evolved state of the given Hamiltonin $\mathcal{H}$ using imaginary and real time evolution repectively.

The TEBD is an algorithm that generates efficiently an approximation to the time evolution of a one-dimensional system subject, in this thesis, to a nearest-neighbor Hamiltonian. TEBD is essentially a combination of an MPS description for a one-dimensional quantum system and an algorithm that applies two-site gates that are necessary to implement a Suzuki-Trotter time evolution. We restrict our attention to time-independent Hamiltonians $\mathcal{H}$; this captures a large number of the problems encountered in practice. As all more important time-evolution schemes currently in use consider small ("infinitesimal") time steps, time-dependent Hamiltonians can be modeled by a sequence of Hamiltonians that change after each small time step.

Real-Time Evolution

Assume we have an initial state $|\psi(0)\rangle$ in MPS form; such a state can be constructed by hand (in simple cases like a Néel state, which is just a $D = 1$ MPS) or is obtained by some other MPS calculation, e.g., as the ground state of some (other) Hamiltonian (otherwise there would be no non-trivial dynamics) – this is the typical setup in ultra cold atom experiments where nonequilibrium dynamics is generated by Hamiltonian quenches, i.e., abrupt changes in Hamiltonian parameters. In the case of coherent evolution, the state at time t is given by

$$|\psi(t)\rangle = U(t)\,|\psi(0)\rangle = e^{-i\mathcal{H}t}\,|\psi(0)\rangle \tag{2.28}$$

Imaginary-Time Evolution

To calculate the ground state of a given Hamiltonian using TEBD, one can use imginary time evolution. Quite generally, starting from a random state $|\psi\rangle = \sum_n c_n\,|n\rangle$, with eigenstates $\mathcal{H}\,|n\rangle = E_n\,|n\rangle$, with $E_0 \leq E_1 \leq E_2 \leq \ldots$, then we have

$$\begin{aligned} |\psi_{GS}\rangle &= \lim_{\tau\to\infty} U(\tau)\,|\psi\rangle = \lim_{\tau\to\infty} e^{-\tau\mathcal{H}}\,|\psi\rangle = \lim_{\tau\to\infty}\sum_n e^{-\tau E_n} c_n\,|n\rangle \\ &= \lim_{\tau\to\infty} e^{-\tau E_0}(c_0\,|0\rangle + \sum_{n>0} e^{-\tau(E_n-E_0)} c_n\,|n\rangle) = \lim_{\tau\to\infty} e^{-\tau E_0} c_0\,|0\rangle, \end{aligned} \tag{2.29}$$

where τ represents an imaginary time.

Suzuki-Trotter Decomposition

The Hamiltonian that we are working with, have the nearest-neighbor structure. This leads to the fact the total Hamiltonian can be split into two terms H_{even} and H_{odd} called bond operators, each are the sum over all even and odd (respectively) terms of the Hamiltonian. They commute if they do not share a site.

$$\mathcal{H} = H_{odd} + H_{even}; \qquad H_{\substack{even \\ (odd)}} = \sum_{\substack{i \\ even \\ (odd)}} \hat{h}_{i,i+1}, \tag{2.30}$$

where $h_{i,i+1}$ are the bond operator at site i. Note that all terms within H_{even} (H_{odd}) commute with each other, incurring no error while applying an operator of the form $\exp(\alpha H_{even})$ ($\exp(\alpha H_{odd})$) and ($\alpha \in \mathbb{C}$). The corresponding time evolution operators read as

$$e^{-i\mathcal{H}t} \simeq e^{-iH_{even}t}e^{-iH_{odd}t}; \qquad \exp(-iH_{\substack{even \\ (odd)}} t) = \prod_{\substack{i \\ even \\ (odd)}} e^{-ih_{i,i+1}t} = \prod_{\substack{i \\ even \\ (odd)}} U_i(t), \tag{2.31}$$

The TEBD algorithm relies on the Suzuki-Trotter decomposition[68] of the time-evolution operator $U(t)$, for this one first needs to decompose the $U(t)$ into N small time steps dt, i.e., $U(t) = [U(dt = t/N)]^N$ where N is a large enough that the time interval $dt = t/N$ is small compared to any internal time scale of the system.

The first and second order Suzuki-Trotter decomposition are as following

$$U(dt) = \prod_{\substack{i \\ odd}} U_i(dt) \prod_{\substack{i \\ even}} U_i(dt) + O(dt^2), \tag{2.32}$$

$$U(dt) = \prod_{\substack{i \\ odd}} U_i(\frac{dt}{2}) \prod_{\substack{i \\ even}} U_i(dt) \prod_{\substack{i \\ odd}} U_i(\frac{dt}{2}) + O(dt^3), \tag{2.33}$$

Two-site gate

After using Suzuki-Trotter decomposition, to evolve the state from t to $t + \delta t$, one needs to apply each gate $U_i(\delta t)$ succeively on all sites. For that one needs to use the tensor representation of $U_i(\delta t)$ at each time step. In other words, due to the nature of local Hamiltonian between site i and $i + 1$, one can write $U_i(\delta t)$ in the form of the rank-4 tensor $\Theta^{\sigma_i,\sigma_{i+1}}_{\sigma'_i,\sigma'_{i+1}}$

$$\Theta^{\sigma_i,\sigma_{i+1}}_{\sigma'_i,\sigma'_{i+1}} = \langle \sigma_i, \sigma_{i+1}|U_i(\delta t)|\sigma'_i, \sigma'_{i+1}\rangle \tag{2.34}$$

After this, one can apply this operator locally on sites i and $i + 1$ in the MPS form and proceed further. The pictural representation of the second-order Suzuki-Trotter

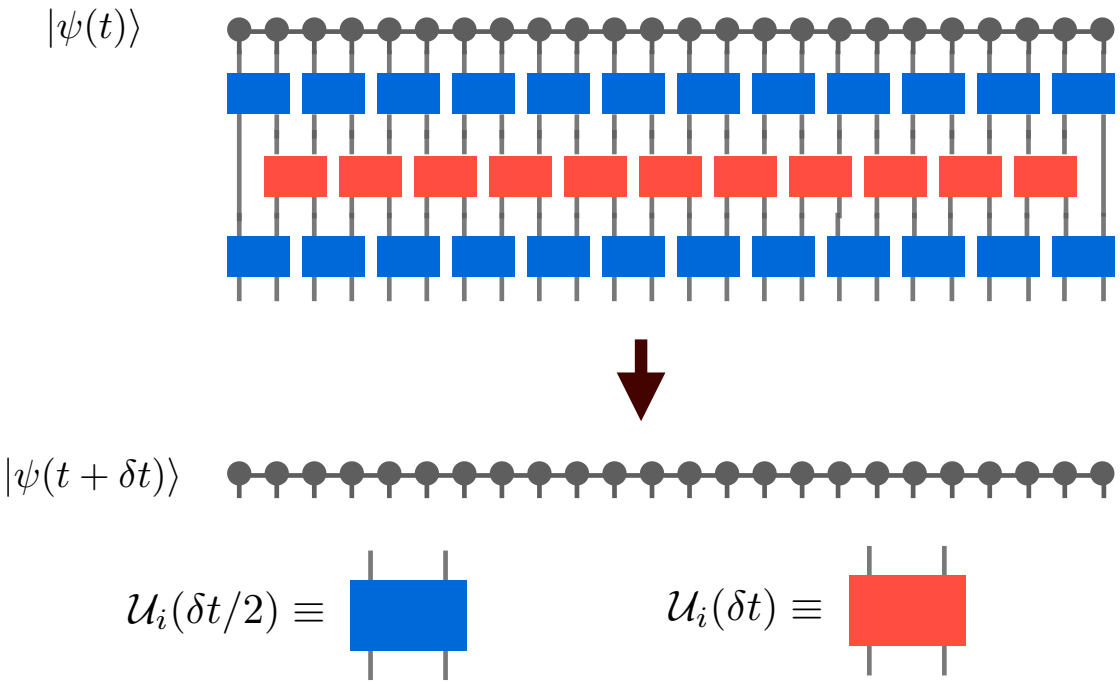

FIGURE 2.3: TEBD algorithm. Second order Suzuki-Trotter has been used. It includes three applications of the gates. First and third evolving is for odd sites with time step $\delta t/2$ and in the middle time evolution of even sites with time step δt

decomposition to evolve the state of the system from $|\psi(t)\rangle$ to $|\psi(t+\delta t)\rangle$ is shown in Fig. 2.3.

Sources of error in Time-Evolving Block Decimation

During a TEBD simulation, the two main error sources are the Trotter and the truncation error.

A decomposition to order p introduces an error of order $\epsilon_{\delta t} = (\delta t)^{p+1}$. The error incurred in one time step in general scales linearly with the system size L. This is due to the commutator relations occurring in the error term of the Suzuki-Trotter decomposition as can be seen when applying the Baker-Campbell-Hausdorff formula. Since the number of time steps taken is the total time t divided by the number of time steps $t/\delta t$, the total Trotter error is of order $O((\delta t)^p L t)$[69, 70].

The second considered error source is the truncation error. It originates from the

truncation of the Schmidt values during the application of a two-site gate. Employing the Schmidt decomposition, a bipartite state can be written

$$\begin{aligned} |\psi\rangle &= \sum_{i=1}^{\chi_{max}} \lambda_i \left|\psi_i^L\right\rangle \left|\psi_i^R\right\rangle + \sum_{i=\chi_{max}+1}^{\chi} \lambda_i \left|\psi_i^L\right\rangle \left|\psi_i^R\right\rangle \\ &= |\psi_{trunc}\rangle + |\psi_{discard}\rangle\,, \end{aligned} \tag{2.35}$$

where the left sum until χ_{max} denotes the kept part $|\psi_{trunc}\rangle$ and the right sum starting from $\chi_{max}+1$ denotes the discarded part $|\psi_{discard}\rangle$. Due to the fact that $\left|\psi^L\right\rangle$ and $\left|\psi^R\right\rangle$ are mutually orthogonal then one can infer that the discarded part is orthogonal to the truncated part.

$$\langle\psi_{trunc}|\psi_{trunc}\rangle = 1 - \sum_{i=\chi_{max}+1}^{\chi} \lambda_i^2 = 1 - w, \tag{2.36}$$

where w is the discarded weight

$$w = \sum_{i=\chi_{max}+1}^{\chi} \lambda_i^2. \tag{2.37}$$

Thus during the renormalizing $|\psi_{trunc}\rangle$ we pick up a factor of $1/(1-w)$. After n_t truncations we are off by a factor of order $(1-w)^{n_t}$. For a chain of size L after total time t with time step δt number of truncation will be $n_t \sim \dfrac{(L-1)t}{\delta t}$ and thus the truncation error is

$$\epsilon_{trunc} = (1-w)^{\frac{(L-1)t}{\delta t}} = \exp\left(\frac{(L-1)t}{\delta t}\ln(1-w)\right) \tag{2.38}$$

Thus we end up with a careful balancing of the two errors, depending on the size of the time step δt. For smaller δt we have a smaller truncation error. Yet this requires more truncations due to the larger number of time steps taken and thus in a larger truncation error.

2.3.3 Finite Temperature Matrix Product States

So far we explained the MPS formalism for pure states. If one considers the scenario for thermal (mixed) states we can not use the same formalism for them. The aim of this part is to describe the situation for the thermal states. Strongly correlated quantum many-body systems at finite temperatures can be simulated by matrix product purifications. This means one needs to purify the thermal density matrix of a many body system using auxiliary degrees of freedom. This can be done by partial trace over a pure state $|\Psi_T\rangle$ living in an enlarged Hilbert space where auxiliary degrees

of freedom $\{\bar{\sigma}_1 \dots \bar{\sigma}_i \dots \bar{\sigma}_L\} \in Q$ of spin-$\frac{1}{2}$ for each lattice site in the MPS representation[71] encodes the thermal bath

$$\rho_\beta = \frac{e^{-\beta H}}{Z} = \mathrm{Tr}_Q |\Psi_\beta\rangle\langle\Psi_\beta|. \tag{2.39}$$

For infinite temperature $T = \infty$ for each site i one can choose

$$|\psi^i_{\beta=0}\rangle = \frac{1}{\sqrt{2}} \left(|\sigma_i = \uparrow, \bar{\sigma}_i = \downarrow\rangle - |\sigma_i = \downarrow, \bar{\sigma}_i = \uparrow\rangle \right), \tag{2.40}$$

which yields the full density matrix

$$\rho_{\beta=0} = \frac{1}{Z_{\beta=0}} = \frac{1}{2^{-L}} = \mathrm{Tr}_Q |\Psi_\infty\rangle\langle\Psi_\infty| = \mathrm{Tr}_Q \prod_{i=1}^{L} |\psi^i_{\beta=0}\rangle\langle\psi^i_{\beta=0}|, \tag{2.41}$$

the thermal state $|\psi_\beta\rangle$ can be obtained from $|\psi_{\beta=0}\rangle$ with imaginary time evolution,

$$|\psi_\beta\rangle = e^{-\beta H/2} |\psi_{\beta=0}\rangle. \tag{2.42}$$

In this way one can compute the thermal density matrix by tracing out the auxiliary degrees of freedom as $\rho_\beta = \mathrm{Tr}_Q |\psi_\beta\rangle\langle\psi_\beta|$. The MPS representation of thermal states can be constructed as for pure states but with an extra index $\bar{\sigma}_i$ for auxiliary Hilbert space for each site.

$$\begin{aligned} |\psi_\beta\rangle = \sum_{\substack{\sigma_1 \dots \sigma_L \\ \bar{\sigma}_1 \dots \bar{\sigma}_L \\ \alpha_1 \dots \alpha_{L-1}}} & T^{\sigma_1 \bar{\sigma}_1}_{\alpha_1} \dots T^{\sigma_i \bar{\sigma}_i}_{\alpha_{i-1}, \alpha_i} \dots \\ & \dots T^{\sigma_L \bar{\sigma}_L}_{\alpha_{L-1}} |\sigma_1 \bar{\sigma}_1 \dots \sigma_i \bar{\sigma}_i \dots \sigma_L \bar{\sigma}_L\rangle, \end{aligned} \tag{2.43}$$

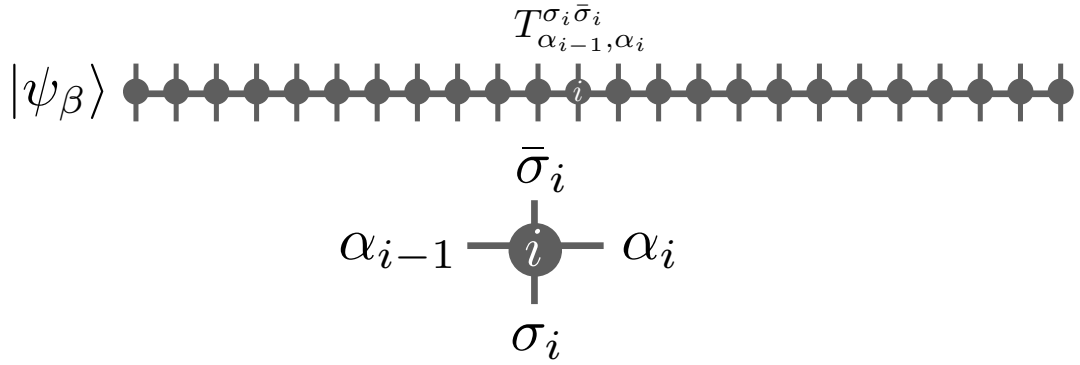

FIGURE 2.4: MPS form for thermal state $|\psi\rangle$ with auxiliary degrees of freedom $\bar{\sigma}_i$.

To cool down the system from $\beta = 0$ to the desired temperature β using imaginary time evolution, one needs to evolve the physical indices σ_i related to the each site in the chain. In the real time evolution, then the auxiliary degrees of freedom helps to minimize the growth of the entanglement by evolving them backward in time[71].

$$\left|\psi_\beta(t)\right\rangle = U_Q(t)U(t)\left|\psi_\beta(0)\right\rangle \tag{2.44}$$

with $U_Q(t) = \exp(+i\tilde{H}t)$ the time evolution operator backwrd in time for auxiliary indecies Q with $\tilde{H} = H(\sigma_i \to \bar{\sigma}_i)$ and $U(t) = \exp(-iHt)$ as time evolution operator. This helps to reach to longer time during time evolution and thus one can reduce the numerical cost of the calculations.

Chapter 3

Interaction tuned Anderson versus Mott Insulator

A Fermi liquid becomes unstable in the presence of strong disorder or Coulomb repulsion. Although this has been known for a long time, the interplay of disorder and electron-electron interaction near the metal-insulator transition is still at the forefront of condensed matter research [72, 73]. This is at least in part due to the lack of general techniques to tackle strong electron interactions in the presence of disorder in higher-dimensional systems.

As is well known, a metal is a good electrical and thermal conductor, as defined by a non-vanishing value of the DC conductivity. An insulator can therefore be defined as a system for which this quantity vanishes.

In systems where the electron-electron interaction can be neglected, two types of insulators, *i.e.* band insulators and Anderson insulators, can exist. In the presence of interactions, the situation is richer, as *e.g.* Mott insulators, excitonic insulators, or even Wigner crystals may form. Under the special condition of perfect nesting, an ordered band insulator-like state is also possible as a result of an electronic phase transition.

Following the seminal work of Basko et al. [73], the many-body localized state, *i.e.* the insulating state that has its origin in the interplay of disorder and interaction, has recently received increased attention [25, 74].

Typically, the term disorder is understood as being synonymous to quenched disorder, *e.g.* when random variables are assumed not to evolve with time. The average over the disorder is taken to mimic the spatial self-averaging of the system. This is in contrast to the annealed disorder where the disorder follows a thermal distribution. When (quantum) dynamics is neglected the partition function of any system can appear as that of an annealed disorder problem. In systems where a separation of time scales permits this neglect for the slow fields, occurrence of a localization without explicit disorder may be possible [75, 76, 77, 78]. Only at sufficiently high temperature, where every configuration carries essentially the same thermal weight, the difference between quenched and annealed disorder is immaterial.

3.1 Phase Diagram

In this chapter we revisit the finite temperature phase diagram of the two-dimensional FKM at half-filling using state-of-the-art Lattice Monte Carlo techniques. The main results are summarized in Fig. 3.1 that shows the phase diagram of the particle-hole symmetric FKM in the interaction U - temperature T plane. By analyzing different observables of the mobile electrons we found multiple different regions with qualitatively distinct properties:

- A charge density wave (CDW) at low temperatures

at high temperature:

- large U Mott-like insulator (MI) phase
- a non-interacting Fermi gas (FG) at $U = 0$
- a central result of the chapter, a region overlooked in previous studies [79] where weak localization (WL) induces a finite-volume crossover between a bad-metal (see below) and an Anderson-insulator (AI).

3.2 Falicov-Kimball Model

The Falicov-Kimball model (FKM) [80] is one of the simplest lattice models of interacting electrons. It was originally developed to describe the metal-insulator transition in the context of f-electron systems and can be understood as a limiting case of the Hubbard model where the dynamics of one of the spin-degenerate fermion species is neglected. Thus, these fermions become immobile. Therefore, the partition function of the FK model can be seen as one of annealed disorder of local f-electron occupation numbers, allowing for the possibility to observe the Anderson localization in the absence of explicit disorder. At half-filling, the FK model describes a charge-ordered state below some U-dependent transition temperature $T_c(U)$ at all non-vanishing values of the interaction strength U between localized and itinerant electrons [81, 82, 79, 83]. This charge-ordered state is commonly referred to as a charge-density wave (CDW) state. Within the standard approach to strongly correlated electron systems, *i.e.* the dynamical mean field theory (DMFT), the resulting effective impurity action, associated with the FK model can be solved exactly [84, 81, 85, 86, 87, 88]. For this reason, the FK model is often taken as a test bed for DMFT approaches and its extensions [55, 89, 90].

3.2.1 Hamiltonian

FKM includes two type of electrons, localized and massive $f-$electrons and itinerant conduction $c-$electrons which have local Coulmob interaction with each other,

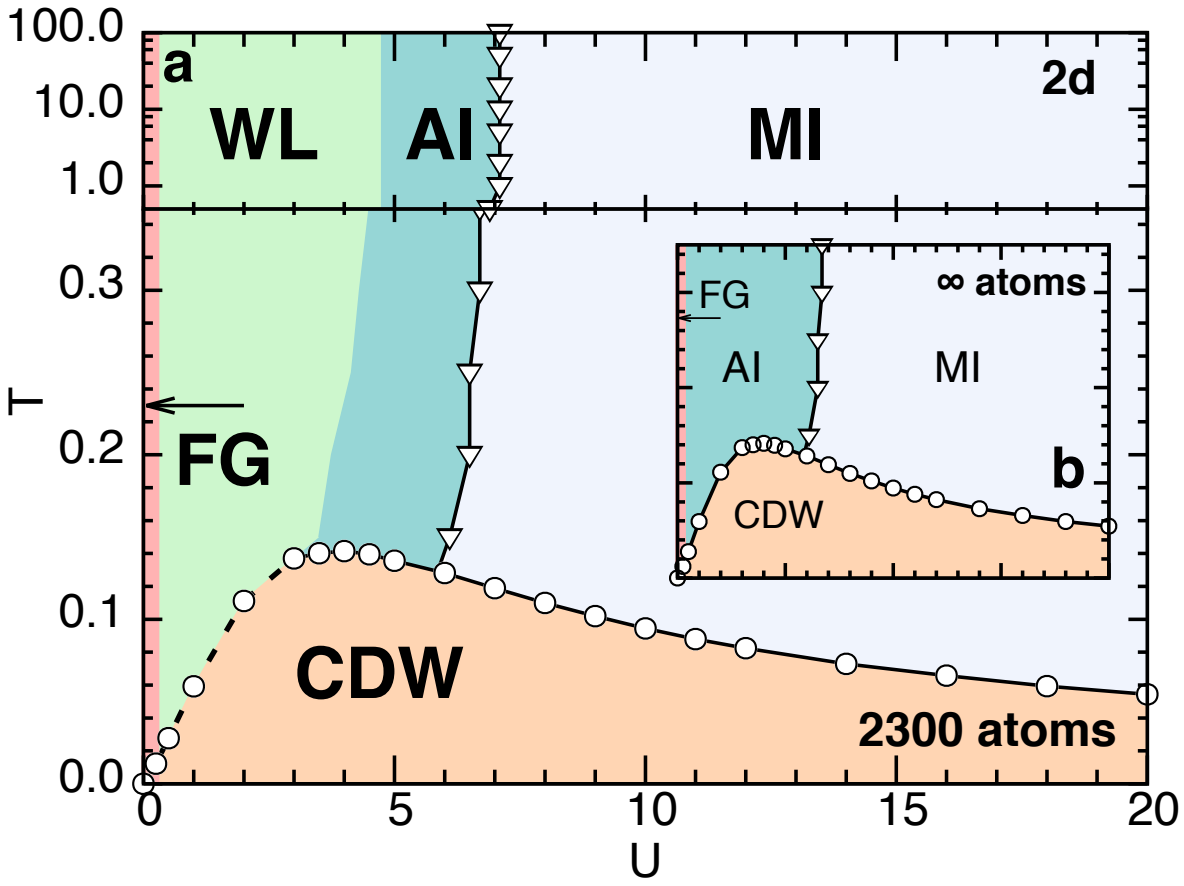

FIGURE 3.1: Phase diagram of the particle-hole symmetric FK model in 2d in U-T plane, obtained by lattice Monte-Carlo, consisting of different phases: Fermi gas (FG) at $U = 0$, charge-density wave insulator (CDW) at low temperature and all non-zero values of U. High temperature phases: Anderson insulator (AI) at intermediate values of U crossing over to a weakly localized (WL) at smaller U, Mott-like insulator (MI) at large U. The points and lines show phase boundaries, the dashed line indicates the first order phase transition between WL and CDW phases. Inset: extrapolation to the thermodynamic limit.

see Fig. 3.2. The Hamiltonian of FKM will read as:

$$\hat{\mathcal{H}} = \hat{\mathcal{H}}_K + \hat{\mathcal{H}}_\mu + \hat{\mathcal{H}}_V, \tag{3.1}$$

where $\hat{\mathcal{H}}_K$, $\hat{\mathcal{H}}_\mu$ and $\hat{\mathcal{H}}_V$ stand for kinetic energy, chemical energy and potential energy respectively, and are defined as

$$\hat{\mathcal{H}}_K = -t \sum_{\langle i,j \rangle} (c_i^\dagger c_j + h.c), \tag{3.2}$$

$$\hat{\mathcal{H}}_\mu = -\sum_i (\mu_c c_i^\dagger c_i + \mu_f f_i^\dagger f_i), \tag{3.3}$$

$$\hat{\mathcal{H}}_V = U \sum_i \hat{n}_{c,i} \hat{n}_{f,i}, \tag{3.4}$$

where

- i and j label the spatial sites of the lattice. $\langle i, j \rangle$ represents a pair of nearest-neighbor sites in the lattice and indicates that the electrons only hopping to nearest neighboring sites.
- the operators $c_i^\dagger$ and c_i are the fermion creation and annihilation operators for electrons located on the ith lattice site.
- the operators $\hat{n}_{i,c} = c_i^\dagger c_i$ and $\hat{n}_{i,f} = f_i^\dagger f_i$ are the number operators which count the number of electrons on site i.
- t is the hopping parameter for the kinetic energy of the electrons, and is determined by the overlap of at wave functions on neigh-boring sites.
- U is the repulsive Coulomb interaction between electrons on the same lattice site. The term $U\hat{n}_{c,i}\hat{n}_{f,i}$ represents an energy cost U for the site i to have two electrons and describes a local repulsion between electrons.
- μ is the chemical potential parameter which controls the electron numbers (density).

Half-Filling case: We consider the case of half-filling band, where the number of c-electrons is equal to f-electrons and their sum is equal to lattice sizes. For this we set in the following we set $\mu_c = \mu_f = \mu = U/2$ corresponding to the half-filling condition for both species.

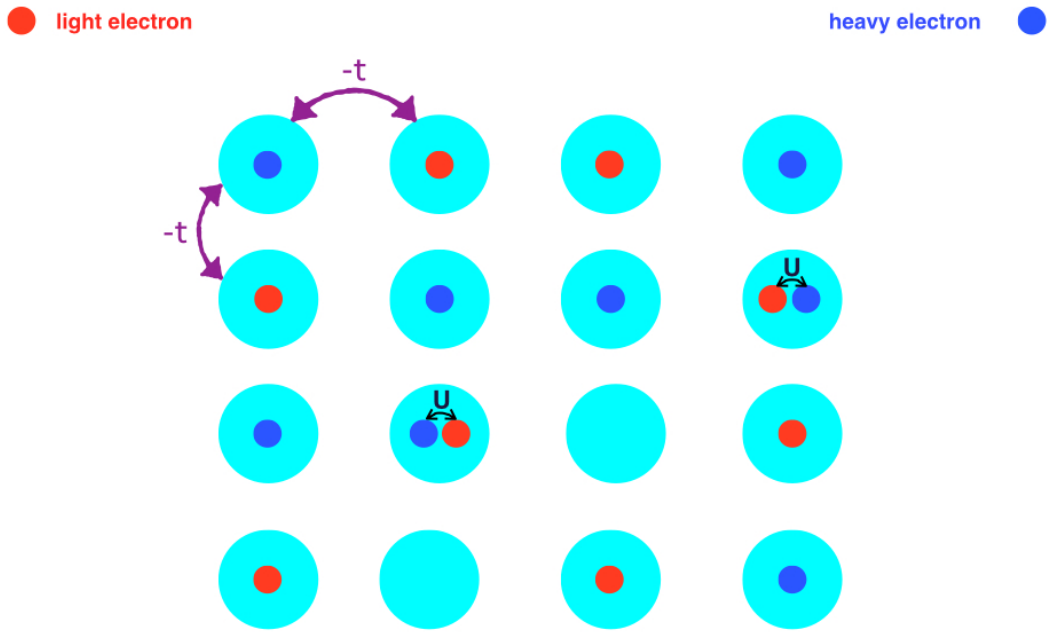

FIGURE 3.2: schematic of Falicov-Kimball Model at half-filling regime for a random configuration for a 4×4 lattice.

3.2.2 Thermodynamic quantities

Because the $f-$electrons are localized, one can write the FKM in a quadradic form and derive an effective Hamiltonian for each configuration $\left[\{n_f\}\right]$

$$\hat{\mathcal{H}} = -\mu_f \sum_i f_i^\dagger f_i + \vec{\mathcal{C}}^\dagger (T - \mu_c \boldsymbol{I} + V)\vec{\mathcal{C}}, \tag{3.5}$$

where $\vec{\mathcal{C}}$ and $\vec{\mathcal{C}}^\dagger$ are vectors that includes all annihilation and creation operators at different sites

$$\vec{\mathcal{C}} = \begin{pmatrix} \hat{c}_1 \\ \hat{c}_2 \\ \vdots \\ \hat{c}_N \end{pmatrix} \quad and \quad \vec{\mathcal{C}}^\dagger = (\hat{c}_1^\dagger, \quad \hat{c}_2^\dagger \quad , \cdots , \quad \hat{c}_N^\dagger)$$

and $\boldsymbol{I}$ is the identity matrix, $T = -t \sum_{\langle i,j \rangle} |i\rangle\langle j|$ and $V = \sum_i |i\rangle n_{f,i} \langle i|$.

Partition function

The partition function of the FKM reads

$$
\begin{aligned}
Z = \mathrm{Tr}\left[e^{-\beta\mathcal{H}}\right] &= \sum_{\{n_f\}} e^{\beta\mu_f \sum_i n_{f,i}} \mathrm{Tr}_c \left[e^{-\beta\vec{\mathcal{C}}^\dagger \boldsymbol{H}[\{n_f\}]\vec{\mathcal{C}}}\right] \\
&= \sum_{\{n_f\}} e^{\beta\mu_f \sum_i n_{f,i}} \det\left[1 + e^{-\beta \boldsymbol{H}[\{n_f\}]}\right] = \sum_{\{n_f\}} P\left[\{n_f\}\right],
\end{aligned}
\tag{3.6}
$$

which is written sum over all possible charge configurations. $P[\{n_f\}]$ is partition function (statistical weight) of the specific charge configuration $\{n_f\}$ with

$$
\boldsymbol{H}[\{n_f\}] = T - \mu_c I + V[\{n_f\}], \tag{3.7}
$$

Average energy

The average energy per site over all configurations is given by

$$
\mathcal{U} = \frac{1}{V}\langle \boldsymbol{H} \rangle = \frac{1}{V}\frac{1}{Z}\sum_{\{n_f\}} E\left[\{n_f\}\right] P\left[\{n_f\}\right], \tag{3.8}
$$

with the energy for a specific configuration $\left[\{n_f\}\right]$

$$
\begin{aligned}
E\left[\{n_f\}\right] &= -\mu_f \sum_i n_{f,i} + \mathrm{Tr}\left[\boldsymbol{H}\left[\{n_f\}\right]\left[1 + e^{\beta \boldsymbol{H}[\{n_f\}]}\right]^{-1}\right] \\
&= -\partial_\beta P\left[\{n_f\}\right],
\end{aligned}
\tag{3.9}
$$

Specific Heat

The specific heat is given by

$$
\begin{aligned}
\mathcal{C}_V &= \beta^2 \frac{1}{V}\left\{\frac{1}{Z}\sum_{\{n_f\}} P\left[\{n_f\}\right]\left[E\left[\{n_f\}\right]^2 - \delta^2 E\left[\{n_f\}\right]\right] - \left(\frac{1}{Z}\sum_{\{n_f\}} E\left[\{n_f\}\right] P\left[\{n_f\}\right]\right)^2\right\} \\
&= \beta^2 \frac{1}{V}\left[\left\langle E^2 - \delta^2 E\right\rangle - \langle E\rangle^2\right],
\end{aligned}
\tag{3.10}
$$

with

$$
\delta^2 E\left[\{n_f\}\right] = \partial_\beta E\left[\{n_f\}\right] = \frac{1}{2}\mathrm{Tr}\left[\boldsymbol{H}\left[\{n_f\}\right]^2\left[1 + \cosh\left(\beta \boldsymbol{H}\left[\{n_f\}\right]\right)\right]^{-1}\right].
$$

3.2.3 Correlation function- f's

For the f's only the static charge susceptibility is non-zero and is given by

$$\chi_f(q) = \left\langle \hat{n}_{\vec{q}} \hat{n}_{-\vec{q}} \right\rangle = \frac{1}{V} \sum_{\vec{r}\vec{r}'} e^{i(\vec{r}-\vec{r}').\vec{q}} \left\langle \hat{n}_{\vec{r}} \hat{n}_{\vec{r}'} \right\rangle, \tag{3.11}$$

where $\vec{q}$ and $\vec{r}$ label the lattice points in momentum and real space respectively. The charge order parameter,assuming symmetry breaking with ordering vector $\vec{Q}$, is

$$\phi_{\vec{Q}_f} = \left\langle \hat{n}_{\vec{q}} \right\rangle = \frac{1}{V} \sum_{\vec{r}} e^{i\vec{r}.\vec{q}} \left\langle \hat{n}_{\vec{r}} \right\rangle. \tag{3.12}$$

The Binder cummulant for this quantity is

$$B_{\vec{Q}} = 1 - \frac{\left\langle \left(\hat{n}_{\vec{Q}} \hat{n}_{-\vec{Q}} \right)^2 \right\rangle}{3 \left\langle \left(\hat{n}_{\vec{Q}} \hat{n}_{-\vec{Q}} \right) \right\rangle^2}. \tag{3.13}$$

For the square lattice, the ordering vector for a charge density wave[1] is $\vec{Q} = [\pi, \pi]$ (and thus $\vec{Q} = -\vec{Q}$) so all these quantities can be obtained from the MC history of the observable $\hat{n}_{\vec{Q}} = \frac{1}{\sqrt{V}} \sum_{\vec{r}} (-1)^{r_1+r_2} \hat{n}_{\vec{r}}$ with $\vec{r} = r_1\hat{x} + r_2\hat{y}$. For a triangular lattice, since the ordering vector, if it exists, is in general not known one will have to compute $\chi_f(\vec{q})$ for every $\vec{q}$.

[1] checkerboard pattern for f-electrons means the occupation in one site is either 0 or 1.

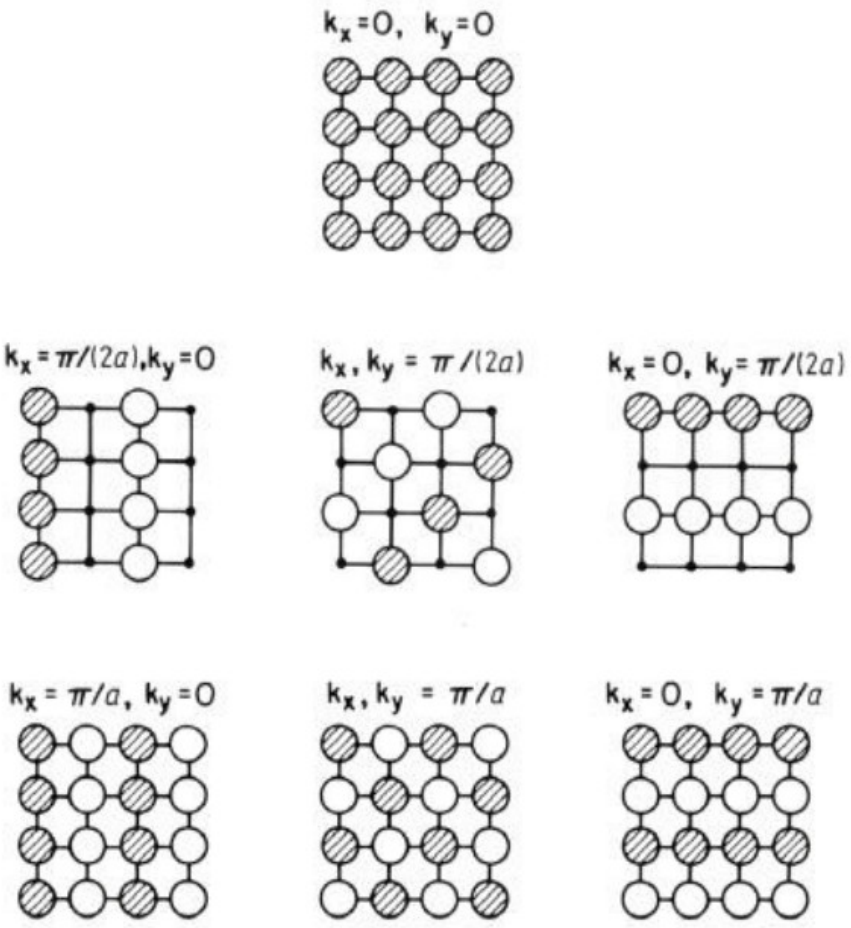

FIGURE 3.3: Different ordering vector $\vec{k} = k_x\hat{x} + k_y\hat{y}$ for a square lattice.

3.2.4 Spectral function-c's

A correlation function $\left\langle \hat{O}_1(\tau)\, \hat{O}_2(0) \right\rangle$ where the operators $\hat{O}_{1,2}$ can be written solely in terms of c-electrons's can be written as

$$\begin{aligned}\left\langle O_1(\tau) O_2(0)\right\rangle &= \frac{1}{Z}\mathrm{Tr}\left[e^{-\beta H}\hat{O}_1(\tau)\hat{O}_2(0)\right] \\ &= \frac{1}{Z}\sum_{\{n_f\}} e^{\beta\mu_f\sum_i n_{f,i}}\mathrm{Tr}_c\left[e^{-\beta\vec{\mathcal{C}}^\dagger \boldsymbol{H}[\{n_f\}]\vec{\mathcal{C}}}\hat{O}_1(\tau)\hat{O}_2(0)\right] \\ &= \frac{1}{Z}\sum_{\{n_f\}} P\left[\{n_f\}\right]\left\langle T_\tau \hat{O}_1(\tau)\hat{O}_2(0)\right\rangle_{[\{n_f\}]},\end{aligned} \tag{3.14}$$

where Tr_c is taken with respect to a quadratic Hamiltonian and Wick's theorem applies inside the average.

Thus let us first consider the case of the Green's function $\hat{O}_1 = \hat{c}_i, \hat{O}_2 = \hat{c}_j^\dagger$, using

$$\hat{c}_i(\tau) = e^{\tau\vec{\mathcal{C}}^\dagger \boldsymbol{H}[\{n_f\}]\vec{\mathcal{C}}}\hat{c}_i e^{-\tau\vec{\mathcal{C}}^\dagger \boldsymbol{H}[\{n_f\}]\vec{\mathcal{C}}} = \left[e^{-\tau\boldsymbol{H}[\{n_f\}]}.\vec{\mathcal{C}}\right]_i \tag{3.15}$$

which is obtained by integrating the equations of motion for $\hat{c}(\tau)$. Now for Green's function, we have

$$\begin{aligned}\boldsymbol{G}_{i,j}(\tau) &= -\left\langle \hat{c}_i(\tau)\hat{c}_j^\dagger(0)\right\rangle \\ &= -\frac{1}{Z}\sum_{\{n_f\}} P\left[\{n_f\}\right]\left[e^{-\tau\boldsymbol{H}[\{n_f\}]}\left(1+e^{-\beta\boldsymbol{H}[\{n_f\}]}\right)^{-1}\right]_{i,j},\end{aligned} \tag{3.16}$$

where the following identity has been used

$$\mathrm{Tr}_c\left[e^{-\beta\vec{\mathcal{C}}^\dagger \boldsymbol{H}[\{n_f\}]\vec{\mathcal{C}}}\hat{c}_k\hat{c}_j^\dagger\right] = \det\left[1+e^{-\beta\boldsymbol{H}[\{n_f\}]}\right]\left[1+e^{-\beta\boldsymbol{H}[\{n_f\}]}\right]^{-1}_{i,j}. \tag{3.17}$$

In Matsubara space one obtains:

$$\boldsymbol{G}(i\omega_n) = \int_0^\beta d\tau e^{i\omega_n\tau}\boldsymbol{G}(\tau) = \frac{1}{Z}\sum_{\{n_f\}} P\left[\{n_f\}\right]\frac{1}{i\omega_n - \boldsymbol{H}\left[\{n_f\}\right]}, \tag{3.18}$$

and, by analytic continuation, for the spectral matrix we have

$$\begin{aligned}\boldsymbol{A}(\omega) &= -\frac{1}{2\pi}\left[\boldsymbol{G}\left(\omega+i0^+\right)-\boldsymbol{G}\left(\omega+i0^+\right)^\dagger\right] \\ &= \frac{1}{Z}\sum_{\{n_f\}} P\left[\{n_f\}\right]\delta\left(\omega-\boldsymbol{H}\left[\{n_f\}\right]\right).\end{aligned} \tag{3.19}$$

The local density of states of the c electrons is then given by

$$\begin{aligned} A_{\text{loc}}(\omega) &= \frac{1}{V}\sum_{\vec{r}} \langle \vec{r}| \boldsymbol{A}(\omega) |\vec{r}\rangle = \frac{1}{V}\text{Tr}\left[\boldsymbol{A}(\omega)\right] \\ &= \frac{1}{Z}\sum_{n_f} P\left[\{n_f\}\right] \sum_{\alpha} \delta\left(\omega - \varepsilon_\alpha\left[\{n_f\}\right]\right), \end{aligned} \tag{3.20}$$

which this can be obtained for all frequencies by storing the MC history of eigenvalues $\varepsilon_\alpha\left[\{n_f\}\right]$, or for a given frequency ω by storing only the MC history of the quantity $\sum_\alpha \frac{\eta/\pi}{\left(\omega-\varepsilon_\alpha[\{n_f\}]\right)^2+\eta^2}$ with $\eta \to 0^+$ which is the width of the regularized delta function.

3.2.5 Inverse Participation Ratio

To measure the degree of the localization for c-electrons, one can use the so-called Inverse Participation Ratio (IPR). The IPR of state $|\psi\rangle$ is given by

$$\mathrm{I}_{|\psi\rangle} = \frac{\sum_{\vec{r}} |\langle \vec{r}\,|\psi\rangle|^4}{\sum_{\vec{r}} |\langle \vec{r}\,|\psi\rangle|^2} \tag{3.21}$$

where $|\vec{r}\rangle$'s are eigenvectros of the position operator $\hat{x}|\vec{r}\rangle = r_x|\vec{r}\rangle$ and $\hat{y}|\vec{r}\rangle = r_y|\vec{r}\rangle$.

The IPR at a given frequency (for a system with no disorder) is thus given by

$$I(\omega) = \frac{\sum_\alpha I_{|\alpha\rangle}\delta(\omega-\varepsilon_\alpha)}{\sum_\alpha \delta(\omega-\varepsilon_\alpha)} \tag{3.22}$$

Averaging over the position of the f-electrons one has

$$\bar{I}(\omega) = \frac{1}{Z}\sum_{\{n_f\}} P\left[\{n_f\}\right] \frac{\sum_\alpha I_{|\alpha[\{n_f\}]\rangle}\delta\left(\omega-\varepsilon_\alpha\left[\{n_f\}\right]\right)}{\sum_\alpha \delta\left(\omega-\varepsilon_\alpha\left[\{n_f\}\right]\right)} \tag{3.23}$$

Note that in order to compute this quantity one has to keep the MC history of both $\varepsilon_\alpha\left[\{n_f\}\right]$ and $I_{|\alpha[\{n_f\}]\rangle}$.

IPR-thermal average

Instead of evaluating IPR spectrum, we can also consider the thermal average of IPR, i.e.

$$I = \frac{1}{Z}\sum_{\{n_f\}} P\left[\{n_f\}\right] \sum_\psi \left[1+e^{\beta\varepsilon_\psi[\{n_f\}]}\right]^{-1} \frac{\sum_{\vec{r}} |\langle \vec{r}\,|\psi\rangle|^4}{\sum_{\vec{r}} |\langle \vec{r}\,|\psi\rangle|^2}$$

here as before we need to keep the history of both $\varepsilon_\alpha\left[\{n_f\}\right]$ and $I_{|\alpha[\{n_f\}]\rangle}$.

3.2.6 Charge Stiffness

Definition

The charge stiffness is defined as [91]

$$D = \frac{L_x}{2} \sum_m \frac{e^{-\beta E_m}}{Z} \partial_\phi^2 E_m \Big|_{\phi=0} \tag{3.24}$$

where the E_m's are the many-body eigen energies of the system and ϕ is the total flux inserted perpendicular to, say the $\hat{x}$ direction, with periodic boundary conditions and length L_x. The flux causes the hopping terms to change according to the minimal coupling prescription: $c^\dagger_{\vec{r}+\hat{x}} c_{\vec{r}} \to e^{i\frac{\phi}{L_x}} c^\dagger_{\vec{r}+\hat{x}} c_{\vec{r}}$. D is also called Drude weight and is related to the $\omega = 0$ component of the real part of optical conductivity

$$\sigma'(\omega) = 2\pi D \delta(\omega) + \sigma'_{\text{reg}}(\omega) \tag{3.25}$$

D is supposed to be finite for a material that conducts current and should vanish for an insulator. Note that the form Eq. 3.24 is the finite-temperature form of the Drude weight.

For an Hamiltonian with time-reversal symmetry, D can be computed directly from the free energy $F = -\frac{1}{\beta} \ln Z$

$$\partial_\phi^2 F\Big|_{\phi=0} = \sum_m \frac{e^{-\beta E_m}}{Z} \partial_\phi^2 E_m \Big|_{\phi=0} \tag{3.26}$$

The time reversal symmetry is needed in order to have $\partial_\phi E_m\big|_{\phi=0} \propto \langle \Psi_m | \hat{J} | \Psi_m \rangle = 0$ where $\hat{J}$ is the current operator.

For our case, where the free energy can be obtained from the single particle states, we have

$$D = \frac{L_x}{2} \partial_\phi^2 F\Big|_{\phi=0} \tag{3.27}$$

$$= -\frac{L_x}{2} \frac{1}{\beta} \sum_\alpha \partial_\phi^2 \ln\left[1 + e^{-\beta\varepsilon_\alpha}\right]\Big|_{\phi=0} \tag{3.28}$$

$$= \frac{L_x}{2} \sum_\alpha \frac{\partial_\phi^2 \varepsilon_\alpha\big|_{\phi=0}}{e^{\beta\varepsilon_\alpha} + 1} \tag{3.29}$$

where $\varepsilon_\alpha = \varepsilon_\alpha\left[\{n_f\}\right]$ are the single particle eigenstates for a given configuration of the f-electrons and using $\partial_\phi \varepsilon_\alpha\big|_{\phi=0} = 0$.

Charge Stiffness for Falicov-Kimball Model

For the FKM, we obtain,

$$D = \frac{L_x}{2}\sum_{\alpha}\frac{1}{e^{\beta\varepsilon_\alpha}+1}\left[-\langle\alpha|\,\hat{T}_{x=0}\,|\alpha\rangle + 2\sum_{\alpha'\neq\alpha}\frac{\langle\alpha|\,\hat{J}_{x=0}\,|\alpha'\rangle\,\langle\alpha'|\,\hat{J}_{x=0}\,|\alpha\rangle}{\varepsilon_\alpha-\varepsilon_{\alpha'}}\right] \tag{3.30}$$

where $|\alpha\rangle$ are the single-particle eigenstates with energies ε_α.

3.3 Towards a field theory description

In this part, we show how to map the FKM to the corresponing Ising model using field theory descrptions for large U limits. We use formulation for coherent path integral in appendix A to give this field theory descriptions.

Perturbation Theory for the Falicov-Kimball Model

For a fixed configuration of the f-electrons in the large U limit we want to treat with kinetic term as small correction to the FKM Hamiltonian and consider it as perturbation in the model. We can write equation 3.7 as[2]

$$\mathcal{H} = H_0 + H_p \tag{3.31}$$

with $H_0 = -\mu_c I + V$ and $H_p = T$.

3.3.1 Coherent path integral for Falicov-Kimball Model

We can write equation 3.5 as follow

$$H - \mu N = \sum_{i,j}\left(-\mu_c + U n_{f,i}\right)\delta_{i,j}c_i^\dagger c_j + \sum_{\langle i,j\rangle} c_i^\dagger T c_j \tag{3.32}$$

[2]there is also a constant term related to chemical potential of the f-electrons for each specific configuration such that we can add to the Hamiltonian for each fixed configuration.

now for the partition function we have

$$Z = Z_0 \langle e^{-\int_0^\beta d\tau \left[\sum_{i,j} \bar{\psi}_i(\tau) T \psi_j(\tau)\right]} \rangle_0 \tag{3.33}$$

$$\ln Z = \ln Z_0 + \ln \langle e^{-\int_0^\beta d\tau \left[\sum_{i,j} \bar{\psi}_i(\tau) T \psi_j(\tau)\right]} \rangle_0 \tag{3.34}$$

$$\ln Z = \ln Z_0 + \ln \left(\frac{e^{\mathrm{Tr}\ln(G_0^{-1}+T)}}{e^{\mathrm{Tr}\ln G_0^{-1}}} \right) \tag{3.35}$$

$$\ln Z = \ln Z_0 + \mathrm{Tr}\ln(1 + G_0 T) \tag{3.36}$$

$$\ln Z = \ln Z_0 - \mathrm{Tr} \sum_{k=1} \frac{(-1)^k}{k} (G_0 T)^k \tag{3.37}$$

Here Z and Z_0 have the same with $P[\{n_f\}]$ that we calculated from 3.6. and

$$\ln Z_0 = \beta \mu_f \sum_r n_{f,r} + \sum_r \ln[1 + e^{-\beta(-\mu_c 1 + U n_{f,r})}] \tag{3.38}$$

In The FKM $(G_0)^{-1}$ (bare green's function) would be

$$G_0^{-1}(i\omega_n) = (i\omega_n + \mu_c I - UV[\{n_f\}]) \tag{3.39}$$

First order term

There is no contribution for the first order term $k = 1$

$$\mathrm{Tr}(G_0 T) = \sum_{i\omega_n} \sum_{r,r'} (G_0)_{r,r'} T_{r,r'} = \sum_{i\omega_n} \sum_r G_0(r) T_{rr} = 0 \tag{3.40}$$

because T has no diagonal element.

Second Order term

For second order term we have

$$\begin{aligned} -\frac{1}{2}\mathrm{Tr}(G_0 T)^2 &= -\frac{1}{2} \sum_{i\omega_n} \sum_{r,r'} G_0(r)(T)_{r,r'} G_0(r')(T)_{r',r} \\ &\overset{r'=r+\delta}{=} -\frac{1}{2} \sum_{i\omega_n} \sum_{r,\delta} G_0(r)(T)_{r,(r+\delta)} G_0(r+\delta)(T)_{(r+\delta),r} \end{aligned} \tag{3.41}$$

Remark: For sum over Matsubara frequency

$$S_0^F(z) = \frac{1}{\beta} \sum_{i\omega_n} g_0(i\omega_n) \tag{3.42}$$

with $g_0(z) = \prod_j \frac{1}{z-z_j}$ we can use

$$S_0^F(z) = \sum_j \underset{z=z_j}{Res}[g_0(z)]f(z_j) \tag{3.43}$$

with Fermi-Dirac distribution function $f(z) = \frac{1}{1+e^{\beta z}}$.

When we do the integration there are 4 possibilities for occupation of the set of $\{n_{r,f}, n_{r+\delta,f}\}$ as follows

$$\{n_{r,f} = 0, n_{r+\delta,f} = 0\}$$
$$\{n_{r,f} = 1, n_{r+\delta,f} = 0\}$$
$$\{n_{r,f} = 1, n_{r+\delta,f} = 1\}$$
$$\{n_{r,f} = 0, n_{r+\delta,f} = 1\}$$

Then we should write the result of the integration as combination of $x_0 + x_1(n_{r,f} + n_{r+\delta,f}) + x_2(n_{r,f}n_{r+\delta,f})$ and by considering sum over each set of the $\{n_{r,f}, n_{r+\delta,f}\}$ we can calculate coefficients x_0, x_1 and x_2.

The final form of the second order term would be

$$K_2 = -\frac{1}{2}\mathrm{Tr}(G_0T)^2 = -\frac{\beta}{2}\left[\frac{2}{U}\tanh(\frac{\beta U}{4}) - \frac{\beta}{2}\frac{1}{\cosh^2(\frac{\beta U}{4})}\right]\sum_{r,\delta}(n_{r,f} + n_{r+\delta,f})^2 + \cdots \tag{3.44}$$

In the large U limit, this equation becomes

$$K_2 = -\frac{1}{2}\mathrm{Tr}(G_0T)^2 \approx \frac{\beta}{U}\sum_{r,\delta}(n_{r,f} + n_{r+\delta,f})^2 \tag{3.45}$$

by using $s_r = 2(n_r - \frac{1}{2})$ we can map the FKM to the corresponding Ising model.

$$K_2 = -\frac{1}{2}\mathrm{Tr}(G_0T)^2 \approx -\frac{\beta}{2U}\sum_{r,\delta} s_r s_{r+\delta} \tag{3.46}$$

In the above expression, in fact $\frac{\beta}{2U} = \beta J_{eff}$ and $J_{eff} = \frac{1}{2U}$.

From Onsager solution for $2D$ Ising model we know $kT_c = 2.265189J$ and we can compute transition temperature at large U for the FKM.

$$kT_c = \frac{2.265189}{2U} \tag{3.47}$$

In the figure 3.4 there are different comparisons for different J_{eff}.

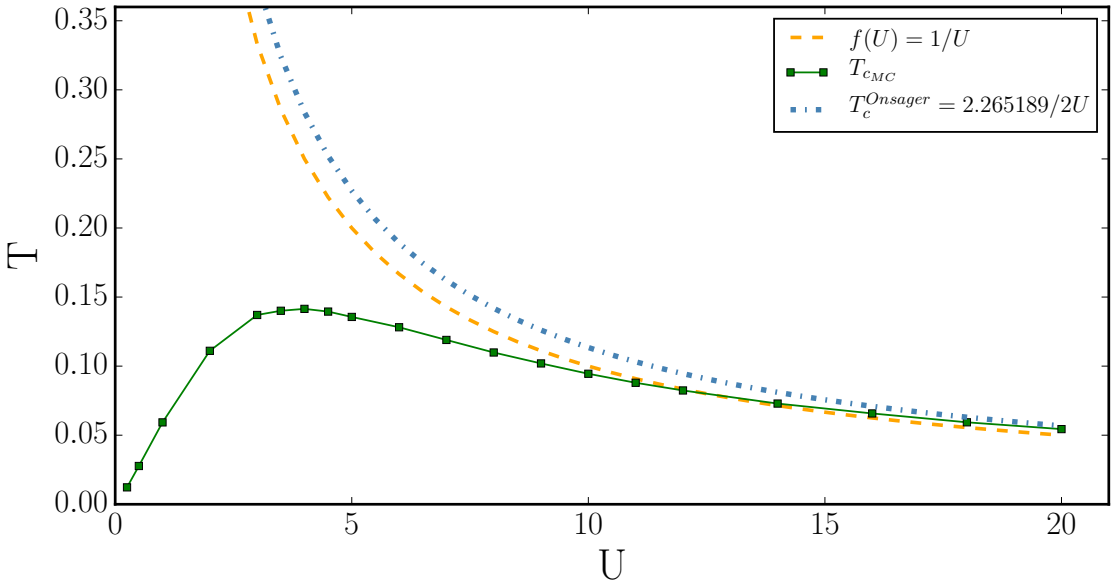

FIGURE 3.4: transition temperature in comparison with numerical result (green curve with dot), the orange curve show the behavior of $f(U) = \frac{1}{U}$ and the dashed blue curve is the transition temperature calculated from a perturbative approach for the FKM. Two other curves are for comparison. as you can see from the figure at large U both the numerical and perturbative approaches are in correspondence with each other.

3.4 Details of the Phase diagram

In this section, we start by introducing every phase in the full phase diagram, see Fig. 3.1, of the model at half-filling. Before we focus on each phase, let us to put introduce neccesary concepts such that we can give a clear description of each phase.

Fermi Gass (FG) At $U = 0$

The model describes a trivial Fermi gas with $\lim_{\omega\to 0} \mathrm{DOS}(\omega) = \text{const}$, illustrated in Fig. 3.5(h). The real part of the conductivity $\sigma'(\omega)$ has unitary Drude weight, i.e. $\sigma'(\omega) = D\delta(\omega)$ with $D = 1$. Fig. 3.6(f) shows that for any finite temperature $D = 0$ for $U > 0$. As in the infinite dimensional case [92], this phase is unstable for any T.

Weak Localized/Anderson Insulator (WL/AI)

The is an interesting region overlooked in previous studies. The effect of the f-electron averaging enters as a disorder potential for the c species and induces an Anderson localization of the single particle eigenstates at low energies. Here, for sufficiently small U and any finite L, the localization length becomes of the order of the volume. In both regions we observe a finite DOS at zero energy, i.e.

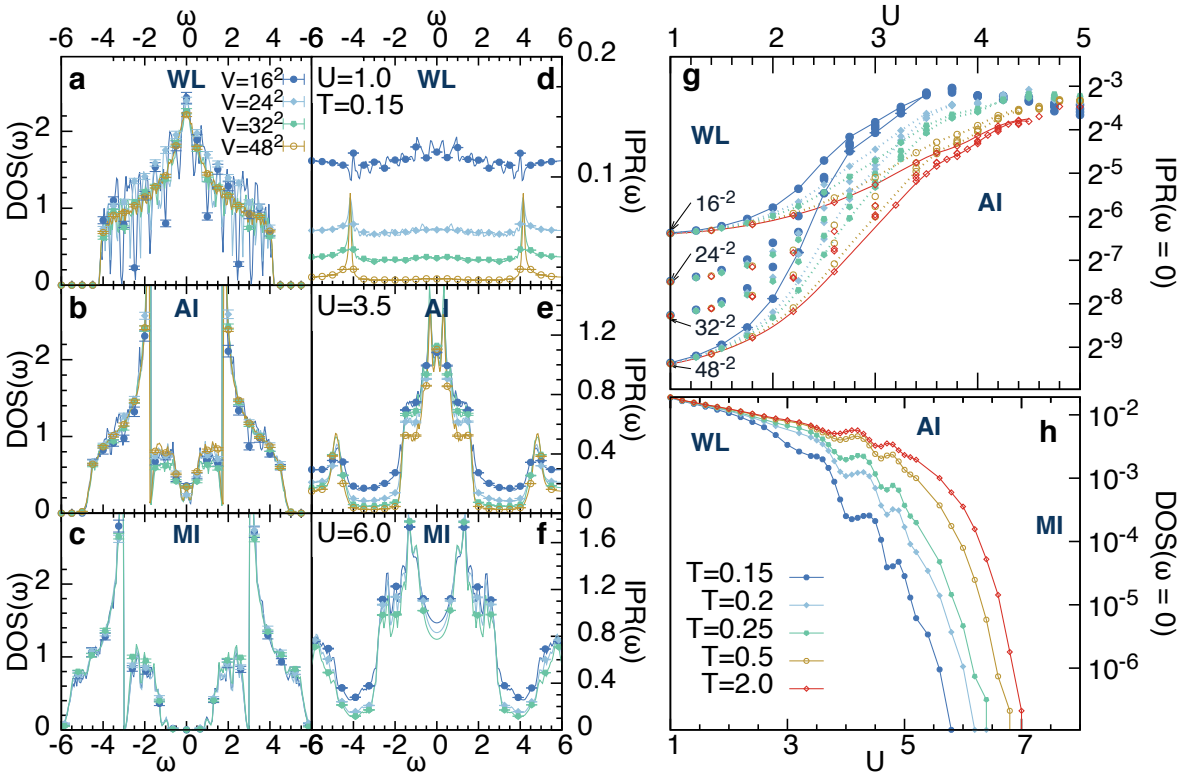

FIGURE 3.5: **a-c**, DOS and **d-f**, IPR as a function of frequency ω at $U = 1, 3.5, 5.25$, $T = 0.15$ and system sizes $16^2, 24^2, 32^2, 48^2$. **g**, IPR and **h**, DOS at $\omega = 0$ as a function of U at different temperatures and system sizes. DOS(0) is independent of system size.

$\lim_{\omega\to 0} \mathrm{DOS}(\omega) \neq 0$, see Fig. 3.5-(a,b). This is further corroborated by the results presented in Fig. 3.5 (h), where we performed the binning of the DOS within a fixed energy window around the Fermi level to avoid any ambiguity with the artificial broadening of δ-peaks. At $T < 1$ and $2 \leq U \leq 7$, the DOS acquires temperature dependence, which is attributed to non-local fluctuations due to proximity to the CDW phase [89, 90]. The behavior of the IPR can be seen in Fig. 3.5-(d-f) to differ in the two regimes: in the WL throughout the spectrum we find IPR strongly dependent on the system size, $\mathrm{IPR}(\omega) \propto V^{-1}$, except at the band edges, signaling predominantly delocalized states. In the AI region, on the other hand, we find $\mathrm{IPR}(\omega) \propto V^0$ for ω in a finite window around zero, $|\omega| < \Delta_{\mathrm{ME}}$ marking the localized region of the spectrum. The low-energy states are localized. With further increase of U this energy window expands, while the density of localized states decreases and approaches zero at the MI phase. Fig. 3.5 (g) shows that the $\mathrm{IPR}(0)$ as a function of U has a V^{-1} scaling at small U and an approximate crossing point at larger U. This crossing point is only weakly dependent on L^2 and was used to extract the approximate crossover line, shown in Fig. 3.1.

The conducting properties of WL/AI phase are studied in Fig. 3.6, which shows the real part of the conductivity $\sigma'(\omega)$ as a function of ω at $T = 0.5$. In the WL region (Fig. 3.6 (a,b)), σ' is zero at $\omega = 0$, but the finite size scaling at small ω and $L \leq 48$ implies that $\lim_{\omega\to 0^+} \sigma'(\omega) \to$ const. In the AI region (Fig. 3.6(c,d)), no such scaling takes place, and $\sigma'(0) = 0$. We observe $\sigma'(\omega) \propto e^{-\Delta_{\mathrm{ME}}/T} a(\omega)$ where Δ_{ME} is the energy gap between the Fermi level and the energy of the first delocalized state $\mathrm{IPR}(\omega \lesssim \Delta_{\mathrm{ME}}) \propto V^{-1}$ and a is roughly linear with frequency at $\omega \to 0$. This temperature dependence is therefore compatible with that for activated hopping (Fig. 3.6e).

Mott Insulator (MI) At high temperatures and sufficiently large U

This Mott-like phase sets in where the c-electrons develop a charge gap, $\mathrm{DOS}(\omega = 0) = 0$ for $|\omega| < \Delta$, while charge order is absent, see Fig. 3.5(c). This phase is adiabatically connected to the point $t/U = 0$ where $\Delta = U$ is the energy cost associated with occupying a c-electron site with $n_{f,\mathbf{r}} = 1$.

Charge Density Wave (CDW)

For any non-zero interaction $U \neq 0$ spontaneous symmetry breaking takes place as temperature is lowered below T_{CDW} leading to a long-range checkerboard-ordered phase, see Ref. [79] and Table 3.1. This phase is characterized by a zero-temperature gap around $\omega = 0$, i.e. $\mathrm{DOS}(\omega, T \to 0) = 0$ for $|\omega| < \Delta$ with a charge gap $\Delta = U$. Within this phase, exact DMFT results for $d \to \infty$ reported a more complex internal structure with some sub-phases including sub-gap states at small U [93, 94, 95].

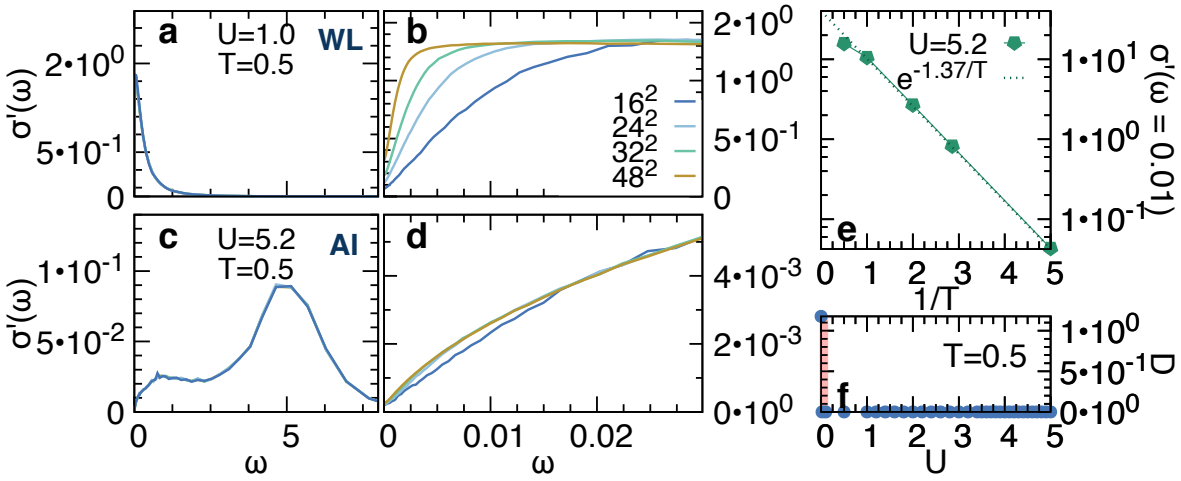

FIGURE 3.6: **a,b,c,d,** Real part of the AC conductivity $\sigma'(\omega)$ as a function of frequency ω at $T = 0.5$, $U = 1.0$ (a, b), 5.2 (c,d). Panels (b),(d) show $\sigma'(\omega)$ for $|\omega| \leq 0.025$ at different system sizes. **e**, The temperature dependence of σ' at $\omega = 0.01$ and $U = 5.2$. **f**, Drude weight D as a function of U at $T = 0.5$.

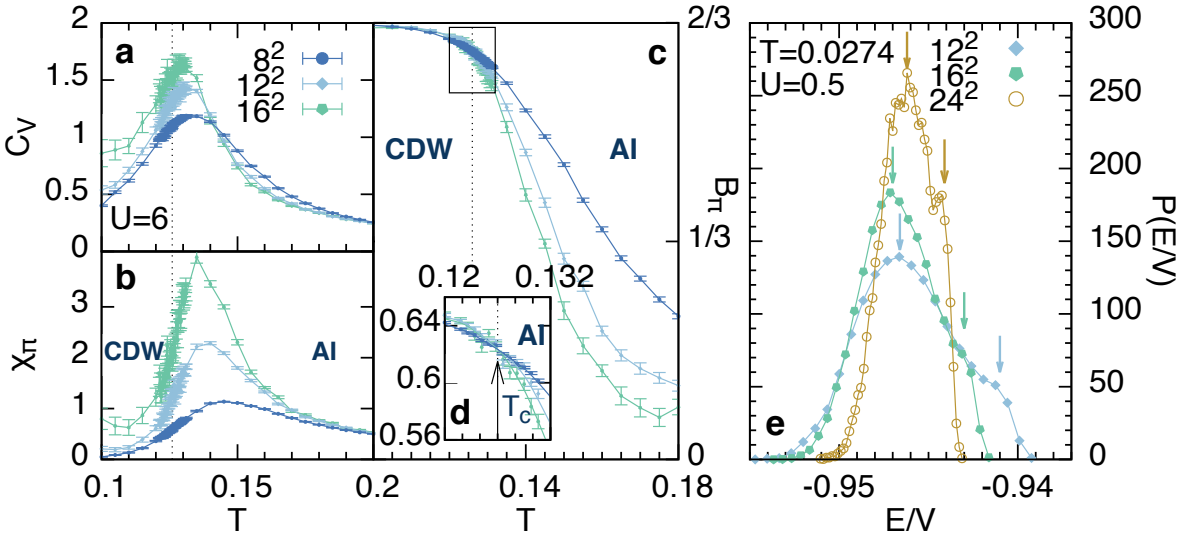

FIGURE 3.7: **a,b,c,** Specific heat, f-electron susceptibility and Binder cumulant for momentum $q = \{\pi, \pi\}$ at $U/t = 6$ and volumes $8^2, 12^2, 16^2$, illustrating the phase transition to the CDW state. Dashed arrow is the transition temperature T_{CDW} obtained by the crossing of the Binder-cumulant curves, shown in Fig. 3.8d. **e,** The distribution of energy values at the proximity of transition temperature to CDW-state at $U = 0.5$, $T = 0.0274$ and system sizes $12^2, 16^2, 24^2$. The existence of two maximums shown by vertical arrows indicate the first-order phase transition, which weakens with increasing system size.

3.5 Transition between different regions

We now turn to a discussion of the nature of the transitions between different regions of phase space.

CDW transition - at large U

We find a previously reported transition between a disorder state at large T and a CDW at small T [82]. The transition between the two is of Ising universality with an order parameter given by the staggered f-occupation $\phi_{\rm st} = \sum_{\boldsymbol{r}} e^{i[\pi,\pi].\vec{r}}(2n_{f,\boldsymbol{r}} - 1)$ as illustrated in Figs. 3.8(a-b) by the T-dependence of specific heat C_v and f-electron susceptibility at momentum $\vec{Q} = [\pi, \pi]$ for $U = 6$.

U	T_c	ν	γ
3.0	0.1370	0.97 ± 0.07	1.76 ± 0.02
5.0	0.1339	0.92 ± 0.11	1.74 ± 0.07
7.0	0.1171	1.00 ± 0.11	1.74 ± 0.07
10.0	0.0951	1.02 ± 0.02	1.73 ± 0.07
12.0	0.0824	1.02 ± 0.17	1.74 ± 0.07

TABLE 3.1: Critical exponents γ (susceptibility) and ν (correlation length) of the CDW transition for different values of U. The Ising exponents are $\gamma = 1.75$ and $\nu = 1$.

In fact, for large U, an exact mapping to the 2d-Ising model can explicitly be given [82]. Numerically, the transition temperature is determined by the crossing of the Binder cumulant $B_Q(L)$ [96], see Figs. 3.8(c-d). Upon decreasing U, the high temperature disorder phase evolves from a MI to an AI, but the nature of the transition into the CDW state is maintained, as highlighted by the Ising exponents, see Table 3.1.

In agreement with previous studies we find that for $0 < U \lesssim 3$, the phase transition appears to be first order [79]. This is illustrated by the double peaked energy histogram in Fig. 3.8e with maxima denoted by arrows. Interestingly, the disappearance of the double peak at $U \approx 3$ coincides with the WL-Al crossover of the high temperature phase. The finite size scaling of Fig. 3.8e shows that the first order nature of the transition weakens with increasing system size implying a continuous transition in the infinite volume limit. This provides further evidence that the occurrence of the WL phase is a finite size effect. In the thermodynamic limit the AI phase extends until $U \to 0^+$ and the transition into the charge-ordered state is continuous for all values of $U > 0$.

AI-MI transition

The existence of this transition in the FK model has not been reported previously. The MI is characterized by $\mathrm{DOS}(0) = 0$. As U is reduced the onset of the AI phase

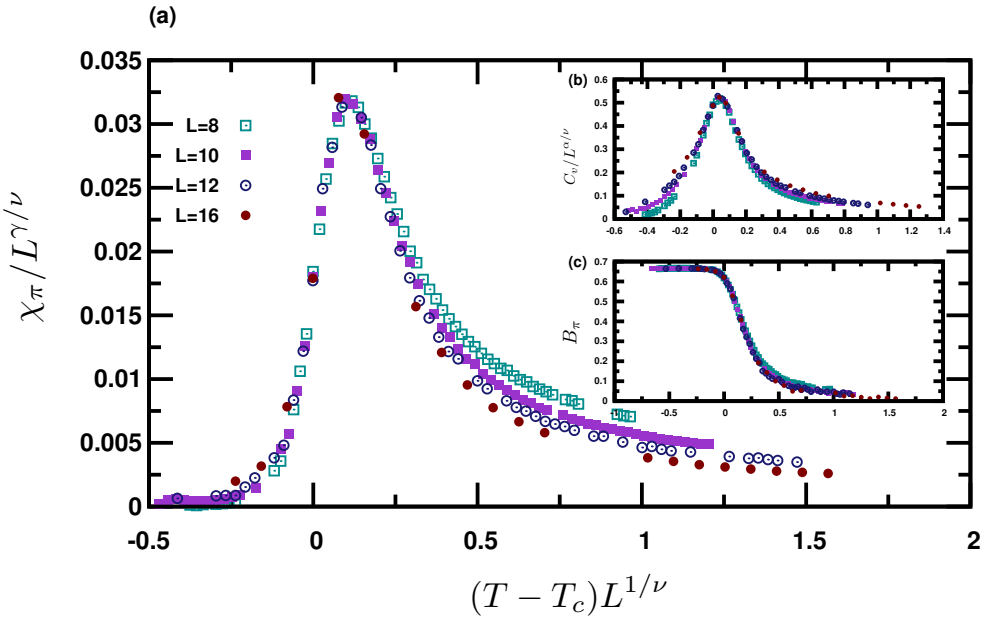

FIGURE 3.8: **a,b,c,** Finite size scaling results for specific heat, f-electron susceptibility and Binder cumulant for momentum $\vec{Q} = [\pi, \pi]$ at $U/t = 10.0$ and volumes $8^2, 10^2, 12^2, 16^2$, illustrating the phase transition to the CDW state with Ising universality class. The critical exponents are presented in table 3.1.

can be best read off by DOS$(0) > 0$, as illustrated in Fig. 3.5h, while $\sigma'(0) = 0$ [3]. As the f-electrons act as static scattering potentials the grand canonical partition function of the FK model can be understood as that of annealed disorder. Across the transition f-electron observables remain smooth. For asymptotically large temperatures FK maps to a binary random disorder model previously studied in the context of binary alloys [97, 98] where transitions similar to the AI-MI transition have previously been observed. Our results suggest that for finite temperature the universal features of the AI-MI transition are the same as the infinite temperature ones and the annealed nature of the disorder plays no qualitative role in this regime.

WL-AI crossover

This crossover turns out to be a feature of finite system size. The crossover is reflected in the AC conductivity and is also clearly visible in the IPR$(\omega = 0)$ which displays qualitatively different behavior in the WL, AI and MI phases. As discussed above, at large temperatures, the nature of the disorder is not relevant as all possible configurations of the f electrons are equally probable. Therefore, results resembling those of quenched disorder are to be expected. For 2D these imply the existence of a so-called weak localized regime where the localization length $\zeta \sim 1/\text{IPR}(\omega = 0)$ depends on the coupling constant U in an exponential fashion [99]. Therefore, for

[3] We used the numerical criterion of DOS$(0) > 10^{-7}$ in our energy units of t

any finite system of linear size L and sufficiently small U, there is a regime where $L < \zeta$. In this case, the system displays properties of a bad metal.

3.6 Discussion

Having described the overall phase diagram of the two-dimensional half-filled FK model we now turn to a discussion of the significance of our findings. The fact that $\sigma'(\omega \to 0^+) \neq 0$ in the temperature range above the charge ordered state at small U, see Fig. 3.1, suggests the identification of the WL regime with the previously reported metallic phase of the model [55, 79]. As shown above this regime is a feature of the finiteness of the underlying lattice and vanishes in the thermodynamic limit. Within the DMFT, the metallic phase originates from a finite local DOS$(\omega = 0)$ and the neglect of spatial correlations [55, 89]. The AI phase is captured by disorder extensions of the DMFT with the addition of quenched disorder [100, 101, 102, 103, 104].

In this chapter, we primarily addressed the intricacies of the phase diagram above the charge ordering transition. Naively, the onset of charge order with propagation vector $\vec{Q}$ in the weakly interacting or small U regime is associated with the instability due to a perfectly nested Fermi surface. Although DOS$(\omega = 0) \neq 0$, the absence of a Fermi surface implies that even for arbitrarily small U this CDW picture cannot apply, when coming out of the AI phase. It thus might be worthwhile to extend our analysis to the charge ordered part of the phase diagram. Interestingly, as can be read off from Table 3.1, the critical exponents associated with the onset of charge order in that region coincide with those of the classical two-dimensional Ising model. This raises the possibility that ordering transitions, traditionally interpreted within the Stoner theory of delocalized electrons, should be better described within a strong-coupling framework. This relates to the on-going debate between the weak- or strong-coupling nature of the onset of order near the emergence of superconductivity in *e.g.* the iron-based superconductors and the heavy fermions [105, 106].

Our results may also shed some light on the finite temperature phase diagram of the three-dimensional half-filled Hubbard model, where at low temperature an antiferromagnetic phase sets. Ignoring the dynamic nature of the antiferromagnetic order parameter the system can be described by a static model with annealed vector disorder. Thus, one may expect an Anderson localized phase at high temperatures separating the weak coupling metallic phase from the Mott insulator at large U. A recent study of the Anderson-Hubbard model with spin-dependent disorder leads to FK-like physics in parts of the phase diagram [107] to which our findings may be relevant.

Finally, we note that our results may be directly relevant to studies of localization in cold atoms [108, 109, 110]. The model serves as a prototype for recent implementations of mass unbalanced fermions in optical lattices [111, 112, 113] and the physical properties of the model extend past the infinite mass ratio regime [114,

115]. It would be interesting to see an experimental confirmation of the existence a the localized phase for a translational-invariant system in the absence of explicit disorder. A direct verification with ultracold atoms systems should be possible with state-of-the-art technology.

Chapter 4

Spatial Structure of Entanglement

spooky action at a distance.
—Albert Einstein

In this chapter we map out the spatial entanglement structure of a low-dimensional quantum system, the transverse-field Ising chain, both in the ground state and in thermal states. For this purpose we use the logarithmic negativity [116, 117, 118, 119, 120, 121, 122], which shares many of the central features of the entanglement entropy in pure states, such as the area law for ground states of gapped Hamiltonians [123, 124, 125] or universal contribution appearing at quantum critical points [126, 39, 127]. In contrast to the entanglement entropy, however, the logarithmic negativity remains an entanglement measure also for mixed states [39, 127, 122]. In order to obtain information about the spatial entanglement structure, we study the logarithmic negativity of two disjoint blocks of identical size ℓ as a function of their separation d, which can be viewed as the entanglement analog to a conventional quantum correlation function. For an illustration of our setup see Fig. 4.1 (a). We find that for any fixed size ℓ of the two blocks there appears a sharp entanglement threshold d^* beyond which the logarithmic negativity vanishes identically. For larger distance than d^* the two blocks become unentangled, accordingly, as measured by the logarithmic negativity. In Fig. 4.1 (b) we show the results for the entanglement threshold d^* as a function of ℓ for different parameters of the transverse-field Ising chain, where one can see that the spatial extent of entanglement is restricted to rather short distances even when the system resides at the quantum phase transition where quantum correlations are long-ranged.

While for the case where the two blocks consist of single qubits this result is well known [128, 129, 130, 131, 132], here we study systematically the crossover from the single-particle to the multi-particle case. We compute the logarithmic negativity numerically for large systems using the Time Evolving Block Decimation (TEBD). In addition, we develop a simple effective model explaining our numerical observations.

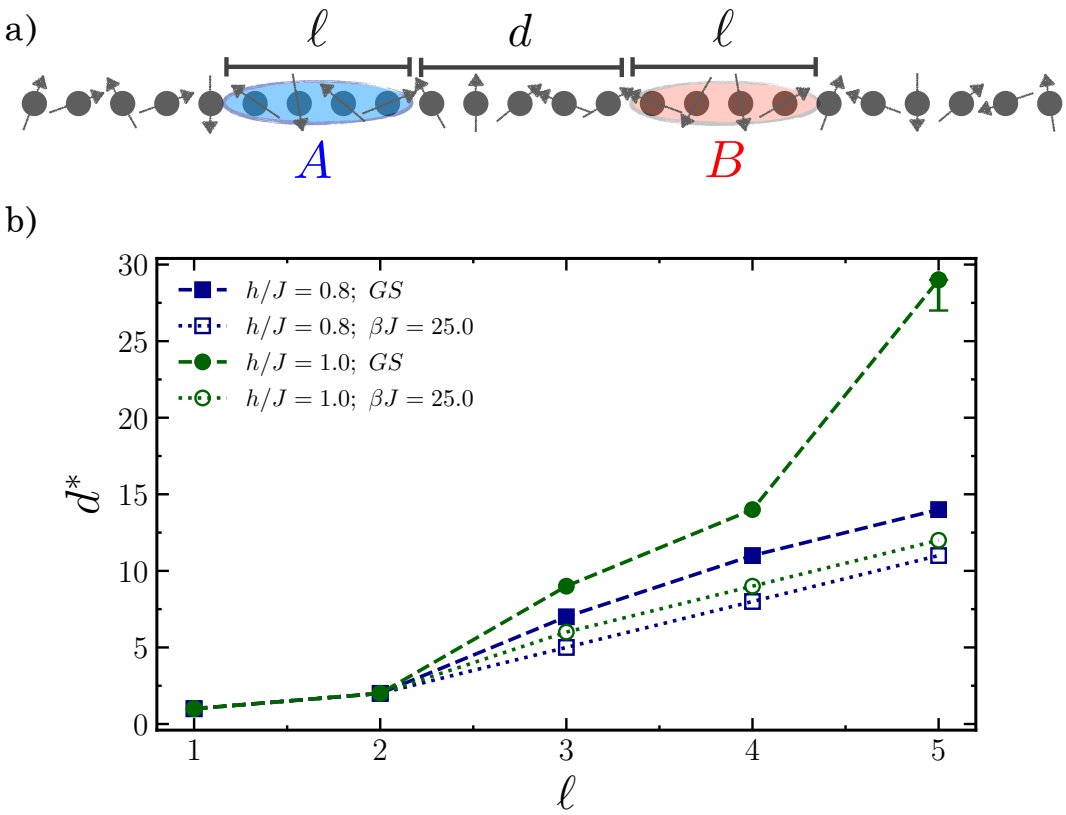

FIGURE 4.1: a) Illustration of the setup used in our work. We consider two spatial regions A and B in a large chain each of which contains ℓ sites. The two regions are separated by a distance d, illustrated here for $\ell = 4$ and $d = 5$. b) Results for the entanglement threshold d^* beyond which distance logarithmic negativity vanishes. We show d^* as a function of block size ℓ for the ground state (GS) and for a thermal state at the inverse temperature $\beta J = 25$. For $\ell = 5$ in the ground state we can only give a lower bound on d^* which we indicate in this plot by adding an error bar.

4.1 Definition of Entanglement

Definition 1.

Let $|\Psi\rangle$ be a state of many physical systems and $|\Phi_i\rangle$ a state in system i. Then, $|\Psi\rangle$ is called entangled if it cannot be expressed as a product of $|\Phi_i\rangle$ for any set of $|\Phi_i\rangle$.

If $|\Psi\rangle$ is not entangled, it is called separable. If $|\Psi\rangle$ is a product of $|\Phi_i\rangle$, $|\Psi\rangle$ is called a product state. All product states are separable. For example, one can easily

check that the following state $|\Psi\rangle$ is entangled

$$|\Psi\rangle = \frac{|11\rangle + |00\rangle}{\sqrt{2}} \neq \underbrace{(a|1\rangle + b|0\rangle) \otimes (a'|1\rangle + b'|0\rangle)}_{=aa'|11\rangle + ab'|10\rangle + ba'|01\rangle + bb'|00\rangle} \tag{4.1}$$

Another Approach

A second, more experimentalist approach to the definition of entanglement is based on the way how entanglement can be obtained. Consider two experimental setups A and B. As these setups are separate, they may only apply local operations. They may use classical communication to coordinate those operations. Then, entanglement can be defined by these operations[133]:

Definition 2.

If a shared state ρ can be obtained by two parties A and B using only local operations and classical communication, ρ is a separable state.

Note that these two definitions of entanglement are equivalent.

4.2 Entanglement Measures

An entanglement measure quantifies how much entanglement is contained in a quantum state. Formally it is any nonnegative real function of a state which can not increase under local operations and classical communication (LOCC) (so called monotonicity), and is zero for separable states[134, 135]. Here we introduce several entanglement measures which can be useful in condensed matter physics.

4.2.1 Density matrices and entanglement

Here, we give a short reminder of density matrices, also so called density operators, which conceptually take the role of state vectors. They encode all the accessible information about a quantum mechanical system. The entanglement structure just discussed can also be found from the density matrices associated with the state $|\Psi\rangle$. This is in fact, the standard way to obtain it.

Definition

In general a density operator ρ can be defined as

$$\rho = \sum_i p_i |\psi_i\rangle\langle\psi_i|, \tag{4.2}$$

where p_i is the probablity that the system is in $|\psi_i\rangle$ with $\sum_i p_i = 1$. Note that $|\psi_i\rangle$'s need not be orthonormal and decomposition is not unique. This density matrix has the following properties:

- $\rho^2 = \rho$ projector
- $\rho^\dagger = \rho$ hermiticity
- $\mathrm{Tr}\rho = 1$ normalization
- $\rho \geq 0$ positivity

Pure and mixed state

A pure quantum state defines as a vector state $|\psi_i\rangle$ in Hilbert space and density matrix for such a state is

$$\rho = |\psi_i\rangle\langle\psi_i| \text{ and } \mathrm{Tr}(\rho^2) = 1. \tag{4.3}$$

A mixed quantum state defines as a probabilistic mixture of a pure state

$$\rho = \sum_i p_i \rho_i^{pure} = \sum_i p_i |\psi_i\rangle\langle\psi_i| \text{ and } \mathrm{Tr}(\rho^2) < 1. \tag{4.4}$$

Thermal states: thermal states are special case of mixed states. Introducing a Hamiltonian $H = \sum_{n=1}^{D} E_n |n\rangle\langle n|$ we can think of this classically, as saying that state nth has energy E_n. The boltzmann distribution at temperature T is $p_n = e^{-\beta E_n}/Z$, where $Z = \sum_{n=1}^{D} e^{\beta E_n}$ with $\beta = 1/k_B T$ and k_B is Boltzmann's constant. In quantum setting the density matrix becomes

$$\rho = \sum_{n=1}^{D} p_i |E_n\rangle\langle E_n| = \frac{\sum_n^D e^{-\beta E_n} |E_n\rangle\langle E_n|}{Z} = \frac{e^{-\beta H}}{Z}. \tag{4.5}$$

This is known as the Gibbs state or the thermal state. It describes the state of a quantum system at thermal equilibrium.

Reduced density matrices (RDM)

If we denote the total density matrix with

$$\rho = |\Psi\rangle\langle\Psi|, \tag{4.6}$$

one can, for a chosen division, take the trace over the degrees of freedom in one part of the system. This gives the reduced density matrix for the other part, i.e.

$$\rho_A = \mathrm{Tr}_B(\rho) \ , \ \rho_B = \mathrm{Tr}_A(\rho). \tag{4.7}$$

These hermitian operators can be used to calculate arbitrary expectation values in the subsystems. Moreover, one can write them based on their diagonal form, see appendix B

$$\rho_\alpha = \sum_n |\lambda_n|^2 |\Phi_n^\alpha\rangle\langle\Phi_n^\alpha| \ , \ \alpha = A, B, \tag{4.8}$$

this leads to two features

1. ρ_A and ρ_B have the same non-zero eigenvalues
2. these eigenvalues are given by $w_n = |\lambda_n|^2$

Therefore the eigenvalue spectrum of the ρ_α gives directly the weights in the Schmidt decomposition and a glance at this spectrum shows the basic entanglement features of the state, for the chosen bipartition. One also sees that the $|\Phi_n^\alpha\rangle$ are the eigenfunctions of the ρ_α. For the single-particle RDM's mentioned in the introduction, these eigenfunctions are known as "natural orbitals" in quantum chemistry[136].

4.2.2 Entanglement Entropy

Whereas the full RDM spectra give the clearest impression of the entanglement in a bipartite system, it is clever to have a simple measure which encode this information into one number. This can be achieved by generalizing the usual (von Neumann) entropy definition to reduced density matrices. This so called entanglement entropy S. It measures a mutual connection between two parts of a system and therefore defines[1]

$$S(\rho_A) = S(\rho_B) = -\mathrm{Tr}(\rho_A \log_2 \rho_A) = -\mathrm{Tr}(\rho_B \log_2 \rho_B) = -\sum_n w_n \log_2 w_n \tag{4.9}$$

The most important features are

- S only meaures the entanglement for pure state
- S is the standard meaure for entanglement in condensed matter physics for bipartitions. It is based on spectrum of ρ_A which is identical to the spectrum of ρ_2. Thus $\rho_A = \rho_B$ holds for an arbitrary bipartition
- S vanishes for product states, and has a maximal value of $S = \log_2 D$ if one has D non-zero eigenvalues which are all equal, $w_n = \frac{1}{D}$ for $n = 1, 2, \ldots, D$.

[1]Note that in this thesis, we use $\log_2$ instead of logarithm in natural basis $\log_e \equiv \ln$. Both cases reach to same results and doesn't affect the physics.

4.2.3 Rényi Entropy

Another bipartite entanglement measure is the Rényi entanglement entropy S_α. It is also defined in terms of the reduced density matrices, and a Rényi index $\alpha \geq 0$. The generalized Renyi entanglement entropies are definea by

$$S_\alpha(\rho_A) = \frac{1}{1-\alpha} \ln \mathrm{Tr}(\rho_A^\alpha) \quad \text{and} \quad \alpha \in \mathbb{N} \tag{4.10}$$

In the limit $\alpha \to 1$, the Renyi entanglement entropy approaches the Von Neumann entanglement entropy. For $\alpha \geq 0$ and $\alpha \neq 1$, can be an entanglement measure for mixed state. Recently, the generalized Rényi entropies have attracted considerable attention in the condensed-matter community, due to their ability to encode information about the whole entanglement spectrum of ρ_A, i.e., this allows the set of S_α to contain much more information than $S_{\alpha=1}$ alone. The Rényi entanglement entropy can be computed in quantum Monte Carlo simultions[137].

4.2.4 Relative Entropy of Entanglement

The relative entropy $S(\rho \parallel \sigma)$ between two states ρ and σ is defined as

$$S(\rho \parallel \sigma) = \mathrm{Tr}[\rho(\log_2 \rho - \log_2 \sigma)], \tag{4.11}$$

which is evidently not symmetric under exchange of ρ and σ, and is non-negative, i.e., $S(\rho \parallel \sigma) \geq 0$. By knowing this, one can define the relative entropy of entanglement as an entanglement measure that quantifies how much a given entangled state is distinguished operationally from the set of separable states or those with positive partial transposition(PPT). For more information about PPT, see appendix C

$$E_R(\rho) = \min_{\sigma \in \mathcal{D}} S(\rho \parallel \sigma), \tag{4.12}$$

where $\mathcal{D}$ denotes the set of all separable states and the minimum is taken over the family of separable states. The task of finding the relative entropy of entanglement for arbitrary states ρ involves a minimization over all separable states, and this renders the computation of this entanglement measure very difficult[138, 139].

4.2.5 Entanglement of Formation

The entanglement of formation represents the minimal possible average entropy of all pure state decompositions. Given a density matrix ρ of a pair of quantum systems A and B, consider all possible pure-state decompositions of ρ, that is, all ensemble of states $|\psi_i\rangle$ with probablities p_i as in Eq. 4.4

$$\rho = \sum_i p_i |\psi_i\rangle\langle\psi_i|.$$

For each pure state, the entanglement S is defined as the entropy of either of the two subsystems A and B as we explained in Eq. 4.9

$$S(\rho) = -\mathrm{Tr}(\rho_A \log_2 \rho_A) = -\mathrm{Tr}(\rho_B \log_2 \rho_B)$$

The entanglement of formation of the mixed state ρ is then defined as the average entanglement of the pure states of the decomposition, minimized over all decompositions of ρ

$$E(\rho) = \min \sum_i p_i S(\rho_i). \tag{4.13}$$

A state ρ is separable if and only if $E(\rho) = 0$ and hence can be represented as a convex combination of product states as $\rho = \sum_i p_i \rho_i^A \otimes \rho_i^B$, where ρ_i^A and ρ_i^B are pure state density matrices associated to the subsystems A and B.

4.2.6 Concurrence

Anothe entanglement measure that one can calculate the entanglement of formation from it is concurrence[140, 141]. The concurrence is an entanglement monotone defined for a mixed state of two qubits as

$$\mathcal{C}(\rho) = \max(0, \lambda_1 - \lambda_2 - \lambda_3 - \lambda_4) \tag{4.14}$$

in which $\lambda_1, \ldots, \lambda_4$ are the square roots of the eigenvalues, in decreasing order, of the product matrix R[2] between two qubits[141, 142]

$$R = \rho\tilde{\rho}, \tag{4.15}$$

where $\tilde{\rho} = (\sigma_y \otimes \sigma_y)\rho^*(\sigma_y \otimes \sigma_y)$ is the spin-flipped matrix of ρ and σ_y is the Pauli matrix. Note that the two qubits can be at any distance from each other. To compute it, one need to access the reduced density matrix between them.

4.3 Logarithmic Negativity

The aim of this work is to study the spatial structure of entanglement in equilibrium states of the transverse-field Ising chain as depicted in Fig. 4.1. The entanglement entropy, which is the paradigmatic entanglement measure for the characterization of quantum many-body systems in ground states, cannot be used for that purpose since it can only access the entanglement between a subsystem and its remainder, but not the entanglement between two subsystems. Here instead, we use the logarithmic negativity $\mathcal{E}_\mathcal{N}$.

Let us denote by ρ the density matrix of the system, which can be either pure or mixed. To compute the logarithmic negativity, it is necessary to access the reduced

[2] R is a non-Hermitian matrix

density matrix $\rho_{A,B}$ of two subsystems A and B which can be obtained from ρ by tracing out all the degrees of freedom not belonging to A or to B:

$$\rho_{A,B} = \mathrm{Tr}_{\overline{AB}}\, \rho. \tag{4.16}$$

Here, $\mathrm{Tr}_{\overline{AB}}$ denotes the trace over the complement $\overline{AB}$ of A and B. The reduced density matrix $\rho_{A,B}$ can be represented as

$$\rho_{A,B} = \sum_{\substack{\mu,\nu \\ m,n}} C^{\mu,\nu}_{m,n} |\mu\rangle\langle\nu| \otimes |m\rangle\langle n|, \tag{4.17}$$

where $|\mu\rangle$ and $|\nu\rangle$ label the basis states of the local Hilbert space $\mathbb{H}_A$ of subsystem A, and $|m\rangle$ and $|n\rangle$ of $\mathbb{H}_B$ accordingly. $C^{\mu,\nu}_{m,n}$ are the coefficients given by $C^{\mu,\nu}_{m,n} = \langle\mu, m|\rho_{A,B}|\nu, n\rangle$.

The logarithmic negativity is an entanglement measure based on the positive partial transpose (PPT) criterion [143, 144], which provides a necessary condition for ρ_{AB} to be separable and therefore to contain no entanglement. Central to the PPT criterion is the partial transpose operation T_B performed on one of the two subsystems, B say:

$$\rho^{T_B}_{A,B} = [I_A \otimes T_B]\rho_{A,B} = \sum_{\substack{\mu,\nu \\ m,n}} C^{\mu,\nu}_{n,m} |\mu\rangle\langle\nu| \otimes |m\rangle\langle n|, \tag{4.18}$$

which leaves the basis states in A unchanged but performs a transpose on B. In the end, this operation is equivalent to $C^{\mu,\nu}_{m,n} \to C^{\mu,\nu}_{n,m}$ when comparing Eq. (4.17) with Eq. (4.18). While the eigenvalues of $\rho_{A,B}$ are probabilities and therefore non-negative real numbers, this is not necessarily the case for the partially transposed $\rho^{T_B}_{A,B}$. When $\rho_{A,B}$ is separable and therefore contains no entanglement, the eigenvalues λ of $\rho^{T_B}_{A,B}$ have to be non-negative, which is the aforementioned PPT criterion. In turn, this means that in case there exists a negative eigenvalue of $\rho^{T_B}_{A,B}$, the reduced density matrix $\rho_{A,B}$ has to be entangled. The logarithmic negativity $\mathcal{E}_\mathcal{N}$ quantifies to which extent the partially transposed density matrix ρ^{T_B} between two subsystems fails to be non-negative. More specifically, $\mathcal{E}_\mathcal{N}$ is defined as

$$\mathcal{E}_\mathcal{N} = \log_2 \|\rho^{T_B}\|_1 = \log_2 \left[1 + \sum_\lambda (|\lambda| - \lambda)\right], \tag{4.19}$$

where $\|.\|_1$ denotes the trace norm, and λ the eigenvalues of $\rho^{T_B}_{AB}$. In general, the PPT criterion is only a necessary but not a sufficient criterion for entanglement, i.e., there might be states that signal a vanishing logarithmic negativity that are, however, not separable. In this context it is important that $\mathcal{E}_\mathcal{N}$ constitutes an upper bound to the distillable entanglement [145]. A vanishing $\mathcal{E}_\mathcal{N}$ therefore means that such a Bell pair distillation is not possible.

For quantum many-body systems the logarithmic negativity has been studied

extensively in the literature [117, 118, 143, 116, 146, 147, 148]. In particular, it has been found that $\mathcal{E}_{\mathcal{N}}$ displays the same universal contributions at quantum critical points [126, 39, 127], as does the entanglement entropy [126, 40, 124]. In particular, the logarithmic negativity for two adjacent large blocks of size ℓ_1 and ℓ_2 becomes [126]

$$\mathcal{E}_{\mathcal{N}} \sim \frac{c}{4} \ln \left[\frac{\ell_1 \ell_2}{\ell_1 + \ell_2} \right], \tag{4.20}$$

with c the central charge of the corresponding conformal field theory, which is a universal property of the underlying quantum phase transition. For $\ell_2 \to \infty$, a situation which is equivalent to measuring the entanglement between a subsystem and its remainder, one obtains $\mathcal{E}_{\mathcal{N}} \sim (c/4)\log(\ell_1)$. The entanglement entropy has been intensively studied analytically [149, 40, 150, 151] and numerically [152, 153, 154, 155, 156] for the ground state of the 1D transverse Ising model. On general grounds the entanglement entropy is characterized by an area law [125, 124, 157], although at the critical point a logarithmic dependence on the size ℓ_1 emerges leading to $S \sim (c/3)\log(\ell_1)$, which has the same functional dependence as the logarithmic negativity.

In the case of disjoint blocks, the set up that we aim to address in this chapter, much less is known in general. Using conformal field theory it is possible to prove that the logarithmic negativity is a scale-invariant quantity at the critical point [126, 158, 159]. Specifically, $\mathcal{E}_{\mathcal{N}}$ is a function only of the dimensionless quantity $y = \frac{(v_1-u_1)(v_2-u_2)}{(u_2-u_1)(v_2-v_1)}$, where u_1, v_1 are respectively the left and right edges of the first block, and u_2, v_2 of the second block.

One case that has been studied already extensively is when each of the two blocks contains a single spin [128, 129, 130, 131, 132]. Then, the entanglement between the two spins exactly vanishes beyond a distance of a few lattice sites, a phenomenon that has been termed 'entanglement sudden death [160, 161]'. How entanglement behaves for disjoint blocks larger than a single spin, is, however, not yet known.

In view of the sudden drop towards vanishing entanglement known for the single-spin case, we introduce in the following the notion of the *entanglement threshold* d^*. We define d^* to be the maximum distance d between two subsystems such that the two systems remain entangled. It is the main goal of this work to study this entanglement threshold in the transverse-field Ising chain[3].

[3]Since we study how the entanglement vanishes, it is important to estimate our numerical accuracy of the program which does not go below 10^{-13}.

4.4 The model

The model we consider is the one-dimensional Ising model with a transverse field (TFIM) described by the following Hamiltonian:

$$H = -\frac{1}{2}\left(J\sum_{i=1}^{L-1}\sigma_i^x\sigma_{i+1}^x + h\sum_{i}^{L}\sigma_i^z \right), \tag{4.21}$$

where J denotes the spin-spin coupling, h the transverse field and $\sigma_i^{x(z)}$ the Pauli matrices acting on the i-th lattice site. For convenience, we set the lattice spacing $a = 1$ and choose open boundary conditions. This model undergoes a quantum phase transition [2, 162] at zero temperature when $J = h$. For $h < J$, the system is in a ferromagnetic phase, while for $h > J$ in a paramagnetic one. The order parameter of the transition is the magnetization $m_x = L^{-1}\sum_l \sigma_l^x$ along the spin-spin coupling direction which is nonzero in the symmetry-broken phase and vanishes in the paramagnetic one. At nonzero temperature a symmetry-broken phase cannot exist for this one-dimensional system according to the Mermin-Wagner theorem [163, 164, 165].

In the following we study the entanglement properties of the transverse-field Ising chain as a function of temperature. Therefore, in general, our system resides in a thermal mixed state given by the density matrix ρ of the canonical ensemble:

$$\rho = \frac{1}{Z}e^{-\beta H}, \tag{4.22}$$

with $\beta = \dfrac{1}{T}$ the inverse temperature, H the Hamiltonian and $Z = \mathrm{Tr}\left(e^{-\beta H}\right)$ the partition function.

4.5 Numerical Approach

Although the TFIM is exactly solvable by mapping the problem to a free fermionic theory using a Jordan-Wigner transformation [2], the computation of the logarithmic negativity remains complicated. The main problems arise when performing the partial transpose operation, which in terms of the fermionic degrees of freedom does not have a solvable structure [166, 167, 119]. Therefore, numerical techniques are required and we use for that purpose the TEBD in the following [57, 168]. Since we aim to study both the ground as well as nonzero temperature states, we use both the pure state matrix product states (MPS) and finite-temperature MPS formalism [169, 170, 171]. In the chapter 2, one can find the full descriptions of these methods that we use in this chapter.

To compute the logarithmic negativity for a generic state $|\psi\rangle$, we need access to the reduced density matrix and its partial transpose. Therefore one needs to compute $\rho = |\psi\rangle\langle\psi|$ and trace out those sites which are not included in the blocks A and

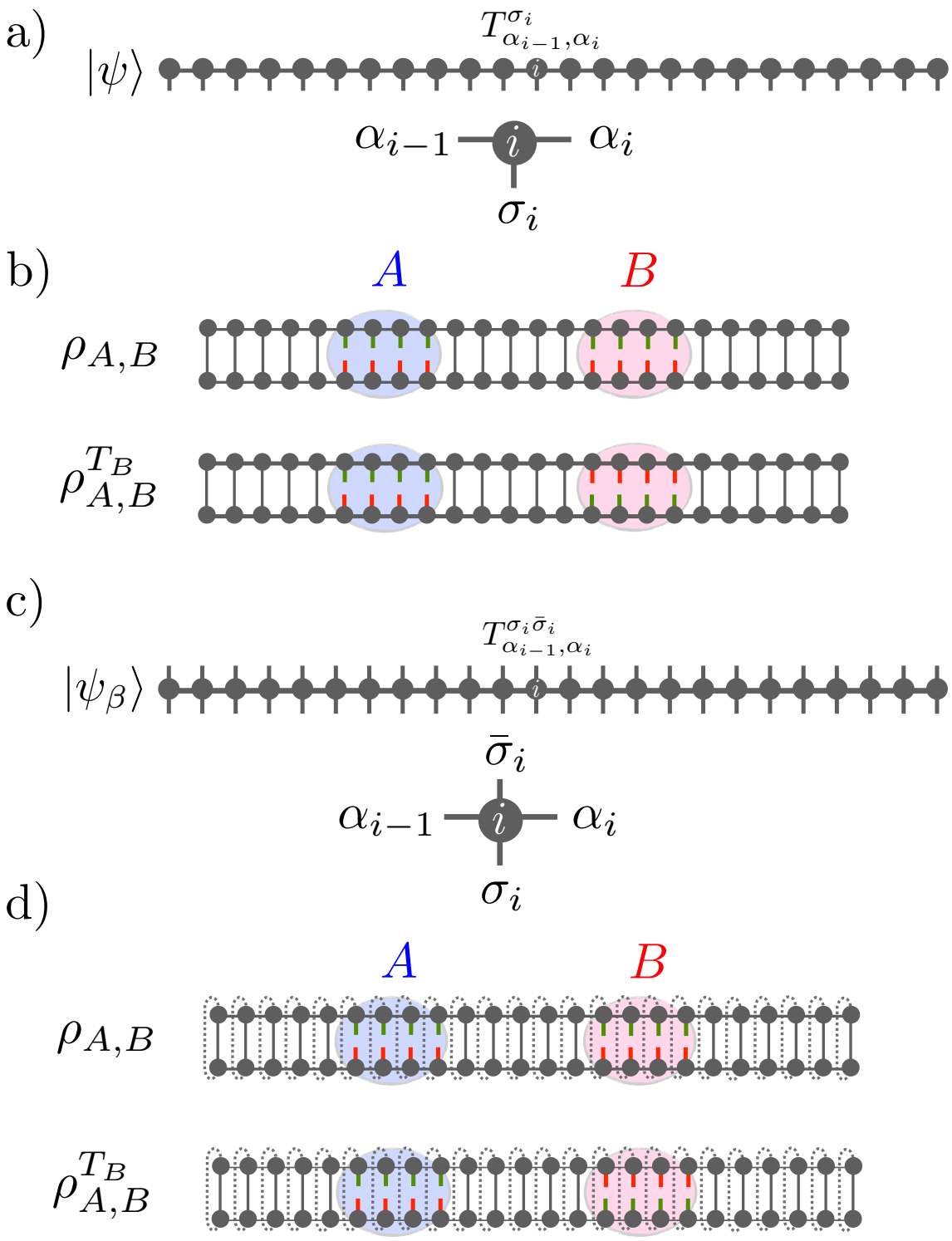

FIGURE 4.2: a) MPS representation of a quantum state $|\psi\rangle$ and its structure at each site i. b) Reduced density matrix representation of two subsystems A and B, i.e., $\rho_{A,B}$ and its partial transpose $\rho^{T_B}_{A,B}$ which is carried out in region B. c) MPS representation of the thermal state $|\psi_\beta\rangle$. Auxiliary degrees of freedom $\bar{\sigma}_i$ have been introduced to purify the thermal state. d) Reduced thermal density matrix between two regions A and B. Note that all other degrees of freedoms have been traced out.

B. As we expained in chapeter 2, the MPS representation of of pure state $|\psi\rangle$ has the following form

$$|\psi\rangle = \sum_{\substack{\sigma_1 \dots \sigma_L \\ \alpha_1 \dots \alpha_{L-1}}} T^{\sigma_1}_{\alpha_1} \dots T^{\sigma_i}_{\alpha_{i-1},\alpha_i} \dots T^{\sigma_L}_{\alpha_{L-1}} \, |\sigma_1 \dots \sigma_i \dots \sigma_L\rangle, \tag{4.23}$$

where each $T^{\sigma_i}_{\alpha_{i-1},\alpha_i}$ is a rank-3 tensor, which therefore depends on the local state $|\sigma_i\rangle$. The MPS representation thermal states which are along with an extra index $\bar{\sigma}_i$ for auxiliary Hilbert space for each site is

$$\begin{aligned} |\psi_\beta\rangle = \sum_{\substack{\sigma_1 \dots \sigma_L \\ \bar{\sigma}_1 \dots \bar{\sigma}_L \\ \alpha_1 \dots \alpha_{L-1}}} & T^{\sigma_1 \bar{\sigma}_1}_{\alpha_1} \dots T^{\sigma_i \bar{\sigma}_i}_{\alpha_{i-1},\alpha_i} \dots \\ & \dots T^{\sigma_L \bar{\sigma}_L}_{\alpha_{L-1}} |\sigma_1 \bar{\sigma}_1 \dots \sigma_i \bar{\sigma}_i \dots \sigma_L \bar{\sigma}_L\rangle. \end{aligned} \tag{4.24}$$

Note that in the case of thermal states the auxiliary degrees of freedom must be traced out. Thus the reduced density matrix and its partial transpose for both pure and thermal states will have the same form. Fig. 4.2 shows the reduced density matrix and its partial transpose using MPS based diagrams.

$$\begin{aligned} \rho_{A,B} = \mathrm{Tr}_{\overline{A,B}}(|\psi\rangle\langle\psi|) = \sum_{\sigma_i,\sigma_i' \in \{A,B\}} & C^{(\sigma_1 \dots \sigma_\ell)_A, (\sigma_1' \dots \sigma_\ell')_A}_{(\sigma_1 \dots \sigma_\ell)_B, (\sigma_1' \dots \sigma_\ell')_B} | \, (\sigma_1 \dots \sigma_i \dots \sigma_\ell)_A, (\sigma_1 \dots \sigma_i \dots \sigma_\ell)_B \, \rangle \\ & \langle \, (\sigma_1' \dots \sigma_i' \dots \sigma_\ell')_A, (\sigma_1' \dots \sigma_i' \dots \sigma_\ell')_B \, |, \end{aligned} \tag{4.25}$$

where the coefficient matrix C for pure states reads as

$$C^{(\sigma_1 \dots \sigma_\ell)_A, (\sigma_1' \dots \sigma_\ell')_A}_{(\sigma_1 \dots \sigma_\ell)_B, (\sigma_1' \dots \sigma_\ell')_B} = \sum_{\substack{\sigma_i,\sigma_i' \notin \{A,B\} \\ \alpha_1 \dots \alpha_{L-1} \\ \alpha_1' \dots \alpha_{L-1}'}} (T^{\sigma_1}_{\alpha_1} T^{\sigma_1' \dagger}_{\alpha_1'}) \dots (T^{\sigma_i}_{\alpha_{i-1},\alpha_i} T^{\sigma_i' \dagger}_{\alpha_{i-1}',\alpha_i'}) \dots (T^{\sigma_L}_{\alpha_{L-1}} T^{\sigma_L' \dagger}_{\alpha_{L-1}'}), \tag{4.26}$$

and for thermal states reads as

$$C^{(\sigma_1 \dots \sigma_\ell)_A, (\sigma_1' \dots \sigma_\ell')_A}_{(\sigma_1 \dots \sigma_\ell)_B, (\sigma_1' \dots \sigma_\ell')_B} = \sum_{\substack{\sigma_i,\sigma_i' \notin \{A,B\}, \\ \bar{\sigma}_i,\bar{\sigma}_i',\alpha_1 \dots \alpha_{L-1} \\ \alpha_1' \dots \alpha_{L-1}'}} (T^{\sigma_1 \bar{\sigma}_1}_{\alpha_1} T^{\sigma_1' \bar{\sigma}_1' \dagger}_{\alpha_1'}) \dots (T^{\sigma_i \bar{\sigma}_i}_{\alpha_{i-1},\alpha_i} T^{\sigma_i' \bar{\sigma}_i' \dagger}_{\alpha_{i-1}',\alpha_i'}) \dots (T^{\sigma_L \bar{\sigma}_L}_{\alpha_{L-1}} T^{\sigma_L' \bar{\sigma}_L' \dagger}_{\alpha_{L-1}'}). \tag{4.27}$$

the partially transposed $\rho^{T_B}_{A,B}$ is given by

$$\rho_{A,B}^{T_B} = \sum_{\sigma_i,\sigma_i' \in \{A,B\}} C^{(\sigma_1 \ldots \sigma_\ell)_A,(\sigma_1' \ldots \sigma_\ell')_A}_{(\sigma_1' \ldots \sigma_\ell')_B,(\sigma_1 \ldots \sigma_\ell)_B} \mid (\sigma_1 \ldots \sigma_i \ldots \sigma_\ell)_A, (\sigma_1 \ldots \sigma_i \ldots \sigma_\ell)_B \rangle$$
$$\langle \ (\sigma_1' \ldots \sigma_i' \ldots \sigma_\ell')_A, (\sigma_1' \ldots \sigma_i' \ldots \sigma_\ell')_B \mid. \tag{4.28}$$

Note that in Eq. (4.28), the partial transpose operation is performed by acting on block B by exchanging the indices in the coefficient matrix C.

In our calculations we consider a chain of length $L = 200$, which is sufficiently large that boundary or finite size effects can be neglected for both ground state and nonzero temperature. The two blocks have the same size ℓ and are situated in the middle of the chain, i.e., the positions of the left edge of each block are respectively $\frac{L}{2} \pm \frac{d}{2}$, with d the distance between them. For the TEBD calculations we ensure that our results are converged with respect to the bond dimension χ_{max}. In particular, we find that in both the phases ($h/J < 1$ or $h/J > 1$), $\chi_{max} = 32$ is sufficient to get a converged results for block sizes $\ell = 1 \ldots 5$. For larger values of $\ell > 5$ it is difficult to go to higher values of χ_{max} due to larger memory requirement, however, we have checked carefully that the ground states of the calculations are converged with respect to the chosen χ_{max} values for all h/J, see Fig. 4.3. For nonzero temperature, we employ a second order Suzuki-Trotter decomposition with an imaginary time step of $\delta\beta = 0.005/J$, to cool the system from $\beta = 0.0$ down to the considered temperature $\beta = \frac{1}{T}$.

4.6 Results

After having presented our numerical techniques, we will now present our results. In subsection 4.6.1 we discuss the entanglement properties for the ground state, and afterwards in subsection 4.6.2, we consider the case of thermal states.

4.6.1 Logarithmic negativity in ground states

The logarithmic negativity computed in the ground state of the TFIM is depicted in Fig. 4.3 for various values of the transverse field h, from top to bottom, and several subsystem sizes ℓ. Distance $d = 0$ refers to the case of the two blocks located directly next to each other, $d = 1$ to the case where there is one site in between, and so on.

Let us first analyze the ferromagnetic phase described by $h = 0.8$ and $h = 0.9$. For $\ell = 2$, the logarithmic negativity drops to zero at $d^* = 2$. By increasing the size of the blocks, the entanglement threshold d^* increases, which means that the two blocks remain entangled over a longer distance. Up to $\ell = 4$ we can accurately detect d^*, while for $\ell > 4$ the logarithmic negativity reaches the numerical precision in a smooth way before the appearance of a sudden death of the entanglement, making it difficult to unambiguously extract d^*.

Comparing the results of the entanglement threshold at criticality, $h/J = 1$ with $h/J = 0.8$ and $h/J = 0.9$, we observe that for $\ell = 2$ they have the same value $d^* = 2$.

On the other hand, the results start to differ increasing the subsystem size ℓ, as one can see for $\ell = 3$ and $\ell = 4$, where the logarithmic negativity drops to zero at a substantially longer distance compared to the ferromagnetic phase. This reveals how the presence of the long-ranged quantum correlations enhances the entanglement between two separated relatively large blocks. In particular, for $\ell > 4$ one obtains $d^* > 30$, where the entanglement threshold is beyond what we can reach reliably numerically.

For the paramagnetic phase we consider the fields $h/J = 1.5$ and $h/J = 2.0$. On general grounds, we see in Fig. 4.3 that the logarithmic negativity drops to zero earlier compared to the cases $h/J \leq 1$, leading to a smaller entanglement threshold. For example, for $\ell = 2$ the entanglement vanishes after one site separation $d^* = 1$. Moreover, we observe that there is a dependency of d^* on the value of the field h/J. For all the subsystem sizes ℓ considered, the higher the field h/J the smaller the entanglement threshold d^*.

All the three different regimes studied share the same behavior for the entanglement when $\ell = 1$. In the case each block has a single spin, the logarithmic negativity vanishes unless the two sites are at most next-nearest neighbors, i.e. $d^* = 1$. The result obtained at criticality is particularly surprising since one might expect that the long-ranged quantum fluctuations would lead also to long-ranged entanglement. We find that the strong quantum character of the critical point becomes manifest for large block sizes. In order to understand the sharp entanglement threshold for $\ell = 1$ we provide a simple model system in Sec. 4.7.

4.6.2 Logarithmic negativity at nonzero temperature

Switching from zero to finite temperature, thermal excitations start to play an important role. For example, the one-dimensional TFIM has a phase transition only at zero temperature [172]. This means that the correlation length stays finite through all values of the transverse field h.

Fig. 4.4 shows the logarithmic negativity as a function of temperature T/J and the field h/J. We consider a chain of $L = 200$ lattice sites, and each of the two partitions contains $\ell = 4$ spins. From Fig. 4.4 (a) to Fig. 4.4 (d) we increase the distance d between the two partitions from $d = 0$ to $d = 3$. Generally we notice that the higher the temperature, the more entanglement is suppressed. This observation is in agreement with the expectation that thermal fluctuations tend to suppress quantum coherence and consequently entanglement. In the opposite regime of low temperature, the logarithmic negativity shows a peak in the vicinity of the quantum phase transition which also survives at nonzero temperature.

We will now study quantitatively how the logarithmic negativity decays by increasing the distance d between the two partitions at finite temperature. Fig. 4.5 shows $\mathcal{E}_\mathcal{N}$ as a function of the distance d for different values of the inverse temperature βJ at a fixed $h/J = 1.0$. At very large temperature, here $\beta J = 5.0$ in Fig. 4.5 (a), the thermal fluctuations have a strong influence on the entanglement. For the partitions of size $\ell = 1$ the logarithmic negativity drops to zero immediately, i.e., $d^* = 0$

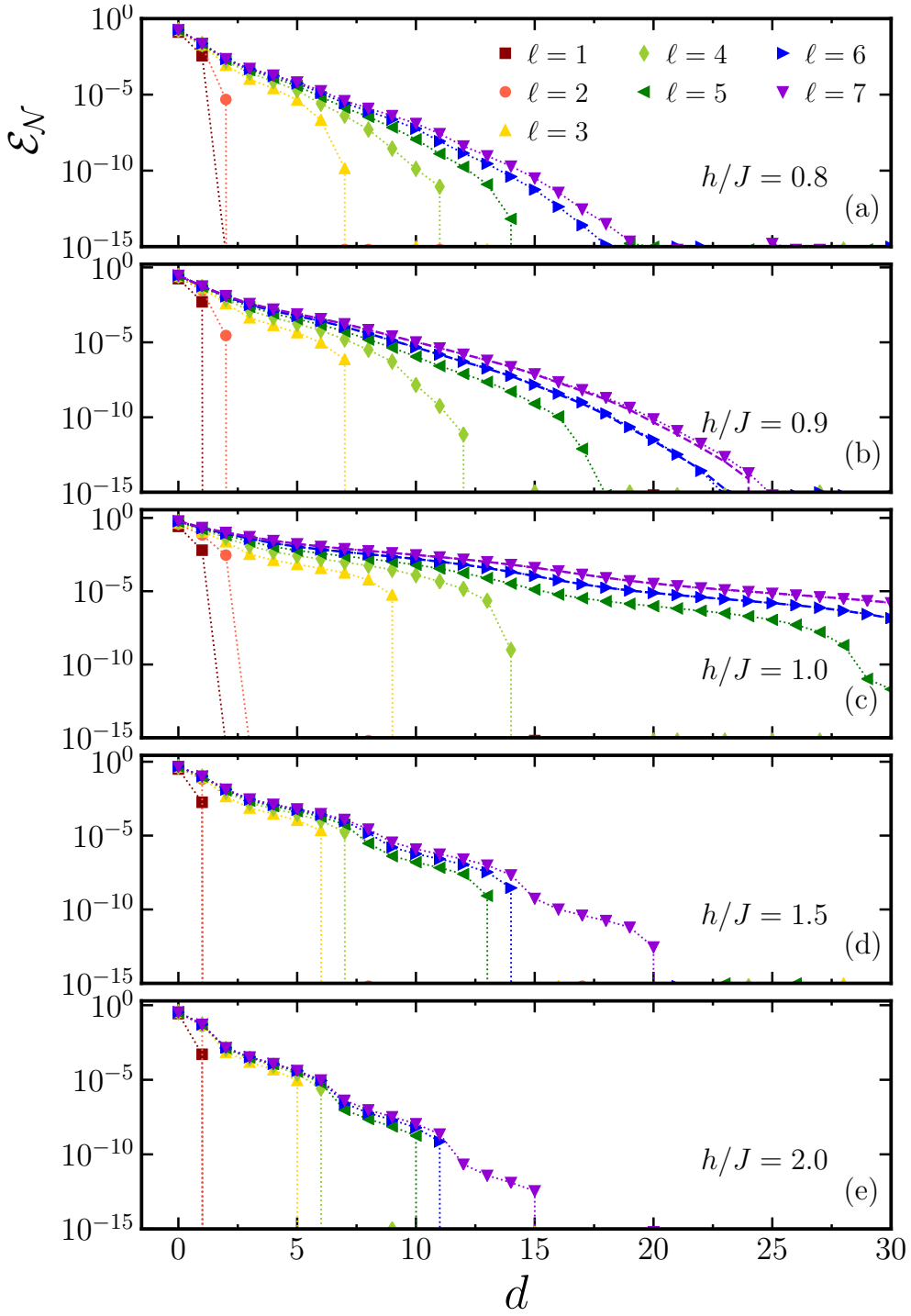

FIGURE 4.3: Logarithmic negativity as a function of distance between two blocks of size ℓ from $\ell = 1$ to $\ell = 7$ in the ground state of the TFIM. In order to avoid finite-size effects, the two partitions are centered at the middle of the chain with $L = 200$ lattice sites with maximum bond dimension $\chi_{max} = 32$. We show $\mathcal{E}_\mathcal{N}$ for different values of the transverse field h/J from $h/J = 0.8$ (a) and $h/J = 0.9$ (b) (ferromagnetic phase) to $h/J = 1.0$ (c) (criticality) to $h/J = 1.5$ (d) and $h/J = 2.0$ (d) (paramagnetic phase). The dashed lines in the (b) and (c) for $\ell = 6, 7$ show $\mathcal{E}_\mathcal{N}$ for $\chi_{max} = 24$.

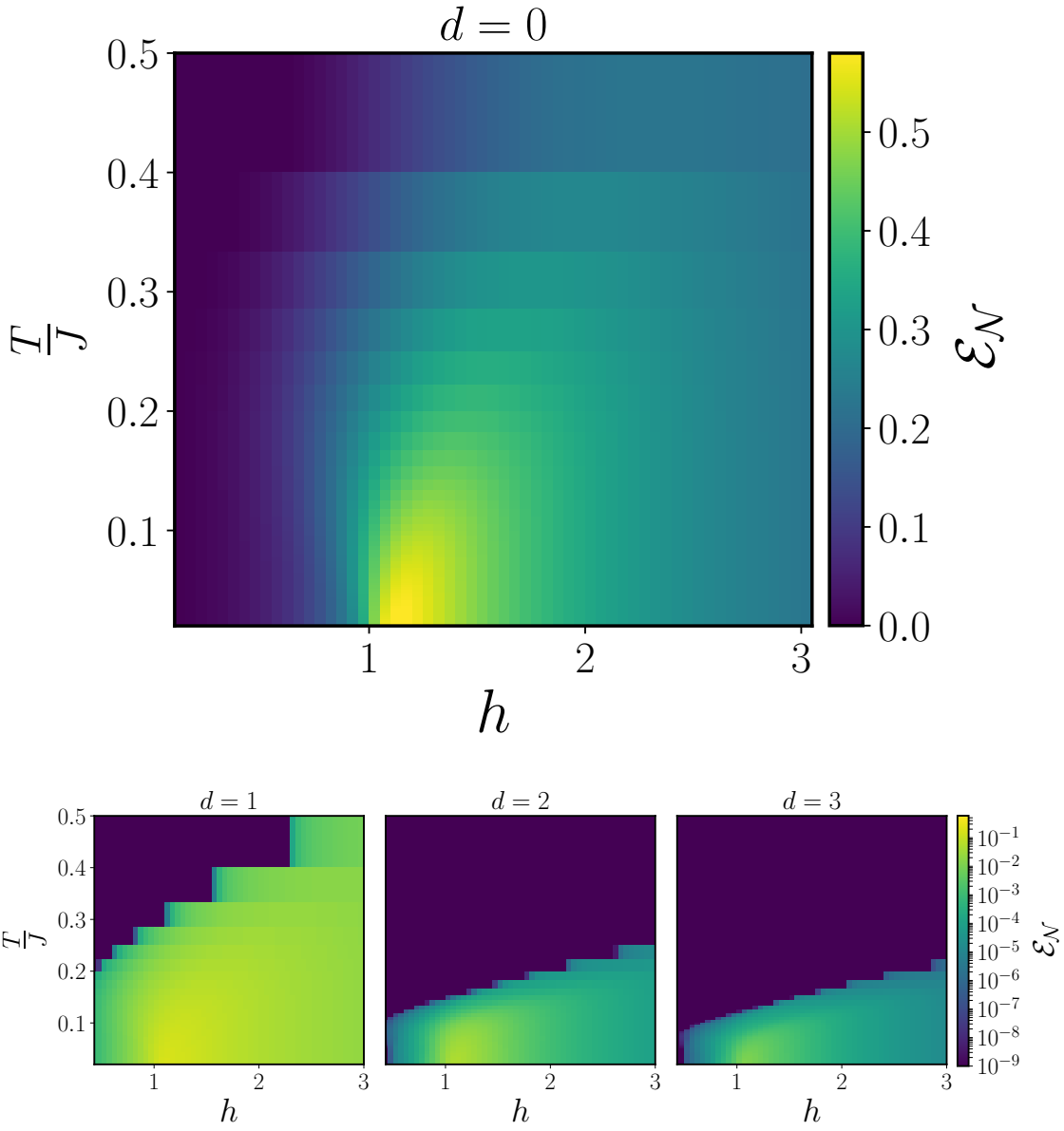

FIGURE 4.4: Color code plot of $\mathcal{E}_{\mathcal{N}}$ between two subsystems A and B with size $\ell = 4$ as a function of temperature and transverse field for a chain of $L = 200$ spins. Each panel is for a different distance d. from $d = 0$ (a) to $d = 3$ (d). Note that for the panels from (b) to (d) $\mathcal{E}_{\mathcal{N}}$ is shown in a log-scale.

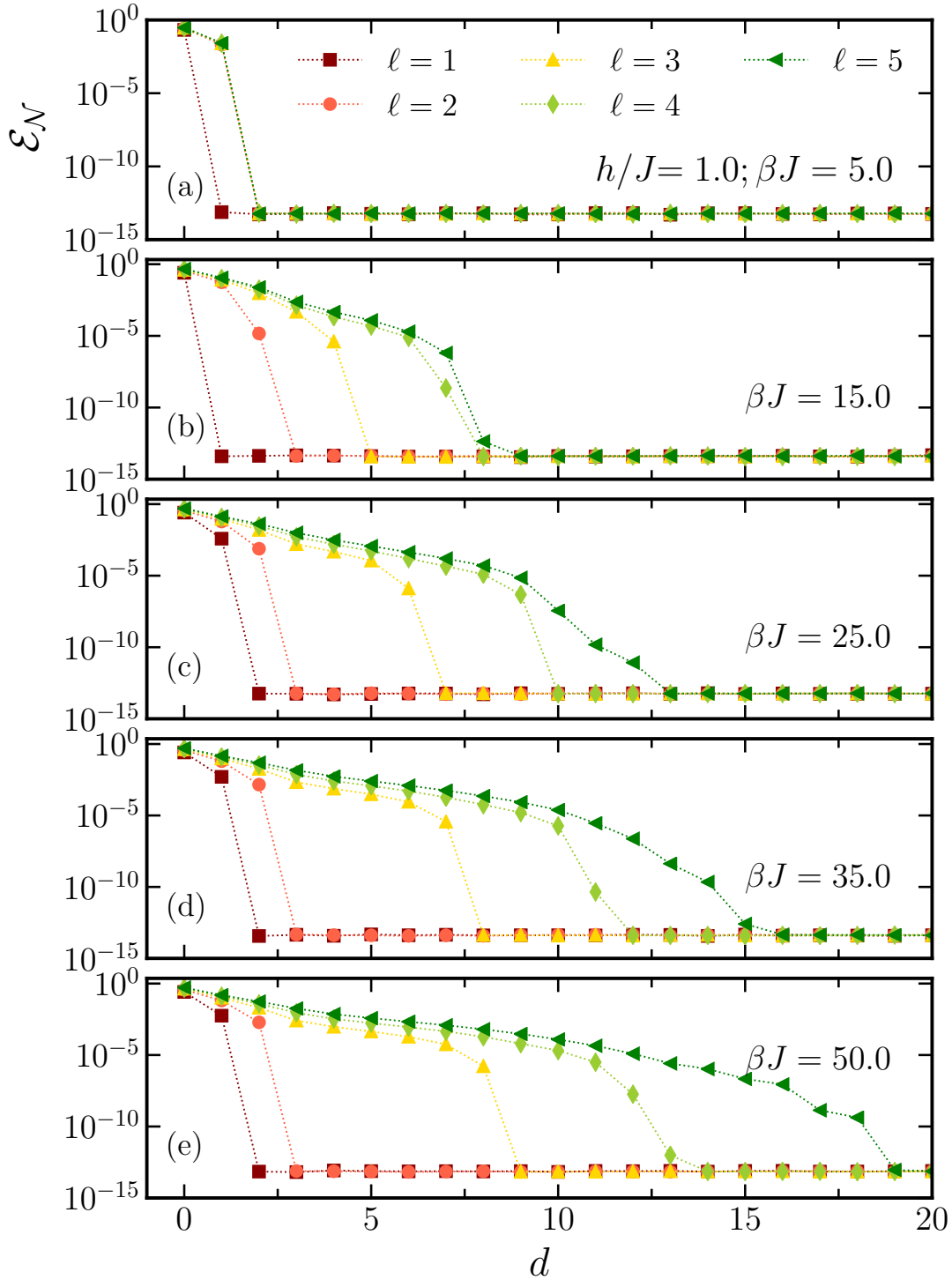

FIGURE 4.5: Logarithmic negativity $\mathcal{E}_{\mathcal{N}}$ as a function of distance d at $h/J = 1.0$ for various temperatures from $\beta J = 5.0$ to $\beta J = 50.0$ for system size of $L = 200$.

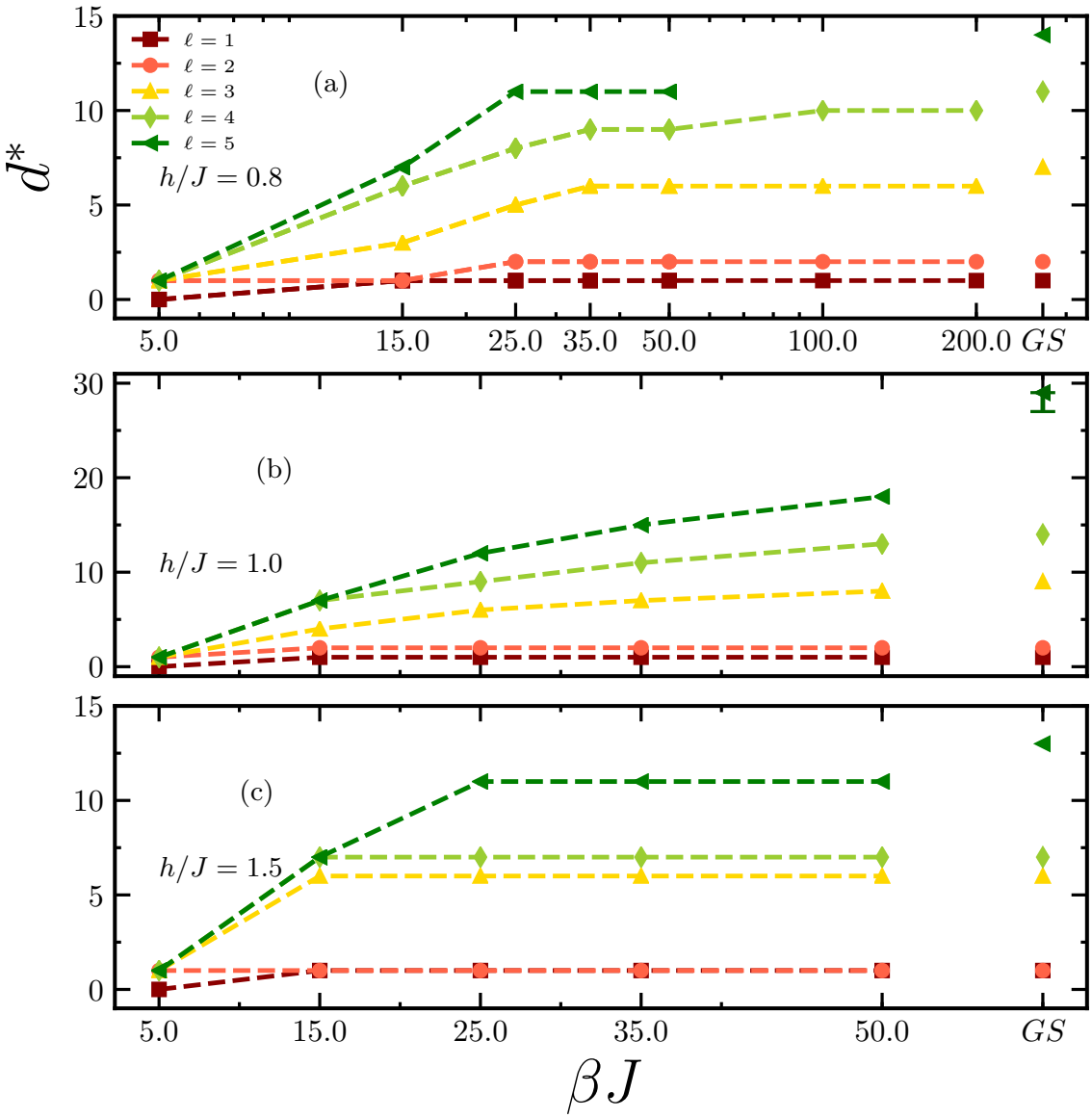

FIGURE 4.6: Entanglement threshold d^* for different subsystem size ℓ for both the ground state and thermal states, for three different transverse field h/J. As temperature reduces, d^* saturates to a constant value. The value of d^* in the ground state (GS) has been shown as an upper bound for the d^* at nonzero temperature.

means two spins are entangled only when they are nearest-neighbors. For $\ell \geq 2$, the logarithmic negativity vanishes after the separation of one lattice site, i.e., $d^* = 1$.

By reducing the temperature to $\beta J = 15$, thermal fluctuations remain sufficiently strong to restrict the entanglement threshold considerably. As shown in Fig. 4.5 (b), for $\ell = 1$, the logarithmic negativity between two blocks vanishes as soon as the distance between them is more than zero site. For $\ell = 2$ and $\ell = 3$ however two blocks remain entangled for a few more sites but of substantially shorter distance compared to the ground state. The thermal fluctuations show their dominant effect better for larger block size. One can see this by looking at the cases $\ell = 4$ and $\ell = 5$. Both drop to zero at approximately the same distance. Reducing the temperature further, the effect of thermal fluctuations becomes smaller as expected. For example in Fig. 4.5 for $\beta J = 25.0$ and $\beta J = 35.0$, the logarithmic negativity for $\ell = 4$ and $\ell = 5$ drops to zero at different threshold distances as a consequence of the less dominant effect of thermal fluctuations. The value of d^* for $l = 3$ has converged for these βJ's but not for $\ell = 4, 5$.

The behavior of the entanglement threshold as function of temperature for different ℓ and transverse field is shown in Fig. 4.6. Away from criticality the entanglement threshold saturates quickly to a constant value for each ℓ, see Fig. 4.6 (a) and (c). With reducing temperature, d^* does not change and reaches to its final value at ground state which is an upper bound for d^* at finite T. Let us point out that the yellow curve in Fig. 4.6 (a) corresponding to $\ell = 3$, seems to reach convergence already at $\beta J = 50.0$. Nevertheless, this value differs by one lattice site from the result obtained for the ground state. This is due to how close we are to the ground state. The thermal activation of the lowest energy excitation is proportional to $e^{-\beta s}$ with s the gap. For $h/J = 1.0$, we have $s = 2\pi/L$ such that $e^{-\beta s} \sim 10^{-1}$ which means we need to be of much lower temperature to suppress thermal excitations.

At criticality, the entanglement threshold d^* increases with decreasing temperature, Fig. 4.6 (b). For small $\ell \leq 2$ the value of d^* converges to its value in the ground state at some temperature. The convergence to the entanglement threshold in the ground state becomes slower for large value of ℓ. In other words d^* increases by increasing ℓ and reducing the temperature, see Fig. 4.6 (b) for $\ell = 3, 4, 5$.

4.7 Entanglement threshold from effective two-level systems

In this section we want to shed some light on the sudden drop of the logarithmic negativity for two spins by providing a simple effective model. Of central importance in this analysis is the possibility of writing, on general grounds, any hermitian operator of a L-spin system in terms of direct products of Pauli operators. In particular, we focus on the density matrix since it plays the main role in computing the

logarithmic negativity:

$$\rho = \sum_{n_1,..,n_L=1}^{4} \rho_{n_1,...,n_L}\, \sigma_{l_1}^{a_{n_1}} \otimes ... \otimes \sigma_{l_L}^{a_{n_L}}, \tag{4.29}$$

where $a_m = 0, x, y, z$, and $\sigma^0 = 1_2$ the 2×2 unit matrix. From Eq. (4.29), the density matrix is fully determined by the values of the correlation functions since $\rho_{n_1,...,n_L} = \mathrm{Tr}[\rho\, \sigma_{l_1}^{a_1} \otimes ... \otimes \sigma_{l_L}^{a_L}]$.

The case we study is a two-spin problem. We consider two spins and label the position of one of them at site 1 and the other at site $1 + d$. This choice permits us to deal with a small number of correlation functions, leading to a simple and intuitive analytical condition for having non vanishing logarithmic negativity. In particular we focus on the paramagnetic phase, where the structure of the reduced density matrix allows us to derive a condition for nonzero logarithmic negativity from an effective two-level system.

4.7.1 Reduced density matrix in the paramagnetic phase

In the paramagnetic phase, the 4×4 reduced density matrix $\rho_{A,B}$ written in the basis $\{|\downarrow,\downarrow\rangle, |\downarrow,\uparrow\rangle, |\uparrow,\downarrow\rangle, |\uparrow,\uparrow\rangle\}$, is characterized by having nonzero entries only on the diagonal and the anti-diagonal:

$$\rho_{A,B} = \begin{pmatrix} \rho_{A,B}(1,1) & 0 & 0 & \rho_{A,B}(1,4) \\ 0 & \rho_{A,B}(2,2) & \rho_{A,B}(2,3) & 0 \\ 0 & \rho_{A,B}(3,2) & \rho_{A,B}(3,3) & 0 \\ \rho_{A,B}(4,1) & 0 & 0 & \rho_{A,B}(4,4) \end{pmatrix}. \tag{4.30}$$

The reason for the vanishing of the other matrix elements is symmetries of the Hamiltonian, as one can directly see from writing those entries in terms of the respective two-point correlation functions. For example, let us consider $\rho_{A,B}(1,2) = \rho_{0,x} - \rho_{z,x} + i(\rho_{0,y} - \rho_{z,y})$, in which $\rho_{a_1,a_{1+d}} = \langle \sigma_1^{a_1} \sigma_{1+d}^{a_{1+d}} \rangle$. Since we are evaluating the correlation functions in the ground state and the system is symmetric under time reversal, it follows that $\rho_{0,y} = \rho_{z,y} = 0$. Moreover, in the paramagnetic phase where the ground state does not break the $\mathbb{Z}_2$ symmetry, we also have $\rho_{0,x} = \rho_{z,x} = 0$. Taking into account all these considerations we conclude that $\rho_{A,B}(1,2) = 0$ and similar argumentations hold for the other matrix elements $\rho_{A,B}(1,3)$, $\rho_{A,B}(2,4)$ and $\rho_{A,B}(3,4)$.

The partial transpose of the density matrix is therefore determined by two uncoupled effective two-level systems:

$$\rho_{A,B}^T = \begin{pmatrix} \rho_{A,B}(1,1) & \rho_{A,B}(2,3) & 0 & 0 \\ \rho_{A,B}(3,2) & \rho_{A,B}(4,4) & 0 & 0 \\ 0 & 0 & \rho_{A,B}(2,2) & \rho_{A,B}(1,4) \\ 0 & 0 & \rho_{A,B}(4,1) & \rho_{A,B}(3,3) \end{pmatrix}. \tag{4.31}$$

For the sake of simplicity, let us focus only on one two-level system, since both of them have the same features:

$$\rho_1^{TLS} = \begin{pmatrix} \rho_{A,B}(1,1) & \rho_{A,B}(2,3) \\ \rho_{A,B}(3,2) & \rho_{A,B}(4,4) \end{pmatrix}. \tag{4.32}$$

Let us denote with $\delta = \rho_{A,B}(2,3)$ the coupling between the two levels, with $E_\pm^*$ the eigenvalues of the matrix (4.32) and with $E_- = \rho_{A,B}(1,1)$, $E_+ = \rho_{A,B}(4,4)$ the unperturbed ones. For an illustration see Fig. 4.7.

The picture of the two-level system in Eq. (4.31) gives a simple physical explanation for the spatial behavior of the logarithmic negativity. Although the reduced density matrix $\rho_{A,B}$ always has positive eigenvalues since it is a semi-positively defined operator, the partially transposed matrix $\rho_{A,B}^T$ can have negative ones, when at least one of the two two-level systems has negative eigenvalues. This can lead to a nonvanishing logarithmic negativity.

Condition for non-vanishing logarithmic negativity

With increasing δ the splitting between E_+ and E_- increases, which for sufficiently large δ turns one of the eigenvalues negative. In order to obtain a more quantitative description of the behavior of the logarithmic negativity, we solve the eigenvalue problem of the matrix (4.32), and similarly for the other two-level system, searching for the conditions which lead to a negative eigenvalue and therefore to a nonvanishing logarithmic negativity. As a result we obtain the following inequalities:

$$\rho_{A,B}^2(2,3) > \rho_{A,B}(1,1)\rho_{A,B}(4,4), \tag{4.33}$$

$$\rho_{A,B}^2(1,4) > \rho_{A,B}(2,2)\rho_{A,B}(3,3). \tag{4.34}$$

Eqs. (4.33) and (4.34) give a quantitative statement concerning how strong the couplings $\rho_{A,B}(2,3)$, $\rho_{A,B}(1,4)$ must be to lower the eigenvalue below zero.

To achieve a better physical intuition for the behavior of the logarithmic negativity as a function of distance, we express the conditions (4.33) and (4.34) in terms of the two-point correlation functions using the prescription in Eq. (4.29). These functions, in some particular limiting cases, are described by universal behaviors allowing a simple analysis of the conditions (4.33) and (4.34) and consequently it is possible to have a clear idea on the spatial structure of the logarithmic negativity for two spins. For simplicity we consider only Eq. (4.33), but similar observations hold for Eq. (4.34). Since

$$\rho_{A,B}(2,3) = \rho_{x,x} + \rho_{y,y} \tag{4.35}$$

$$\rho_{A,B}(1,1) = 1 + \rho_{z,z} - \rho_{0,z} - \rho_{z,0} \tag{4.36}$$

$$\rho_{A,B}(4,4) = 1 + \rho_{z,z} + \rho_{0,z} + \rho_{z,0}, \tag{4.37}$$

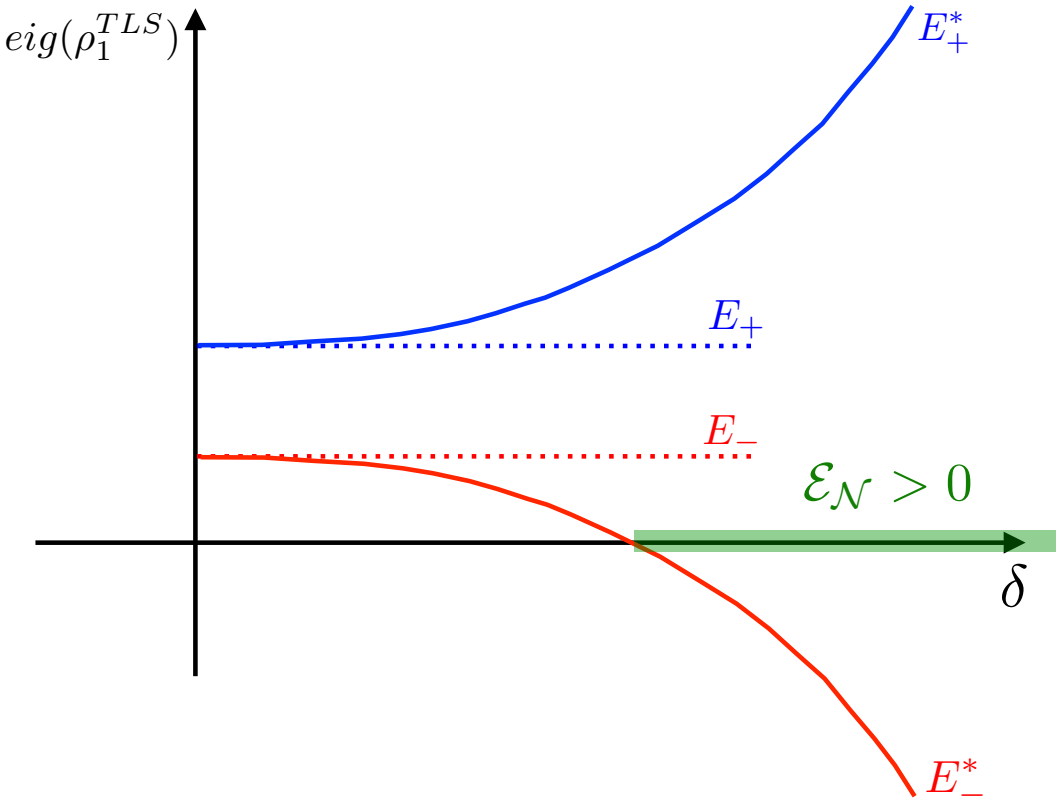

FIGURE 4.7: Eigenvalues $E_\pm^*$ of the partially transposed reduced density matrix ρ_1^{TLS} in Eq. (4.32), as a function of δ . While the full lines correspond to $E_\pm^*$, the dotted ones correspond to the unperturbed eigenvalues $E_\pm$. When δ is sufficiently large such that the eigenvalue E_-^* becomes negative, the logarithmic negativity starts to take a nonzero value.

Eq. (4.33) reads

$$(1-\rho_{z,z})^2-(\rho_{z,0}-\rho_{0,z})^2 < (\rho_{x,x}-\rho_{y,y})^2+(\rho_{x,y}+\rho_{y,x})^2. \tag{4.38}$$

Eq. (4.38) can be further simplified noting that the translational invariance of the system implies $\rho_{0,z}=\rho_{z,0}$. Moreover, the terms $\rho_{x,y}$ and $\rho_{y,x}$ vanish because the entries of the reduced density matrix $\rho_{A,B}$ have to be real due to time-reversal symmetry. Using all this information, Eq. (4.38) simplifies to

$$(1-\rho_{z,z})^2 < (\rho_{x,x}-\rho_{y,y})^2. \tag{4.39}$$

In other words, using the definition of the coefficients: $\rho_{x,x}=\langle\sigma_1^x\sigma_{d+1}^x\rangle$, $\rho_{y,y}=\langle\sigma_1^y\sigma_{d+1}^y\rangle$ and $\rho_{z,z}=\langle\sigma_1^z\sigma_{d+1}^z\rangle$, we can rewrite Eq. (4.39) as following

$$(1-\langle\sigma_1^z\sigma_{d+1}^z\rangle)^2 < (\langle\sigma_1^x\sigma_{d+1}^x\rangle-\langle\sigma_1^y\sigma_{d+1}^y\rangle)^2. \tag{4.40}$$

Vanishing logarithmic negativity at large distance

From Eq. (4.39) one can directly see the vanishing logarithmic negativity when the two spins are very far apart. In this regime, the correlation functions follow a generic behavior:

$$\rho_{x,x}=\langle\sigma_1^x\sigma_{d+1}^x\rangle\sim e^{-d/\xi_x}\underset{d\to\infty}{\longrightarrow}0. \tag{4.41}$$

$$\rho_{y,y}=\langle\sigma_1^y\sigma_{d+1}^y\rangle\sim e^{-d/\xi_y}\underset{d\to\infty}{\longrightarrow}0. \tag{4.42}$$

$$\rho_{z,z}=\langle\sigma_1^z\sigma_{d+1}^z\rangle\sim\langle\sigma_1^z\rangle\langle\sigma_{d+1}^z\rangle\neq 0. \tag{4.43}$$

Thus, in the limit $d\to\infty$, both $\rho_{x,x}$ and $\rho_{y,y}$ go to zero and therefore the inequality (4.39) cannot be satisfied leading to a vanishing logarithmic negativity. In addition, the two-level system description is able to predict that the logarithmic negativity is zero not only in the singular point $d=\infty$, but in an interval of nonzero extent $d<\infty$. For a general field h in the paramagnetic phase, $h>h_c$, both the magnetization and correlation along z are finite but smaller than one. Consequently, the diagonal elements in the matrix (4.32) are strictly larger than zero, as one can realize from Eqs. (4.36) and (4.37). In order to argue the existence of a finite interval of distances where the logarithmic negativity vanishes, let us first begin from the case where the two spins are infinitely far apart from each other, meaning that the matrix (4.32) is diagonal because of the exponential suppression of the off-diagonal elements announced by Eqs. (4.41), (4.42) and (4.35). As the distance d decreases, the off-diagonal element $\rho_A(2,3)=\delta$ starts to have a nonzero value, affecting perturbatively the eigenvalue of the matrix (4.32). In particular, using perturbation theory in δ, the shift of the eigenvalues is proportional to the square of the coupling of the

two level system δ

$$E_{\pm}^{*} = E_{\pm} \pm \frac{\delta^2}{E_{+} - E_{-}}, \tag{4.44}$$

supposing that $E_{\pm}$ are nondegenerate. Let us point out that the unperturbed eigenvalues $E_{\pm}$, appearing in Eq. (4.44), cannot assume negative values since they correspond to the diagonal elements of $\rho_{A,B}$ which are probabilities. As a consequence, δ must be sufficiently large to make at least one eigenvalue negative. This can occur only when the distance between the two spins is less than a certain threshold, $d < \tilde{d}$, since the strength of δ is exponentially suppressed with d as suggested by Eqs. (4.41), (4.42) and (4.35).

While the condition for nonzero logarithmic negativity in Eq. (4.39) holds also for small distances d, the exponential structures of the correlation functions in Eqs. (4.41), (4.42) are no longer valid since they describe the asymptotic behavior in the limit $d \to \infty$. Nevertheless, the strength of δ decreases with d, as we observe from the nonzero entanglement between the two spins in the paramagnetic phase at short distance, see Fig. 4.3 panels (d) and (e). Moreover, nonzero entanglement between two spins at short distances was already shown in a variety of works [131, 128, 129, 130, 132].

4.7.2 Reduced density matrix at the critical point

The two-level system description introduced in the previous section holds also at criticality, since only in the symmetry-broken phase the matrix elements $\rho_{0,x}$, $\rho_{z,x}$, $\rho_{0,y}$, $\rho_{z,y}$ are nonzero.

The main difference to the paramagnetic phase consists in the functional form of the order parameter correlation function (4.41). Specifically, it exhibits a power law decay instead of an exponential one: $\rho_{x,x} \sim d^{-\eta}$, with η the critical exponent of the correlation function whose value depends on the universality class of the problem. For the 1D-Ising transverse field, $\eta = 1/4$. Although we mentioned differences between the two regimes, the same conclusion concerning the spatial structure of the two-spins holds.

4.8 Discussion

In this chapter we have studied the spatial entanglement structure of the transverse-field Ising chain at zero and nonzero temperatures. Specifically, we have investigated the logarithmic negativity between two disjoint blocks of equal size ℓ as a function of their separation, which is an entanglement analog to a quantum correlation function.

We have found that for any fixed size ℓ of the blocks there exists an entanglement threshold at a distance d^* beyond which the logarithmic negativity vanishes identically. This holds across the whole phase diagram of the system including also the quantum critical point where the system exhibits long-ranged quantum correlations.

The influence of temperature onto the spatial entanglement structure as measured by the logarithmic negativity depends crucially on the size ℓ of the blocks. The larger d^* (for increasing ℓ) the more important the influence of temperature, cutting off long-range entanglement.

For small blocks ℓ the entanglement threshold d^* appears on short distances on the order of a few lattice spacings even at the quantum critical point. In this case the precise value of d^* is determined by nonuniversal short-distance properties that depend on the microscopic details of the model. However, using a simple effective model we have found for the case $\ell = 1$ that the existence of the threshold d^* can be derived solely from the universal long-distance properties.

A vanishing logarithmic negativity for blocks of size $\ell = 1$ implies that the two corresponding qubits are unentangled, because the PPT criterion (whose violation is measured by the negativity) for the separability of a quantum state is not only necessary but also sufficient. For larger blocks $\ell > 1$ the PPT criterion is not sufficient anymore, such that a vanishing logarithmic negativity at distances larger than d^* does not necessarily imply that the two blocks are completely unentangled. Thus, we cannot exclude that there exist other measures signaling nonzero entanglement. However, it is important to note that the logarithmic negativity gives a bound on the distillable entanglement, such that a vanishing logarithmic negativity implies that no Bell pairs can be extracted from the state.

At first sight the already known result of a finite entanglement threshold $d^* < \infty$ for $\ell = 1$ at the critical point might not comply with expectations originating from strong quantum correlations or the well-established violation of the area law for the entanglement entropy. The results of our work provide a quantitative description of the crossover from $\ell = 1$ to $\ell \gg 1$ upon increasing ℓ.

We have studied the spatial entanglement structure for the transverse-field Ising chain so that it is a natural question to which extent our results extend to a broader class of systems. The effective model for the reduced density matrix at $\ell = 1$, which we used to argue about the existence of an entanglement threshold, can be straightforwardly applied to other models as well, independent of the dimension provided the blocks consist of spin-1/2 degrees of freedom and the system resides in a paramagnetic phase. Our conclusions also hold for the critical point whenever the quantum correlations are long-ranged along one particular direction. This might change, for example, in the case the transition is associated with a broken $U(1)$ instead of $\mathbb{Z}_2$ symmetry. For larger block sizes $\ell > 1$ the situation is much less clear on general grounds and deserves a further investigation.

Chapter 5

Eigenstate spin-glass order parameter

> Very few believed [localization] at the time, and even fewer saw its importance; among those who failed to fully understand it at first was certainly its author. It has yet to receive adequate mathematical treatment, and one has to resort to the indignity of numerical simulations to settle even the simplest questions about it.
> —Philip W. Anderson, Nobel lecture, 8 December 1977

Recently, it has been proposed that phases of quantum many-body systems may not only be characterized in terms of their thermodynamic properties but also on the level of single eigenstates [173, 174, 175, 176, 177, 178, 26, 179]. These so-called eigenstate phases are protected by nonergodicity where the long-time dynamical properties of the system cannot be captured by a thermodynamic ensemble. Consequently, systems can exhibit order in steady states resulting from real-time dynamics although the thermal states at the corresponding energy density are featureless. The protecting nonergodicity can be generated by strong quenched disorder [180, 11, 181, 24, 182, 176, 183, 184, 185, 186, 26, 187, 188] or dynamical constraints due to gauge invariance [189, 190, 191]. Recently, the dynamical signatures of such eigenstate phases have been probed in experiments including the observation of many-body localization (MBL) [192, 193, 194, 195, 196, 197] or discrete time crystals [198, 199].

MBL phases may not only be characterized by their ergodicity breaking, but can also host ordered phases such as the MBL spin-glass [173, 174, 179], see Fig. 5.1. The MBL spin-glass is challenging to access in a dynamical measurement and therefore experimentally since the conventionally used Edwards-Anderson order parameter is a two-point correlation function in time. In this chapter, we show that MBL spin-glass order can also be detected from two-site reduced density matrices, which we use to construct an eigenstate spin-glass (ESG) order parameter.

5.1 MBL Spin-glass phase

As we mentioned before, we aim to show that MBL-SG order can be detected from two-site reduced density matrices, which we use to construct an eigenstate spin-glass (ESG) order parameter. The information about reduced density matrices and

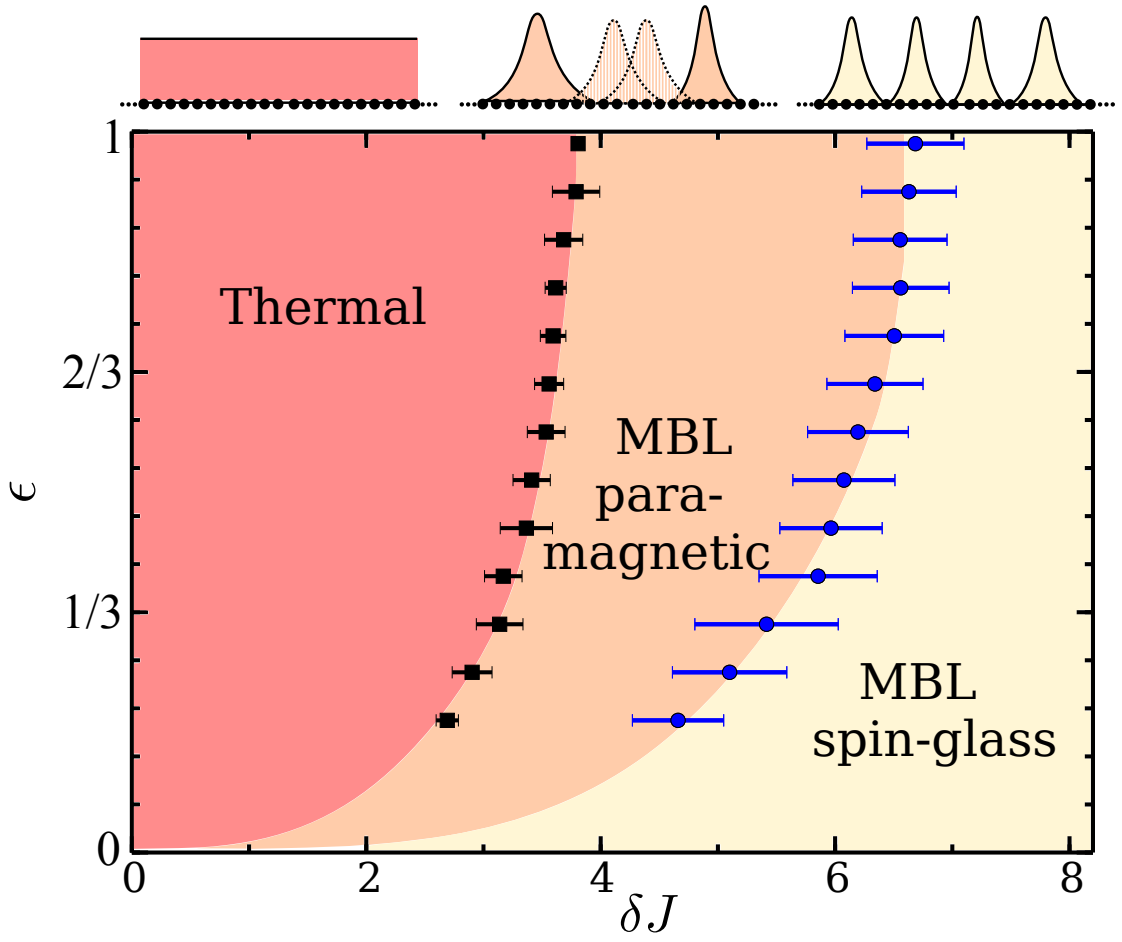

FIGURE 5.1: Phase diagram of the Ising model. ϵ is the energy density relative to total bandwidth. The axes give the energy density above the ground state and the disorder strength. The colored areas are guides to the eye. The data are obtained from finite size scaling of entanglement difference, $\Delta S_n = \lim_{t\to\infty} S_n(t) - S_n(0)$, after a local quench and the spin-glass order parameter, Eq. 5.1; The thermal phase is characterized by extended domain walls, the MBL paramagnetic phase by localized domain walls which are created and removed in pairs (dashed), and the MBL spin glass by localized nonoverlapping domain walls. Note that this figure is the result from the reference [174].

its properties has been described in section 4.2.1. We find that this ESG order parameter captures MBL-SG phases both in eigenstates as well as in the nonequilibrium dynamics from a *local in time* measurement, which makes MBL-SG order accessible within current experiments in quantum simulators. In previous works MBL spin glass order in an eigenstate $|\Psi\rangle$ has been detected for spin-1/2 systems using an Edwards-Anderson (EA) order parameter [200, 173]

$$\chi_{\mathrm{EA}} = \frac{1}{L^2} \sum_{i,j=1}^{L} \langle \Psi | \sigma_i^z \sigma_j^z | \Psi \rangle^2 \,, \tag{5.1}$$

where σ_i^z, $i = 1, \ldots, L$, denotes Pauli matrices on site i with L the total number of lattice sites. This order parameter requires access to single quantum many-body eigenstates, which experimentally is not achievable and also limits numerical studies to exact diagonalization and therefore the reachable system sizes. While χ_{EA} can also be rewritten in the time domain, a measurement of χ_{EA} then requires access to a two-time correlation function at large times, which is experimentally challenging and not possible within current quantum simulator implementations.

5.2 Eigenstate spin-glass order parameter

For the definition of the eigenstate spin-glass order parameter χ_{ESG}, let us first fix two lattice sites i and j. Moreover, let us denote the reduced density matrix of these two sites by ρ_{ij}, which can be obtained from the full density matrix ρ by tracing out the complement of the two sites i and j. The main idea behind χ_{ESG} is to not calculate the square of the spin-spin correlator in Eq. (5.1) for the full quantum many-body eigenstate, but rather on the local equivalent which are the eigenstates of the reduced density matrix ρ_{ij}. Accordingly, we diagonalize the 4×4 matrix $\rho_{ij} = \sum_n p_n^{ij} |\psi_n^{ij}\rangle\langle\psi_n^{ij}|$ to find its eigenvalues (p_n^{ij}), eigenvectors ($|\psi_n^{ij}\rangle$) and calculate the following quantity:

$$\chi_{\mathrm{ESG}}^{ij} = \sum_{n=1}^{4} p_n^{ij} \langle \psi_n^{ij} | \sigma_i^z \sigma_j^z | \psi_n^{ij} \rangle^2 \,. \tag{5.2}$$

Finally, we perform a spatial average over all pairs (i, j) via:

$$\chi_{\mathrm{ESG}} = \frac{1}{L(L-1)} \sum_{i \neq j}^{L} \chi_{\mathrm{ESG}}^{ij} \,. \tag{5.3}$$

It is the central result of this work that for a paradigmatic MBL spin-glass model the χ_{ESG} detects the eigenstate spin-glass order as we show in detail below. Thus, MBL spin-glass order doesn't require knowledge of the full quantum many-body eigenstate, but rather only the local information contained in the reduced density matrix. We compare χ_{ESG} and χ_{EA} both in the GS for large systems using DMRG and in

highly-excited states using exact diagonalization. We find numerical evidence that both of these quantities are not only quantitatively close but also can be used as order parameters for the MBL spin glass transition in the studied model. Importantly, we also show that $\mathcal{X}_{\mathrm{ESG}}$ can be used as a dynamical measure to detect the MBL spin-glass order. In particular, we find that for typical initial conditions, the long-time limit of $\mathcal{X}_{\mathrm{ESG}}$ is nonzero in the ordered phase and vanishes in the paramagnetic one. However, towards the transition the dynamics becomes very slow such that accessing the structure of the transition remains challenging. In the end we will discuss how to observe our findings in current experiments.

5.3 Model and method

We study the ESG order parameter $\mathcal{X}_{\mathrm{ESG}}$ for the following quantum Ising chain with open boundary conditions,

$$\hat{\mathcal{H}} = -\frac{1}{2}\left[\sum_{i=1}^{L-1} J_i^z \sigma_i^z \sigma_{i+1}^z + \sum_{i=1}^{L-1} J_i^x \sigma_i^x \sigma_{i+1}^x + \sum_{i=1}^{L} h_i^x \sigma_i^x\right], \tag{5.4}$$

where $\sigma_i^{x,z}$, $i = 1, \ldots, L$ are the Pauli matrices and L denotes the total number of lattice sites. All the parameters appearing in this model are random and taken from uniform distributions. We choose $J_i^z \in [-J, J]$ and $h_i^x \in [-h, h]$ from uniform box distribution. For vanishing J_i^x the model reduces to the transverse field Ising chain, which is integrable and exactly solvable by a mapping to a quadratic fermionic theory using a Jordan-Wigner transformation [201]. To make the model generic and non-integrable we add a weak random $J_i^x \in [-\frac{h}{4}, \frac{h}{4}]$ term, which becomes equivalent to a two-particle interaction in the fermionic language and renders the model non-integrable.

The transverse-field Ising chain with $J_i^x = 0$ exhibits a $T = 0$ quantum phase transition from a paramagnetic $(J < h)$ state to a doubly degenerate spin-glass ground state $(J > h)$ [2]. In order to explore the ground state physics for the interacting model at $J_i^x \neq 0$, we use density-matrix renormalization group (DMRG) techniques within a matrix product state formulation [202] and used second order Suzuki-Trotter decomposition to exponentiate the unitary operator [203]. This allows us to probe the phase transition for large system sizes reducing finite-size effects. In order to access the high energy eigenstates we use standard exact diagonalization and typically calculate 16 eigenstates from the middle of the spectrum and perform an average of $\mathcal{X}_{\mathrm{ESG}}$ over this set of states. At excited energies around ~ 1000 disorder configurations are used to perform statistical averaging of $\mathcal{X}_{\mathrm{EA}}$ and $\mathcal{X}_{\mathrm{ESG}}$, while in ground state ~ 100 disorder realizations are considered for averaging. Finally, for simulating the dynamics for large system sizes the time-evolving block decimation technique is used. To minimize finite-size effects, we calculate $\mathcal{X}_{\mathrm{EA}}$ and $\mathcal{X}_{\mathrm{ESG}}$ by averaging not over all pairs (i, j) of lattice sites but rather restrict

to those pairs with $|i-j| > 4$. Also to minimize the edge effects for such small system sizes we excluded the edge site contribution in χ_{EA} and χ_{ESG}.

5.4 Eigenstate results

First we study the χ_{ESG} in eigenstates and compare it to the Edwards-Anderson order parameter χ_{EA} . In Fig. 5.2(a-d) we plot both χ_{EA} and χ_{ESG} for the ground state calculated using the density-matrix renormalization group for system sizes $L = 32, 48, 64$ and exact diagonalization for $L = 8, 12, 16$ as a function of the spin-spin coupling strength strength J/h. The top panel shows the ground state results. As expected, for weak couplings ($J/h < 1.5$) the system is in a paramagnetic phase and thus χ_{EA} vanishes. The χ_{ESG} is showing an analogous behavior, as can be seen in Fig. 5.2(b). In the spin-glass phase χ_{EA} is finite and almost independent of systems size, as we find also for χ_{ESG}, see Fig. 5.2(b). Overall, these results suggest that the χ_{ESG} parameter can be taken as an order parameter for the spin-glass quantum phase transition in the considered model.

In Fig. 5.2(c-d) we study spin-glass order in excited states of the same model Eq. (5.4) where we observe an overall similar behavior. For sufficiently weak couplings both χ_{EA} and χ_{ESG} take small values indicating that the system does not exhibit MBL-SG order. This is different for large couplings where both χ_{EA} and χ_{ESG} saturate to a large nonzero value almost independent of system size. More quantitatively, we analyze the finite size dependence for strong and weak couplings by plotting both the eigenstate order parameters as a function of $1/L$ for several disorder values ($J/h = 0.6, 0.8, 1.0, 2.5$) in Fig. 5.2(e-f). While for large couplings both χ_{EA} and χ_{ESG} are almost independent of system size, at weak couplings a linear extrapolation in $1/L$ suggests vanishing values. This extrapolation should be taken only as a guide to the eye as the precise functional form of the L-dependence is not known. Due to the limited system sizes and the resulting strong finite-size effects we don't attempt to extract the MBL-SG transition from the exact diagonalization data. We find, however, that the measurement of χ_{ESG} in the real-time dynamics, as discussed in the following, is much better suited for that purpose.

5.4.1 Quench dynamics

It is a crucial observation that χ_{ESG} can be computed for any state. In particular, we now show that this makes it possible to monitor the buildup of MBL-SG order in the quantum real-time dynamics from a local in time measurement. This observation is not only useful from a theoretical point of view, but also makes the observation of MBL-SG phases accessible for current experiments in quantum simulators.

In the following we study the real-time evolution of the ESG order parameter $\chi_{\mathrm{ESG}}(t)$ from initial spin configurations with random orientations along the σ^x direction therefore respecting the $\mathbb{Z}_2$ symmetry of the Hamiltonian. We compute the dynamics using time dependent DMRG (tDMRG) or TEBD using the second order Trotter decomposition with $dt = 0.01$, where we kept only those states with singular

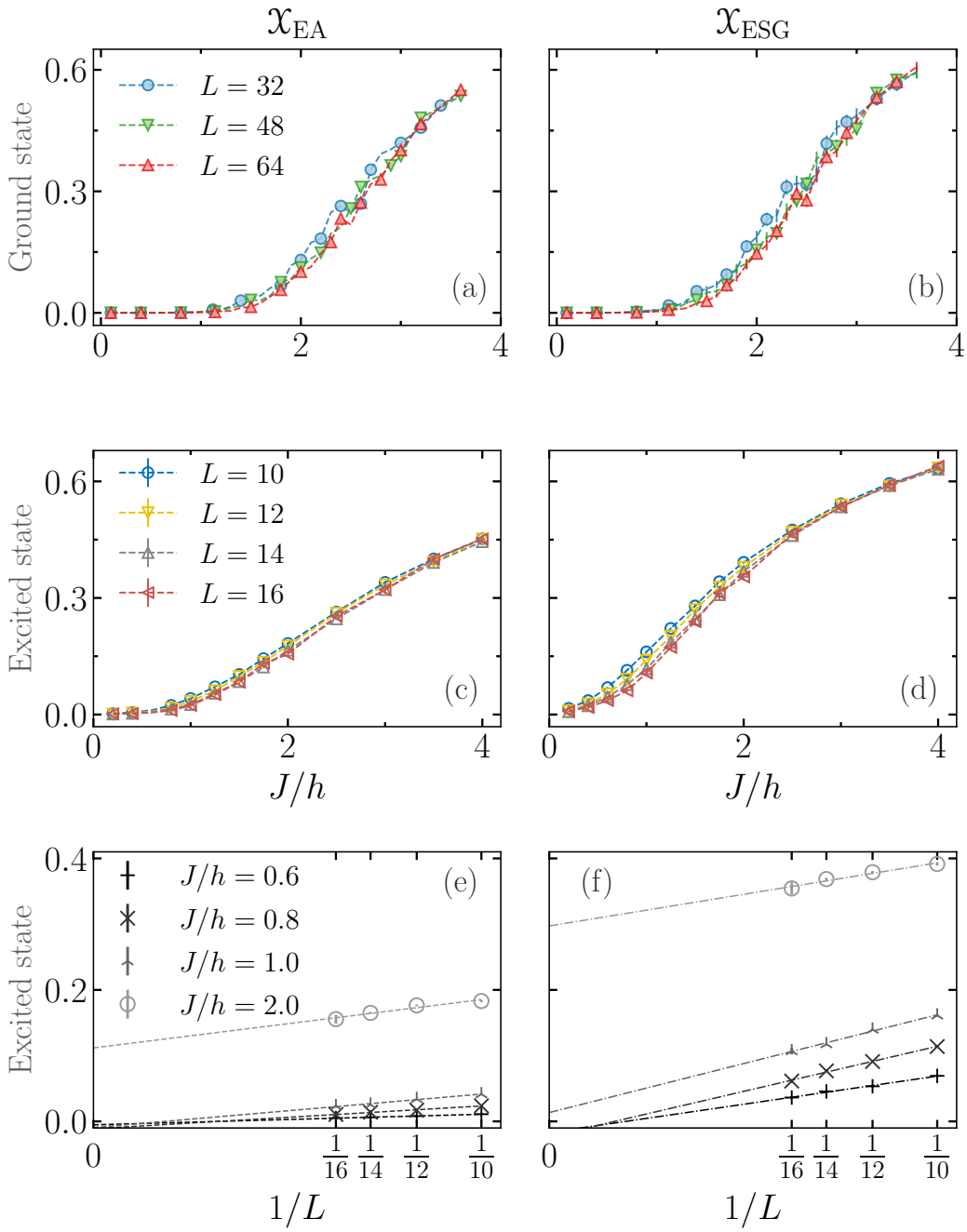

FIGURE 5.2: **Eigenstate spin-glass order.** Upper panel: (a) Shows the Edwards-Anderson order parameter, χ_{EA}, in the ground state of the Hamiltonian Eq. (5.4) obtained using DMRG for system sizes $L = 32, 48, 64$ as a function of coupling strength J/h. While for weak couplings χ_{EA} approaches zero, for large $J/h \gtrsim 1.5$ χ_{EA} becomes nonvanishing in the expected spin-glass ordered phase. (b) The eigenstate spin-glass order parameter χ_{ESG} in the ground state for the same system sizes. (c) χ_{EA} in excited states from the center of the spectrum for system sizes $L = 10, 12, 14, 16$ obtained 4from exact diagonalization, and compared to χ_{ESG} (d). In (e-f) we show the finite-size dependence of χ_{ESG} for excited states. For couplings $J/h \lesssim 1$, χ_{ESG} tends towards a vanishing value for increasing system sizes, whereas for $J/h \gtrsim 1$ it is large and nonzero. The included lines are a guide to the eye and don't represent a quantitative extrapolation.

values above 10^{-9}. An analysis of the numerical accuracy and time steps in TEBD calculations can be found in the appendix C.

Initial state along σ^x

In Fig. 5.3 we show the dynamical evolution of χ_{ESG}, where we compare two representatives for the temporal behavior for weak couplings in Fig. 5.3a and for strong couplings in Fig. 5.3b, respectively. At $t = 0$ we have that $\chi_{\mathrm{ESG}}(t = 0) = 0$ since the initial condition is structureless and does not contain any spatial correlations. In the transient stage of the dynamics we observe an increase of $\chi_{\mathrm{ESG}}(t)$ to nonzero values as a consequence of an initial buildup of spatial correlations. On longer time scales two qualitatively different dynamical regimes emerge depending on the coupling strength, suggesting that MBL-SG order can be detected from the long-time limit of $\chi_{\mathrm{ESG}}(t)$. While for weak couplings $\chi_{\mathrm{ESG}}(t)$ decays for increasing time, this is not the case for strong couplings, where $\chi_{\mathrm{ESG}}(t)$ saturates to a nonzero value.

Initial state with broken Z_2 symmetry

In this section we show additional data for quench dynamics when the initial state breaks the Ising $\mathbb{Z}_2$ symmetry by choosing product states aligned along the z-direction. As seen in Fig. 5.4 we observe the same long-time dynamics as for the initial condition studied in the main text.For weak couplings the χ_{ESG} values goes to zero with increasing system sizes at long times. For large couplings instead, χ_{ESG} remains finite at long times for all system sizes.

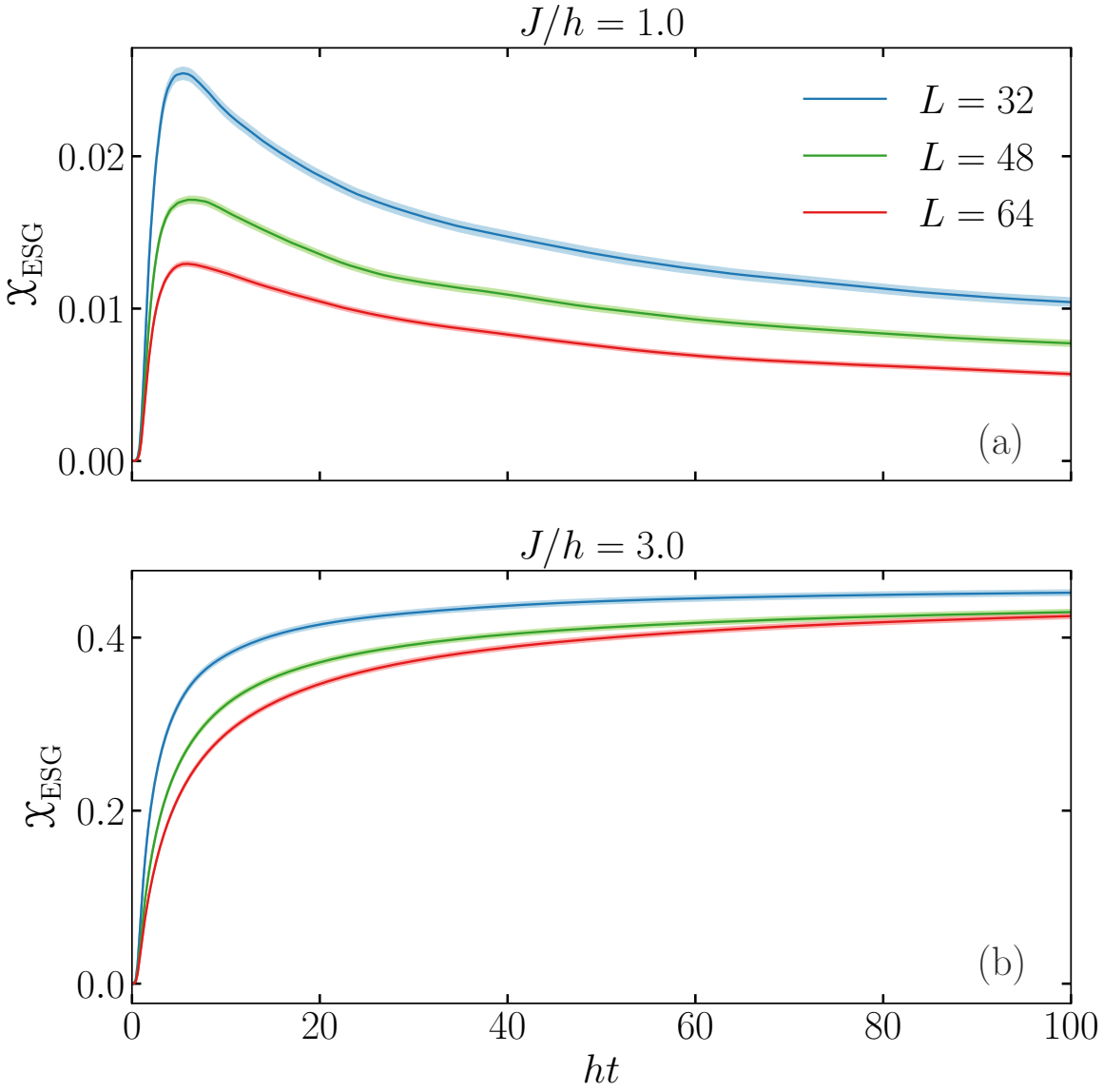

FIGURE 5.3: **Quench dynamics.** Dynamical evolution of χ_{ESG} starting from a state where all spins are initially aligned along the transverse direction. (a) For weak couplings $J/h = 1.0$ χ_{ESG} is small and decays on long-time scales. (b) For larger couplings in the eigenstate spin-glass ordered phase $J/h = 3.0$, χ_{ESG} increases steadily with time approaching a nonzero value in the long-time limit. The shaded region indicates the statistical error in the data due to a finite set of disorder averages.

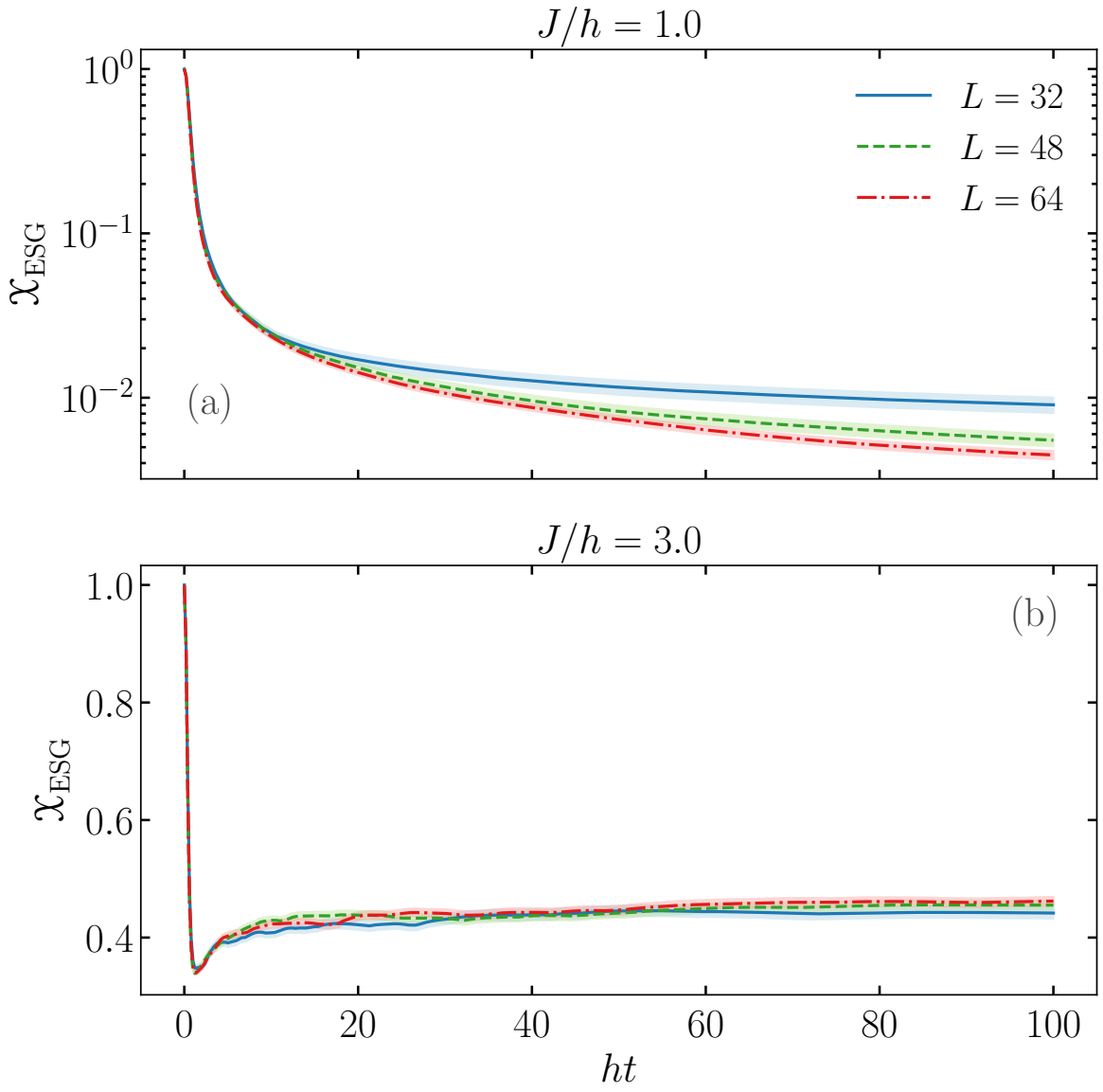

FIGURE 5.4: **Quench dynamics** (a) Shows the dynamical evolution of χ_{ESG} starting from an initial state where all spins initially align along the z- direction. Because of the initially broken $\mathbb{Z}_2$ symmetry at $t = 0$, the χ_{ESG} is non-zero as seen in both the plots. For weak coupling $J/h = 1.0$ the χ_{ESG} decays at long times. (b) For strong couplings $J = 3.0$ the χ_{ESG} becomes finite instead. The shaded region indicates the statistical error in the data.

Idenfifying the transition dynamically in time

Figure 5.5 demonstrates how one could possibly identify the MBL-SG transition dynamically. In each of the panels of this figure we plot for different system size the value of χ_{ESG} as a function of the coupling strength and how this value changes as a function of time t. For each L one can identify two dynamical regimes, one

where $\mathcal{X}_{\mathrm{ESG}}$ increases and one where $\mathcal{X}_{\mathrm{ESG}}$ decays as a function of time within accessible time scales in numerical simulation. We identify the regime where $\mathcal{X}_{\mathrm{ESG}}$ goes to a nonzero value as the MBL-SG phase. From the plots in Fig. 5.5 we observe a crossing point for each system size which suggest that it might be possible to estimate the critical coupling strength for the MBL-SG transition using $\mathcal{X}_{\mathrm{ESG}}$. From our current data, however, this does not appear to be possible accurately. For the exactly solvable case $J_i^x = 0$, it is well known that the MBL spin-glass transition is located at $J/h = 1$ [201]. Computing with tDMRG the dynamics for the same system sizes and times, we find that in this case the crossing point is located around $J \approx 1.2$ [204], which overestimates the region of the MBL paramagnet. We attribute this observation to the slow expected dynamics in these models, which can show slow power-law or also logarithmic relaxation [205]. While the crossing point for the times accessible within tDMRG shows only a weak dependence on time, it is very likely that it exhibits a further slow drift on even longer times scales.

In Fig. 5.6 we show data for $\mathcal{X}_{\mathrm{ESG}}$ in the vicinity of the transition for the integrable case of the model studied in the main text ($J^x = 0$), where the transition is known to be at $J/h = 1$ [201]. From this plot one can again identify two phases separated by a crossing point, with which one might identify the location of the MBL-SG transition in the asymptotic long-time limit. From our finite-time data, however, we find the crossing point at $J/h \approx 1.2$, which overestimates the transition by 20 %. As in the main text, we attribute this discrepancy to the slow dynamics that can occur in these models, which effectively implies that one would need to reach even longer times to see a drift towards the known transition value.

5.5 Long-range correlated Ising Model

In this section we consider a different model and show that also in the presence of long-range interaction the eigenstate order parameter shows the essential behavior of MBL-SG. The model we consider is the following:

$$\mathcal{H} = \frac{1}{N(\alpha)} \sum_{i<j} \frac{\Omega_i \Omega_j}{|i-j|^\alpha} \sigma_i^x \sigma_j^x + \sum_i h_i \sigma_i^z, \tag{5.5}$$

where $N(\alpha) = \sum_{i<j} \frac{1}{|i-j|^\alpha}$ is the Kac normalization. Ω_i is taken from an uniform distribution $[0, W]$, while the field is distributed randomly between $[-h_z, h_z]$. Like in the main text here we also calculated both the Edwards-Anderson parameter $\mathcal{X}_{\mathrm{EA}}$and the eigenstate order parameter $\mathcal{X}_{\mathrm{ESG}}$. It has been theoretically proposed that this model can be realized in current trapped ion experiments [206, 207].

Figure 5.7 shows the parameter dependence of both $\mathcal{X}_{\mathrm{EA}}$ and $\mathcal{X}_{\mathrm{ESG}}$ along with the finite-size dependence. The calculation is performed for excited states taken from the middle of the spectrum and for $\alpha = 2.0$. As one can see the behavior of $\mathcal{X}_{\mathrm{EA}}$ is well reproduced by the $\mathcal{X}_{\mathrm{ESG}}$, however again due to strong finite size effects the critical disorder value for MBL-paramagnet to MBL-SG transition cannot be reliably

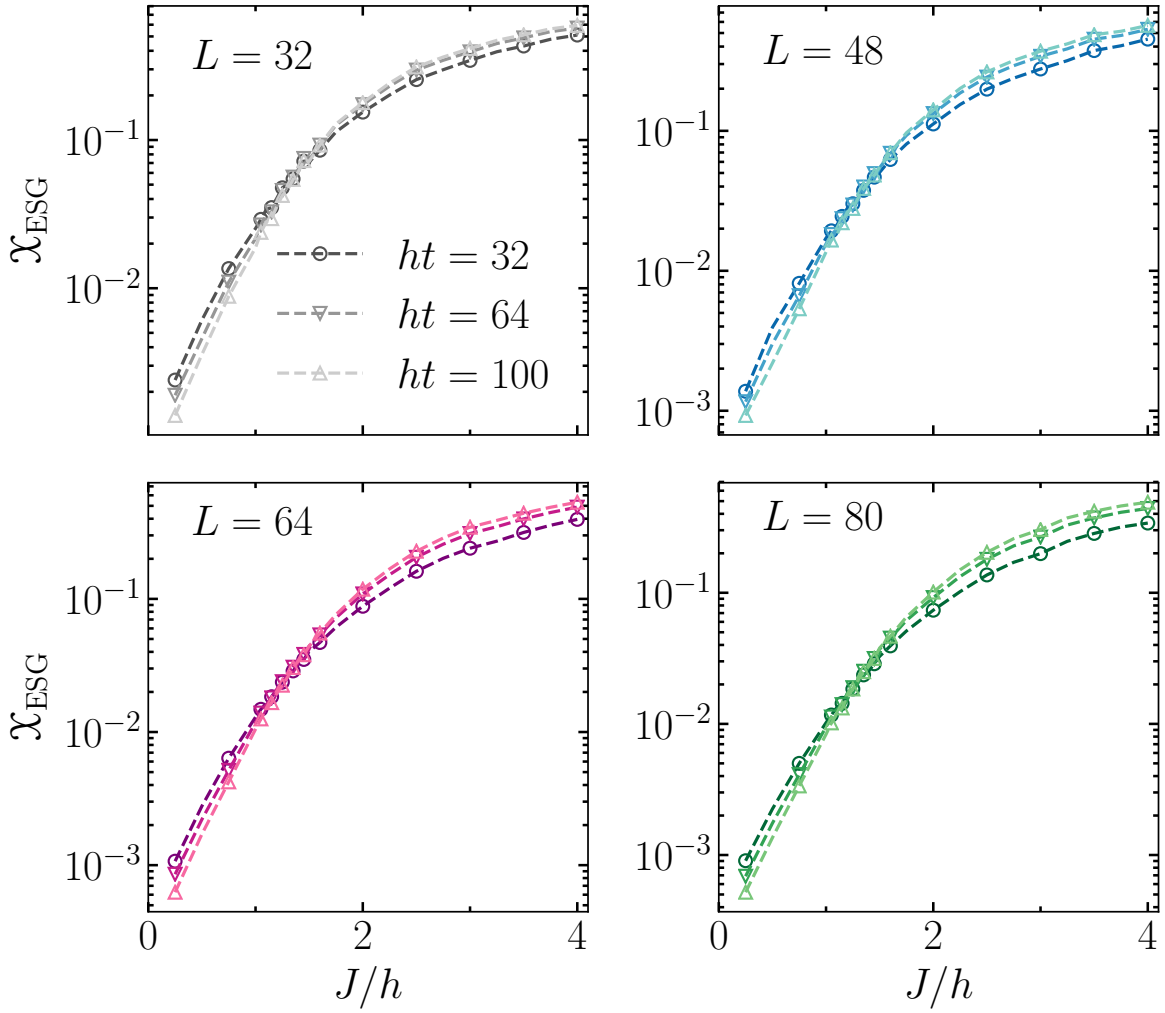

FIGURE 5.5: **Eigenstate spin-glass order parameter across the transition.** Time evolution of χ_{ESG} as a function of disorder strength J/h for different system sizes, $L = 32, 48, 64, 80$ in different panels. For weak couplings χ_{ESG} decays with time, while in the opposite regime it increases. A crossing point separates these regimes of opposite dynamical behavior.

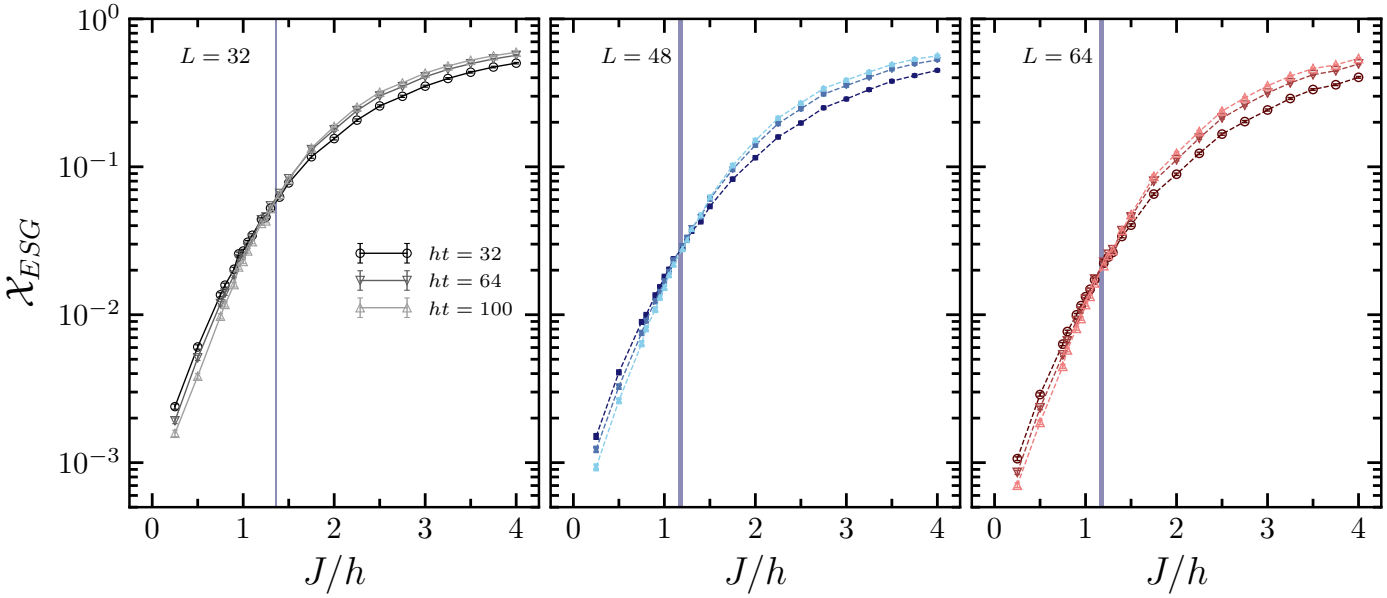

FIGURE 5.6: Eigenstate spin-glass order parameter χ_{ESG} across the transition in the integrable model, where the coupling along the x-direction is taken to be zero ($J^x = 0$, see main text for further details of the model). For weak couplings χ_{ESG} decays with time, while in the other regime it increases.

detected. We have used similar averaging procedure as it is done for all the data in the main text.

5.6 Discussion

In this chapter we have provided evidence that the detection of MBL spin-glass order does not require access in the full many-body eigenstates, as is necessary for the previously used Edwards-Anderson order parameter. We rather find that MBL spin-glass order in random quantum Ising chains is contained in two-spin reduced density matrices.

This observation has several implications. On the theory side, reduced density matrices can be accessed with a variety of methods, whereas full eigenstates require in general the use of exact diagonalization, which a priori limits the accessible system sizes. We have shown in this chapter, for example, that our proposed eigenstate spin-glass (ESG) order parameter can be computed using the density-matrix renormalization group method, which allows us to reach systems up to at least 80 spins. This can be achieved, since the ESG can be obtained from a local in time measurement in contrast to the Edwards-Anderson order parameter, which either requires access to the full eigenstates or to a two-time correlation function.

The property, that the ESG can be obtained by a local in time measurement, not only makes MBL spin-glass order theoretically more easily accessible, but also

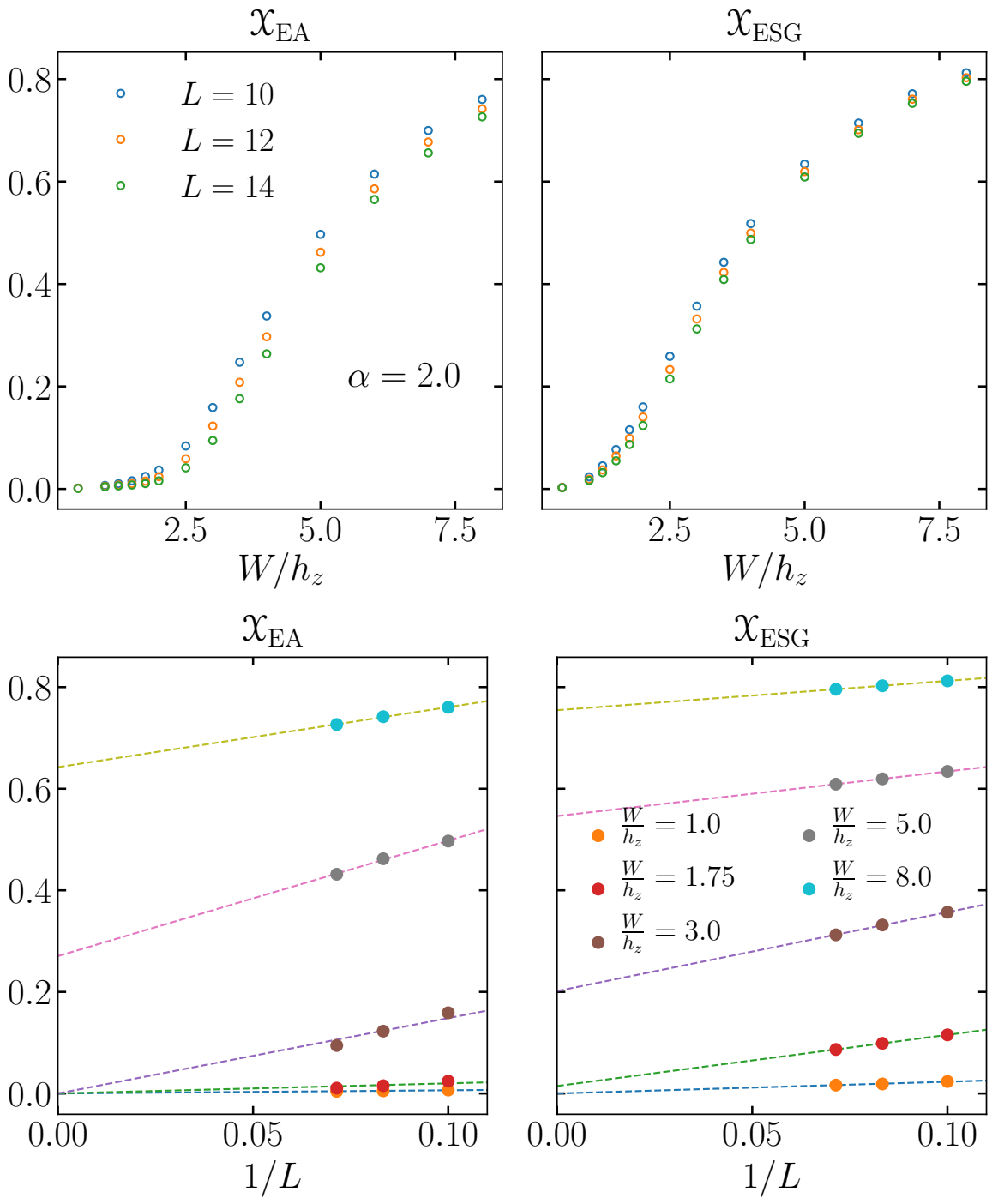

FIGURE 5.7: **Eigenstate order** Upper panel: Shows both the χ_{EA} and χ_{ESG} for the long-range model (5.5) in for excited states taken from the middle of the spectrum. Above $W/h_z \gtrsim 2.5$ the model appears to have a nonzero χ_{EA}, suggesting MBL-SG order. This behavior is also captured by the χ_{ESG} as well. Lower panel shows the L dependence of both the order parameters for few different values of disorder strength as mentioned in the label. Here $\alpha = 2$ is chosen. As in the main text, the lines are a guide to the eye and are not supposed to provide a qualitative extrapolation.

makes an experimental detection more feasible. Still, the ESG requires the full reconstruction of a reduced density matrix of two spins. While this limits the range of applicable experimental platforms, reduced density matrices are accessible in so-called quantum simulators such as trapped ions [208, 209], superconducting qubits [210], Rydberg systems, or ultra-cold atoms in optical lattices [211]. The observation of MBL spin-glass order remains nevertheless challenging since the experimental realization of system Hamiltonians, that are capable to host MBL spin-glass ordered phases, has not yet been reported. For trapped ions systems, however, a way to generate an Ising Hamiltonian with random spin interactions has been proposed [206, 207]. In general, random interactions might also be straightforwardly realized using the digital approach to quantum simulation [212, 213, 210] which is currently limited, however, by the accessible system sizes.

We have analyzed the ESG for a random quantum Ising chain, so that it is a natural question to which extent our results generalize to other models. While addressing this question on general grounds is beyond of the scope of this work, we also showed numerical results for a long-range Ising model with algebraically decaying spin-spin interactions, whose realization in a trapped ion system appears feasible within current experimental techniques. While finite-size effects in this model are stronger than for the nearest-neighbor Ising chain, we find a similar behavior of the Edwards-Anderson order parameter and the ESG, indicating that our results extend beyond the particular quantum Ising chain studied here.

Chapter 6

Conclusion

6.1 Summary

In this thesis, we have considered three different topics in modern condensed matter physics. We have studied these topics with state-of-art numerical techniques: lattice Monte Carlo and tensor network methods. Each of the topics reflects a different aspect of the field. However There are other important topics in modern condensed matter that we could not survey due to the time limitations, for example, the topological phase of matter or high-temperature superconductivity and so on.

In chapter 3, we revisited the phase diagram of Falicov-Kimball model. Especially we addressed the intricacies of the phase diagram above the charge ordering transition. We found out that the WL regime is due to the finiteness of the underlying lattice and vanishes in the thermodynamic limit. The AI phase is captured by disorder extensions of the DMFT with the addition of quenched disorder. We have studied the charged ordered phase in detail and found out the critical exponents associated with the onset of charge order in that region coincide with those of the classical two-dimensional Ising model.

In chapter 4, we have studied the spatial structure of entanglement for transverse field Ising chain using logarithmic negativity at zero and nonzero temperatures. We have found that for any fixed size ℓ of the blocks there exists an entanglement threshold at a distance d^* beyond which the logarithmic negativity vanishes identically. This holds across the whole phase diagram of the system including also the quantum critical point where the system exhibits long-ranged quantum correlations. The influence of temperature onto the spatial entanglement structure as measured by the logarithmic negativity depends crucially on the size ℓ of the blocks. The larger d^* (for increasing ℓ) the more important the influence of temperature, cutting off long-range entanglement. Logrithmic negativity is based on PPT criterion and for larger blocks $\ell \geq 2$, although it might be zero for larger distances but this does not necessarily imply that the two blocks are completely unentangled. But as well we can not exclude that there exist other measures signaling nonzero entanglement. However it is important to keep in mind that the logarithmic negativity gives a bound on the distilable entanglement, such that a vanishing logarithmic negativity implies that no Bell pairs can be extracted from the state.

In chapter 5 we considered MBL phase of matter where the effects of disorder become important. Our focus was inside the MBL phase that hosts another interesting

phase, the so-called MBL spin-glass phase. We have introduced an order parameter called eigenstate spin-glass order parameter. It overcome the current dynamical and experimental challenges to detect this phase. We have provided evidence that the detection of MBL spin-glass order does not require access to the full many-body eigenstates, as is necessary for the previously used Edwards-Anderson order parameter. We rather find that MBL spin-glass order in random quantum Ising chains is contained in two-spin reduced density matrices.

We find that this ESG order parameter captures MBL spin-glass phases in random Ising chains both in many-body eigenstates as well as in the nonequilibrium dynamics from a local in time measurement.

6.2 Outlook

The performed results in chapter 3 may shed some light on the study of other types of lattices, for instance, triangular lattice in which one has to consider the frustration effects or three-dimensional lattices. As well the results might be useful for studies of localization in cold atoms. Recently, using neural networks and machine learning techniques, people have studied different problems in condensed matter physics. One can for future studies use such methods for bigger lattices and higher dimensions.

Regarding chapter 4, for future considerations, it is interesting to look at the behavior of logarithmic negativity for other models and with different natures. It also would be interesting to study the dynamic properties of entanglement dynamics and its propagation with time for different model following a quantum quench. This can help to understand these problems from a different point of view.

Using our results in chapter 5, one can dynamically study the systems that show a spin-glass phase in the context of MBL phase. As we have discussed there in our results, one can access the reduced density matrix experimentally, for example, our results can be used to observe MBL spin-glass order within current experiments in Rydberg atoms and trapped ion systems. This lets to measure the amount of glassiness in such systems in the laboratory. Recent works on floquet-driven MBL systems and time crystals[214, 215, 216, 217, 218] suggest a glass phase in their phase diagram. This can be motivating to investigate these systems and their MBL spin-glass phases spatially in space and time using our order parameter.

Appendix A

Coherent state path integral

From coherent state path integral formalism we can write the partition function as follow

$$Z = \int_{\substack{\bar{\psi}(\beta) = -\zeta\bar{\psi}(0) \\ \psi(\beta) = -\zeta\psi(0)}} D(\bar{\psi},\psi) e^{-S[\bar{\psi},\psi]} \tag{A.1}$$

and

$$S[\bar{\psi},\psi] = \int_0^\beta d\tau \left(\bar{\psi}\cdot\partial_\tau\psi + H(\bar{\psi},\psi) - \mu N(\bar{\psi},\psi)\right) \tag{A.2}$$

for the general Hamiltonian

$$H - \mu N = \sum_{i,j} \left(h_{ij} - \mu\delta_{ij}\right) a_i^\dagger a_j + \sum_{ij\ldots kl} V_{ijkl} a_i^\dagger a_j^\dagger \ldots a_k a_l \tag{A.3}$$

we have

$$S\left[\bar{\psi},\psi\right] = \int_0^\beta d\tau \left[\sum_{ij} \bar{\psi}_i(\tau)\left[(\partial_\tau - \mu)\delta_{ij} + h_{ij}\right]\psi_j(\tau) + \sum_{ij\ldots kl} V_{ijkl}\bar{\psi}_i(\tau)\bar{\psi}_j(\tau)\ldots\psi_k(\tau)\psi_l(\tau)\right] \tag{A.4}$$

in frequency domain and if V is a two body operator we have

$$S\left[\bar{\psi},\psi\right] = \sum_{ij\omega_n} \bar{\psi}_{i\omega_n}\left[(i\omega_n - \mu)\delta_{ij} + h_{ij}\right]\psi_{j\omega_n} \tag{A.5}$$

$$+ \frac{1}{\beta}\sum_{ijkl}\sum_{\omega_{n_1}\omega_{n_2}\omega_{n_3}\omega_{n_4}} V_{ijkl}\bar{\psi}_{i\omega_{n_1}}\bar{\psi}_{i\omega_{n_2}}\psi_{j\omega_{n_3}}\psi_{l\omega_{n_4}}\delta_{\omega_{n_1}+\omega_{n_2},\omega_{n_3}\omega_{n_4}} \tag{A.6}$$

with

$$\omega_n = \begin{cases} 2n\pi/\beta & \text{bosons} \\ (2n+1)\pi/\beta & \text{fermions.} \end{cases} \quad n \in \mathcal{Z}$$

also it is possible to write the action as follow

$$\begin{aligned} S &= S_0 + S_{int} \\ &= \sum_{ij\omega_n} \bar{\psi}_{i\omega_n}\left[(G_0)^{-1}\right]\psi_{j\omega_n} + S_{int} \end{aligned} \tag{A.7}$$

Generally we can write Z as follow

$$Z = Z_0 \langle e^{-\int_0^\beta d\tau V(\bar{\psi}_i(\tau)\bar{\psi}_j(\tau)...\psi_k(\tau)\psi_l(\tau))} \rangle_0 \tag{A.8}$$

where $\langle e^{-\int_0^\beta d\tau V(\bar{\psi}_i(\tau)\bar{\psi}_j(\tau)...\psi_k(\tau)\psi_l(\tau))} \rangle_0$ is

$$\langle e^{-\int_0^\beta d\tau V(\bar{\psi}_i(\tau)\bar{\psi}_j(\tau)...\psi_k(\tau)\psi_l(\tau))} \rangle_0 = \frac{1}{Z_0} \int_{\substack{\bar{\psi}(\beta) = -\zeta\bar{\psi}(0) \\ \psi(\beta) = -\zeta\psi(0)}} D(\bar{\psi}, \psi) e^{-S[\bar{\psi},\psi]} \tag{A.9}$$

and

$$Z_0 = \int_{\substack{\bar{\psi}(\beta) = -\zeta\bar{\psi}(0) \\ \psi(\beta) = -\zeta\psi(0)}} D(\bar{\psi}, \psi) e^{-S_0[\bar{\psi},\psi]} \tag{A.10}$$

where S_0 is action without interaction or perturbation.

Appendix B

Finite size scaling

We know that the phase transition occur only in thermodynamic limit and due to finite memory and processing time, it is not possible to do the calculation in thermodynamic limit, for this reason physicists do the simulation for finite lattice sizes and then with scaling hypothesis, analyze finite systems and deduce conclusions for thermodynamic limit. This method of scaling called *Finite Size Scaling* or *FSS*.

B.0.1 Critical exponent

When we are near the critical point T_c, a quantity like $g(t)$ obeys a exponential law as

$$g(t) = |t|^{\lambda} \tag{B.1}$$

And $t = \dfrac{T - T_c}{T_c}$. This g could be specific heat C_v or susceptibility χ or any related quantity on problem. In our problem and in square lattice g is C_v and χ_f. λ is critical exponent of the $g(t)$ and determine as

$$\lambda = \lim_{t \to 0} \frac{\ln g(t)}{\ln t} \tag{B.2}$$

So t^{λ} describes $g(t)$ at the transition.

B.0.2 Scaling hypothesis

For the quantity $g(t)$ we have following scaling behavior at T_c

$$g(t) \sim L^{\lambda/\nu} \Phi_g(tL^{1/\nu}) \tag{B.3}$$

and $\Phi_g(tL^{1/\nu})$ is universal scaling function.

Thermodynamic limit	Finite size system
$\chi_f(t) \sim \lvert t\rvert^{-\gamma}$	$\chi_f(t) \sim L^{-\gamma/\nu}\Phi_{\chi_f}(tL^{1/\nu})$
$C_v(t) \sim \lvert t\rvert^{-\alpha}$	$C_v(t) \sim L^{-\alpha/\nu}\Phi_{C_v}(tL^{1/\nu})$

TABLE B.1: Thermodynamic limit and finite size system.

B.0.3 The results of the FSS

The results of finite size scaling is to extract the correct set of values of exponents including ν, γ, α and T_c from results that we gain from simulation, Fig. 3.8 a,b and c. Fortunately we have T_c from our results and there is no need to calculate it with FSS. With fourth order Binder Cumulant $B_{\vec{Q}}$ we can calculate the T_c .
Also there is scaling behavior for fourth order Binder Cumulant $B_{\vec{Q}}$ [85] as follow

$$B_{\vec{Q}} = \tilde{B}_{\vec{Q}}(tL^{1/\nu}) \tag{B.4}$$

Then after FSS, to extract scaling function $\phi_Q(tL^{1/\nu})$ from numerical data one could define

$$y_L = g(t)L^{-\lambda/\nu} \quad , \quad x_L = tL^{1/\nu} \tag{B.5}$$

B.0.4 How to do FSS

for this aim, in equation B.3 with Taylor expansion of $\Phi_g(tL^{1/\nu})$ convert it to polynomial form and keep N first terms as follow

$$\Phi_g(tL^{1/\nu}) = L^{\lambda/\nu}(a_0 + a_1L^{1/\nu}t + a_2L^{2/\nu}t^2 + a_3L^{3/\nu}t^3 + a_4L^{4/\nu}t^4 + ... + a_NL^{N/\nu}t^N) \tag{B.6}$$

From numerical data by using only the temperatures adequately close to T_c for different lattice sizes we can extract a_0, a_1, a_2 ,..., a_N, T_c, λ and ν by fitting B.6 with numerical data.

Appendix C

Schmidt Decomposition

Any vector $|\Psi\rangle \in \mathcal{H}_1 \otimes \mathcal{H}_2$ can be expressed in the form

$$|\Psi\rangle = \sum_j \lambda_j \left|\Phi_j^L\right\rangle \left|\Phi_j^R\right\rangle \tag{C.1}$$

for non-negative real λ_j so-called Schmidt values, and orthonormal sets $\left|\Phi_j^L\right\rangle \in \mathcal{H}_1$ and $\left|\Phi_j^L\right\rangle \in \mathcal{H}_2$ with $j = 1, 2, 3, \ldots$. There are density operators ρ_1 on $\mathcal{H}_1$ and ρ_2 on $\mathcal{H}_2$ such that

$$\langle\Psi|(A \otimes 1)|\Psi\rangle = \mathrm{Tr}[A\rho_1], \quad \langle\Psi|(1 \otimes B)|\Psi\rangle = \mathrm{Tr}[B\rho_2] \tag{C.2}$$

for all observables A and B on $\mathcal{H}_1$ and $\mathcal{H}_2$, respectively, and $\{\left|\Phi_j^L\right\rangle\}$ may be chosen to be the eigenverctors of ρ_1 corresponding to nonzero eigenvalues $\{p_j\}$ and the vectors $\{\left|\Phi_j^R\right\rangle\}$, the corresponding eigenvectors for ρ_2, and the positive scalars $c_j = \sqrt{p_j}$.

Appendix D

Error analysis in TEBD for ESG order parameter

D.1 Optimal choice of TEBD parameters:

In order to reach long simulation time t one has to find optimal control parameters, which are time step dt, and the number of the truncated states (kept state) χ_{max}. We implemented the TEBD algorithm is such a way that we discarded states below certain threshold, ε.

Therefore the control parameters are the time step dt and the truncation error threshold is ε. The total error would increase at larger dt due to the Trotter error, and at smaller dt due to the truncation error. It is reasonable to choose for small times rather small values of dt in order to minimize the Trotter error and for large times, to choose a somewhat coarser time interval, in order to push the time to as large as possible [219]. We choose two small value for dt

$$hdt \in [0.01, 0.005] \tag{D.1}$$

and for ε we consider different truncation thresholds

$$\varepsilon \in [1e-7, 1e-9, 1e-11] \tag{D.2}$$

In the Following we do the error analysis for two different initial states, first error analysis for the results that we have shown in the main text of the paper and second for initial state that break the Z_2 symmetry of the system in the z-direction, i.e., an initial state where all spins are pointed randomly in the z-direction.

Figure D.1 and D.2 shows the error analysis for the initial states, which is product state randomly directed in x-direction and z-direction respectively. Note that we average over 1000 realizations for this simulation. In each set of TEBD parameters, i.e., ε and dt, the initial states remain unchanged, which give us confident that results shown here and in the main text are well converged.

Figure D.1 right panel shows the evolution of the $\mathcal{X}_{\mathrm{ESG}}$ for different TEBD parameters starting with an initial state, which is randomly pointed in z-direction. As it is seen that for all the parameters choice of the TEBD algorithm the dynamics remain unaffected. Here the discarded weight remains very small of the order $1e-16$.

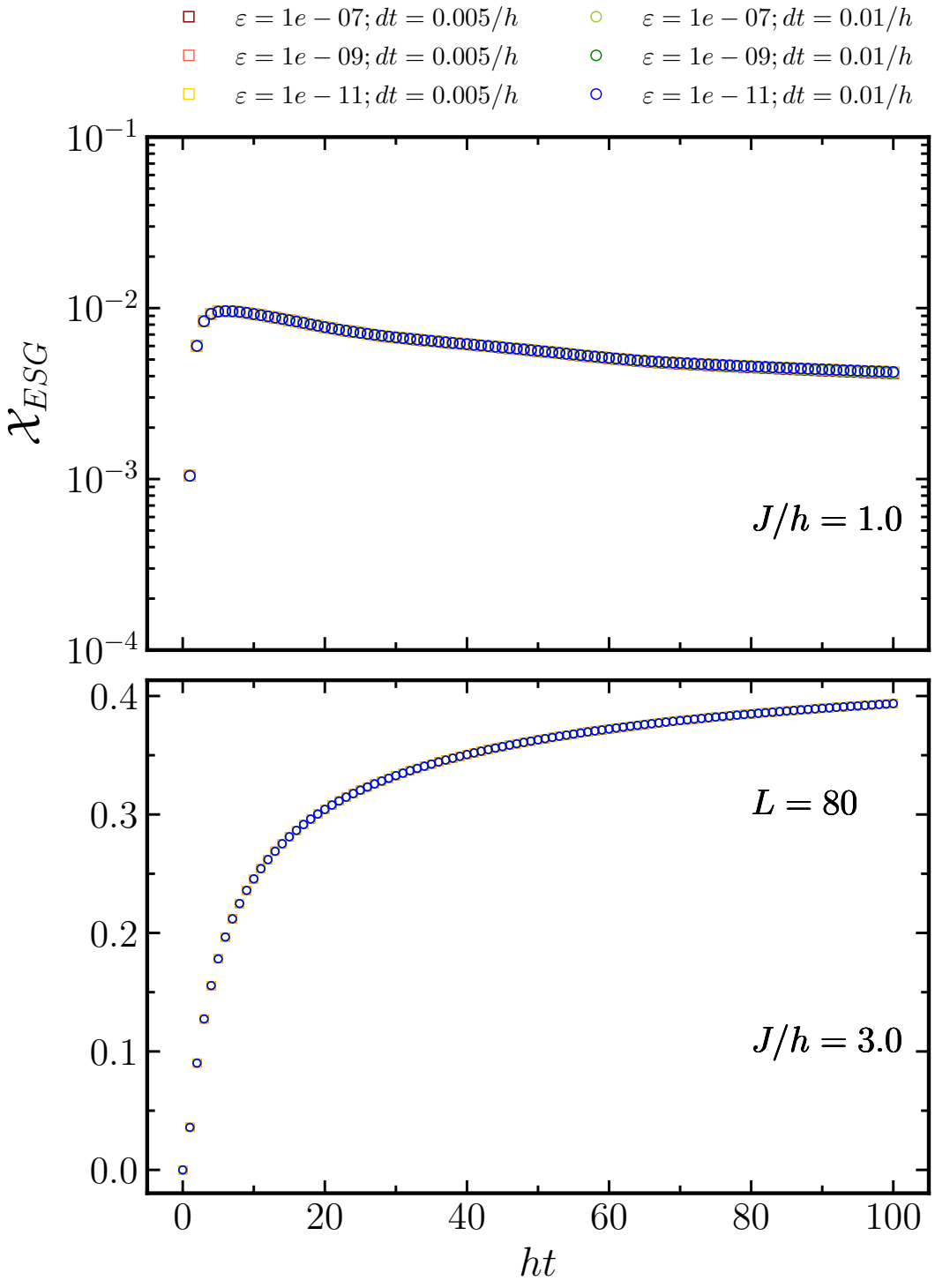

FIGURE D.1: Error analysis for different set of parameters (ε, dt) for non-MBL SG, $J/h = 1.0$, and MBL-SG, $J/h = 3.0$, phases for a chain $L = 80$ with all initial states randomly pointed in the x-direction.

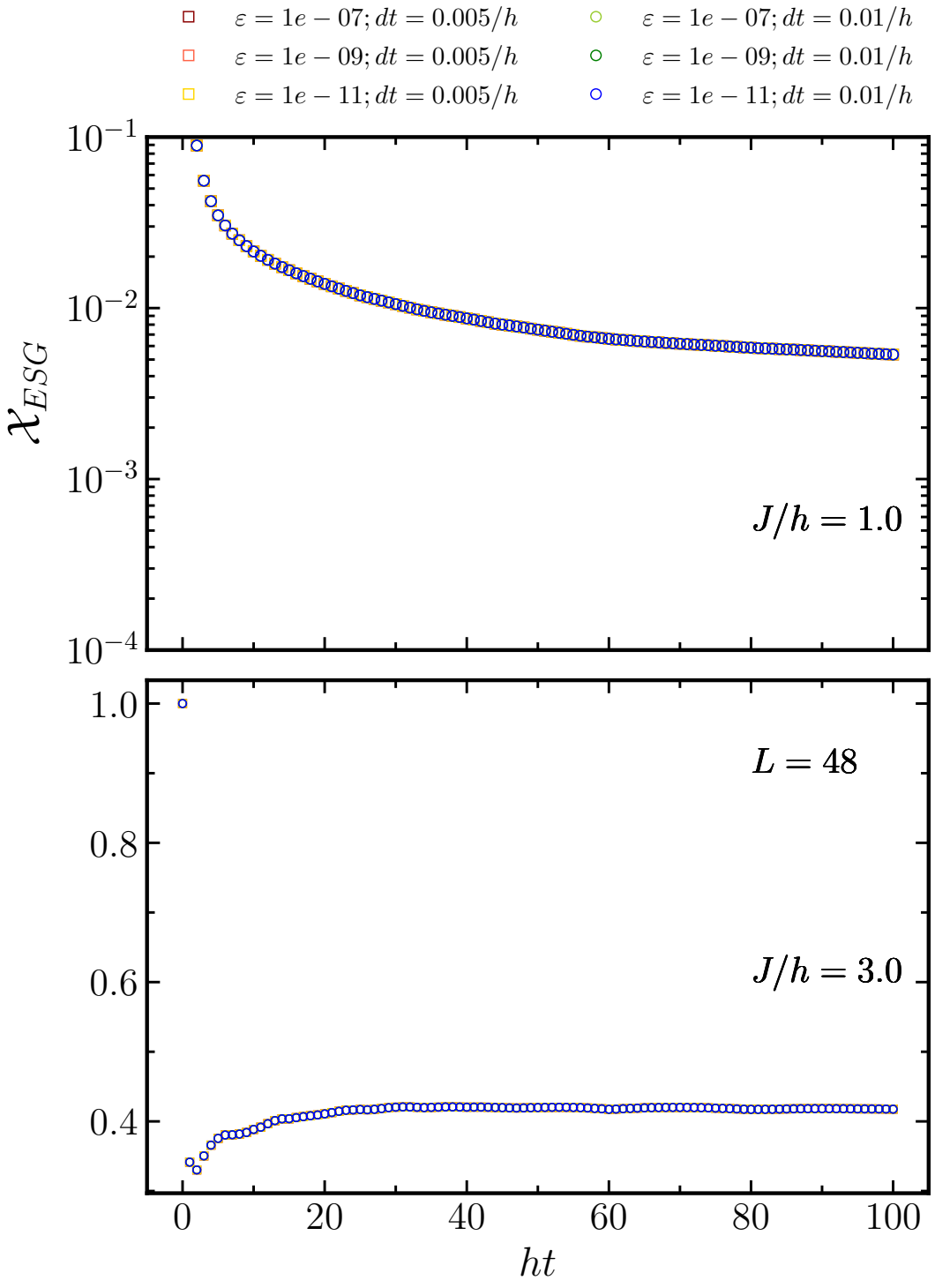

FIGURE D.2: Error analysis for different set of parameters (ε, dt) for non-MBL SG, $J/h = 1.0$, and MBL-SG, $J/h = 3.0$, phases for a chain $L = 48$ with all initial states randomly pointed in the z-direction.

Bibliography

[1] L. LANDAU. "The Theory of Phase Transitions". In: *Nature* 138.3498 (1936), pp. 840–841. ISSN: 0028-0836. DOI: 10.1038/138840a0. URL: http://www.nature.com/articles/138840a0.

[2] Subir Sachdev. *Quantum Phase Transitions*. 2nd ed. Cambridge University Press, 2011. DOI: 10.1017/CBO9780511973765.

[3] Thomas Vojta. "Quantum phase transitions". In: *News and Views* 4 (2000), pp. 167–204. ISSN: 0034-4885. DOI: 10.1088/0034-4885/66/12/R01. arXiv: 0010285 [cond-mat]. URL: http://www.nature.com/nphys/focus/quantum-phase-transitions/index.htmlhttp://arxiv.org/abs/cond-mat/0010285.

[4] Matthias Vojta and Matthias Vojta. "Quantum phase transitions". In: *Repts. Prog. Phys.* 66.12 (2003), pp. 2069–2110. ISSN: 0034-4885. DOI: 10.1088/0034-4885/66/12/R01. arXiv: 0309604v2 [cond-mat]. URL: http://stacks.iop.org/0034-4885/66/i=12/a=R01?key=crossref.c536678c9f7b611291c4445db9c68861.

[5] N Goldenfeld. *Lectures on Phase Transitions and the Renormalization Group*. 1992. DOI: citeulike-article-id:3771437. URL: http://www.amazon.com/gp/redirect.html?ASIN=0201554097{\&}tag=ws{\&}lcode=xm2{\&}cID=2025{\&}ccmID=165953{\&}location=/o/ASIN/0201554097?SubscriptionId=0NM5T5X751JWT17C4GG2.

[6] F. Steglich et al. "Superconductivity in the Presence of Strong Pauli Paramagnetism: $CeCu_2Si_2$". In: *Phys. Rev. Lett.* 43 (25 1979), pp. 1892–1896. DOI: 10.1103/PhysRevLett.43.1892. URL: https://link.aps.org/doi/10.1103/PhysRevLett.43.1892.

[7] Z Fisk et al. "The physics and chemistry of heavy fermions". In: *Proceedings of the National Academy of Sciences* 92.15 (1995), pp. 6663–6667. ISSN: 0027-8424. eprint: http://www.pnas.org/content/92/15/6663.full.pdf. URL: http://www.pnas.org/content/92/15/6663.

[8] Piers Coleman. *Introduction to Many-Body Physics*. Cambridge University Press, 2015. DOI: 10.1017/CBO9781139020916.

[9] S. Doniach. "The Insulator-Metal Transition". In: *Advances in Physics* 18.76 (1969), pp. 819–848. ISSN: 14606976. DOI: 10.1080/00018736900101397.

[10] N. F. Mott and W. D. Twose. "The theory of impurity conduction". In: *Advances in Physics* 10.38 (1961), pp. 107–163. ISSN: 14606976. DOI: 10.1080/00018736100101271.

[11] D.M. Basko, I.L. Aleiner, and B.L. Altshuler. "Metal–insulator transition in a weakly interacting many-electron system with localized single-particle states". In: *Ann. Phys.* 321.5 (2006), pp. 1126–1205. ISSN: 0003-4916. DOI: 10.1016/j.aop.2005.11.014. URL: http://www.sciencedirect.com/science/article/pii/S0003491605002630.

[12] N. F. Mott and R. Peierls. *Discussion of the paper by de Boer and Verwey*. 1937. DOI: 10.1088/0959-5309/49/4S/308.

[13] N. F. Mott. "The basis of the electron theory of metals, with special reference to the transition metals". In: *Proceedings of the Physical Society. Section A* 62.7 (1949), pp. 416–422. ISSN: 03701298. DOI: 10.1088/0370-1298/62/7/303.

[14] Masatoshi Imada, Atsushi Fujimori, and Yoshinori Tokura. "Metal-insulator transitions". In: *Rev. Mod. Phys.* 70 (4 1998), pp. 1039–1263. DOI: 10.1103/RevModPhys.70.1039. URL: https://link.aps.org/doi/10.1103/RevModPhys.70.1039.

[15] Pasquale Calabrese. "Entanglement and thermodynamics in non-equilibrium isolated quantum systems". In: *Physica A: Statistical Mechanics and its Applications* 504 (2018), pp. 31–44. ISSN: 03784371. DOI: 10.1016/j.physa.2017.10.011.

[16] Anatoli Polkovnikov et al. "Colloquium: Nonequilibrium dynamics of closed interacting quantum systems". In: *Rev. Mod. Phys.* 83 (3 2011), pp. 863–883. DOI: 10.1103/RevModPhys.83.863. URL: https://link.aps.org/doi/10.1103/RevModPhys.83.863.

[17] J. M. Deutsch. "Quantum statistical mechanics in a closed system". In: *Phys. Rev. A* 43 (4 1991), pp. 2046–2049. DOI: 10.1103/PhysRevA.43.2046. URL: https://link.aps.org/doi/10.1103/PhysRevA.43.2046.

[18] Mark Srednicki. "Chaos and quantum thermalization". In: *Phys. Rev. E* 50 (2 1994), pp. 888–901. DOI: 10.1103/PhysRevE.50.888. URL: https://link.aps.org/doi/10.1103/PhysRevE.50.888.

[19] Sheldon Goldstein et al. "Canonical Typicality". In: *Phys. Rev. Lett.* 96 (5 2006), p. 050403. DOI: 10.1103/PhysRevLett.96.050403. URL: https://link.aps.org/doi/10.1103/PhysRevLett.96.050403.

[20] Jochen Gemmer, Alexander Otte, and Günter Mahler. "Quantum Approach to a Derivation of the Second Law of Thermodynamics". In: *Phys. Rev. Lett.* 86 (10 2001), pp. 1927–1930. DOI: 10.1103/PhysRevLett.86.1927. URL: https://link.aps.org/doi/10.1103/PhysRevLett.86.1927.

[21] Anatoly Dymarsky, Nima Lashkari, and Hong Liu. "Subsystem eigenstate thermalization hypothesis". In: *Phys. Rev. E* 97 (1 2018), p. 012140. DOI: 10.1103/PhysRevE.97.012140. URL: https://link.aps.org/doi/10.1103/PhysRevE.97.012140.

[22] Sandu Popescu, Anthony J. Short, and Andreas Winter. "Entanglement and the foundations of statistical mechanics". In: *Nat. Phys.* 2 (Oct. 2006), 754 EP –. URL: http://dx.doi.org/10.1038/nphys444.

[23] P. W. Anderson. "Absence of Diffusion in Certain Random Lattices". In: *Phys. Rev.* 109 (5 1958), pp. 1492–1505. DOI: 10.1103/PhysRev.109.1492. URL: https://link.aps.org/doi/10.1103/PhysRev.109.1492.

[24] Arijeet Pal and David A. Huse. "Many-body localization phase transition". In: *Phys. Rev. B* 82 (17 2010), p. 174411. DOI: 10.1103/PhysRevB.82.174411. URL: http://link.aps.org/doi/10.1103/PhysRevB.82.174411.

[25] Rahul Nandkishore and David A. Huse. "Many-Body Localization and Thermalization in Quantum Statistical Mechanics". In: *Annual Review of Condensed Matter Physics* 6.1 (2015), pp. 15–38. DOI: 10.1146/annurev-conmatphys-031214-014726. eprint: https://doi.org/10.1146/annurev-conmatphys-031214-014726. URL: https://doi.org/10.1146/annurev-conmatphys-031214-014726.

[26] Rahul Nandkishore and David A. Huse. "Many-Body Localization and Thermalization in Quantum Statistical Mechanics". In: *Annu. Rev. Condens. Matter Phys.* 6.1 (2015), pp. 15–38. ISSN: 1947-5454. DOI: 10.1146/annurev-conmatphys-031214-014726. URL: http://www.annualreviews.org/doi/abs/10.1146/annurev-conmatphys-031214-014726http://www.annualreviews.org/doi/10.1146/annurev-conmatphys-031214-014726.

[27] Giulio Biroli, Corinna Kollath, and Andreas M. Läuchli. "Effect of Rare Fluctuations on the Thermalization of Isolated Quantum Systems". In: *Phys. Rev. Lett.* 105 (25 2010), p. 250401. DOI: 10.1103/PhysRevLett.105.250401. URL: https://link.aps.org/doi/10.1103/PhysRevLett.105.250401.

[28] Hal Tasaki. "From Quantum Dynamics to the Canonical Distribution: General Picture and a Rigorous Example". In: *Phys. Rev. Lett.* 80 (7 1998), pp. 1373–1376. DOI: 10.1103/PhysRevLett.80.1373. URL: https://link.aps.org/doi/10.1103/PhysRevLett.80.1373.

[29] Leon Balents. "Spin liquids in frustrated magnets". In: *Nature* 464.7286 (2010), pp. 199–208. URL: https://www.nature.com/articles/nature08917.

[30] Lucile Savary and Leon Balents. "Quantum spin liquids: a review". In: *Rep. Prog. Phys.* 80.1 (2017), p. 016502. URL: http://stacks.iop.org/0034-4885/80/i=1/a=016502.

[31] Frank Pollmann et al. "Entanglement spectrum of a topological phase in one dimension". In: *Phys. Rev. B* 81.6 (2010), p. 064439. URL: https://link.aps.org/doi/10.1103/PhysRevB.81.064439.

[32] Hong-Chen Jiang, Zhenghan Wang, and Leon Balents. "Identifying topological order by entanglement entropy". In: *Nat. Phys.* 8.12 (2012), pp. 902–905. URL: https://www.nature.com/articles/nphys2465.

[33] Marko Žnidarič, Tomaž Prosen, and Peter Prelovšek. "Many-body localization in the Heisenberg XXZ magnet in a random field". In: *Phys. Rev. B* 77.6 (2008), p. 064426.

[34] Jens H Bardarson, Frank Pollmann, and Joel E Moore. "Unbounded growth of entanglement in models of many-body localization". In: *Phys. Rev. Lett.* 109.1 (2012), p. 017202.

[35] K. Macieszczak et al. "Coherence, entanglement and quantumness in closed and open systems with conserved charge, with an application to many-body localisation". In: *arXiv:1805.00079* (Apr. 2018). arXiv: 1805.00079.

[36] Bela Bauer and Chetan Nayak. "Area laws in a many-body localized state and its implications for topological order". In: *J. Stat. Mech. Theory Exp.* 2013.09 (2013), P09005. URL: http://stacks.iop.org/1742-5468/2013/i=09/a=P09005.

[37] H Eugene Stanley. "Scaling, universality, and renormalization: Three pillars of modern critical phenomena". In: *Rev. Mod. Phys.* 71.2 (1999), S358.

[38] G. Vidal et al. "Entanglement in Quantum Critical Phenomena". In: *Phys. Rev. Lett.* 90 (22 2003), p. 227902. DOI: 10.1103/PhysRevLett.90.227902. URL: https://link.aps.org/doi/10.1103/PhysRevLett.90.227902.

[39] Vincenzo Alba. "Entanglement negativity and conformal field theory: a Monte Carlo study". In: *J. Stat. Mech. Theory Exp.* 2013.05 (2013), P05013.

[40] Pasquale Calabrese and John Cardy. "Entanglement entropy and conformal field theory". In: *J. Phys. A* 42.50 (2009), p. 504005.

[41] A. Osterloh et al. "Scaling of entanglement close to a quantum phase transition". In: *Nature* 416.6881 (2002), pp. 608–610. ISSN: 00280836. DOI: 10.1038/416608a. eprint: 0202029 (quant-ph).

[42] Nicolai Friis et al. "Observation of Entangled States of a Fully Controlled 20-Qubit System". In: *Phys. Rev. X* 8 (2 2018), p. 021012. DOI: 10.1103/PhysRevX.8.021012. URL: https://link.aps.org/doi/10.1103/PhysRevX.8.021012.

[43] Kihwan Kim et al. "Quantum simulation of frustrated Ising spins with trapped ions". In: *Nature* 465.7298 (2010), pp. 590–593.

[44] Petar Jurcevic et al. "Quasiparticle engineering and entanglement propagation in a quantum many-body system". In: *Nature* 511.7508 (2014), pp. 202–205.

[45] Takeshi Fukuhara et al. "Spatially resolved detection of a spin-entanglement wave in a Bose-Hubbard chain". In: *Phys. Rev. Lett.* 115.3 (2015), p. 035302.

[46] Esteban A Martinez et al. "Real-time dynamics of lattice gauge theories with a few-qubit quantum computer". In: *Nature* 534.7608 (2016), pp. 516–519.

[47] P. Jurcevic et al. "Direct Observation of Dynamical Quantum Phase Transitions in an Interacting Many-Body System". In: *Phys. Rev. Lett.* 119 (8 2017), p. 080501. DOI: 10.1103/PhysRevLett.119.080501. URL: https://link.aps.org/doi/10.1103/PhysRevLett.119.080501.

[48] AJ Daley et al. "Measuring entanglement growth in quench dynamics of bosons in an optical lattice". In: *Phys. Rev. Lett.* 109.2 (2012), p. 020505.

[49] Rajibul Islam et al. "Measuring entanglement entropy in a quantum many-body system". In: *Nature* 528.7580 (2015), pp. 77–83.

[50] Adam M Kaufman et al. "Quantum thermalization through entanglement in an isolated many-body system". In: *Science* 353.6301 (2016), pp. 794–800.

[51] Andreas Elben et al. "Renyi Entropies from Random Quenches in Atomic Hubbard and Spin Models". In: *arXiv:1709.05060* (2017).

[52] B Vermersch et al. "Unitary n-designs via random quenches in atomic Hubbard and Spin models: Application to the measurement of Renyi entropies". In: *arXiv:1801.00999* (2018).

[53] Giacomo Torlai et al. "Many-body quantum state tomography with neural networks". In: *arXiv:1703.05334* (2017).

[54] Shiwei Zhang. *Theoretical Methods for Strongly Correlated Electrons*. Ed. by David Sénéchal, André-Marie Tremblay, and Claude Bourbonnais. CRM Series in Mathematical Physics 1. New York: Springer-Verlag, 2004, pp. 39–74. ISBN: 0-387-00895-0. DOI: 10.1007/b97552. arXiv: arXiv:1011.1669v3. URL: http://link.springer.com/10.1007/0-387-21717-7{_}2{\%}0Ahttp://link.springer.com/10.1007/b97552http://link.springer.com/10.1007/b97552.

[55] J. K. Freericks, familyi=c., given=V., giveni=V., „ and. "Exact dynamical mean-field theory of the Falicov-Kimball model". In: *Rev. Mod. Phys.* 75 (4 2003), pp. 1333–1382. DOI: 10.1103/RevModPhys.75.1333. URL: https://link.aps.org/doi/10.1103/RevModPhys.75.1333.

[56] Peter Anders et al. "Dynamical mean-field theory for bosons". In: *New Journal of Physics* 13.7 (2011), p. 75013. DOI: 10.1088/1367-2630/13/7/075013. arXiv: 1103.0017. URL: http://stacks.iop.org/1367-2630/13/i=7/a=075013?key=crossref.3a7446115bac89596d0558378e95a2e4{\%}5Cnpapers3://publication/doi/10.1088/1367-2630/13/7/075013.

[57] Ulrich Schollwöck. "The density-matrix renormalization group in the age of matrix product states". In: *Ann. Phys. (N. Y.)* 326.1 (2011). January 2011 Special Issue, pp. 96 –192. ISSN: 0003-4916. DOI: https://doi.org/10.1016/j.aop.2010.09.012. URL: http://www.sciencedirect.com/science/article/pii/S0003491610001752.

[58] A. J. Daley et al. "Time-dependent density-matrix renormalization-group using adaptive effective Hilbert spaces". In: *Journal of Statistical Mechanics: Theory and Experiment* 4 (2004). ISSN: 17425468. DOI: 10.1088/1742-5468/2004/04/P04005. arXiv: 0403313 [cond-mat].

[59] Guifré Vidal. "Efficient Simulation of One-Dimensional Quantum Many-Body Systems". In: *Phys. Rev. Lett.* 93 (4 2004), p. 040502. DOI: 10.1103/PhysRevLett.93.040502. URL: https://link.aps.org/doi/10.1103/PhysRevLett.93.040502.

[60] Guifré Vidal. "Efficient Classical Simulation of Slightly Entangled Quantum Computations". In: *Phys. Rev. Lett.* 91 (14 2003), p. 147902. DOI: 10.1103/PhysRevLett.91.147902. URL: https://link.aps.org/doi/10.1103/PhysRevLett.91.147902.

[61] Steven R. White. "Density matrix formulation for quantum renormalization groups". In: *Phys. Rev. Lett.* 69 (19 1992), pp. 2863–2866. DOI: 10.1103/PhysRevLett.69.2863. URL: https://link.aps.org/doi/10.1103/PhysRevLett.69.2863.

[62] Steven R. White. "Density-matrix algorithms for quantum renormalization groups". In: *Phys. Rev. B* 48 (14 1993), pp. 10345–10356. DOI: 10.1103/PhysRevB.48.10345. URL: https://link.aps.org/doi/10.1103/PhysRevB.48.10345.

[63] Steven R. White and Adrian E. Feiguin. "Real-Time Evolution Using the Density Matrix Renormalization Group". In: *Phys. Rev. Lett.* 93 (7 2004), p. 076401. DOI: 10.1103/PhysRevLett.93.076401. URL: https://link.aps.org/doi/10.1103/PhysRevLett.93.076401.

[64] Giuseppe Carleo and Matthias Troyer. "Solving the quantum many-body problem with artificial neural networks". In: *Science* 355.6325 (2017), pp. 602–606. ISSN: 10959203. DOI: 10.1126/science.aag2302. arXiv: arXiv:1411.3159v1.

[65] A. Öchsner, J. Grácio, and M. Stasiek. "Adsorption and desorption of oxygen at metal-oxide interfaces: Two-dimensional modeling approaches". In: *Journal of Phase Equilibria and Diffusion* 27.6 (2006), pp. 644–650. ISSN: 1863-7345. DOI: 10.1007/BF02736567. URL: https://doi.org/10.1007/BF02736567.

[66] Irina V Belova et al. "The Lattice Monte Carlo Method for Solving Phenomenological Mass and Thermal Diffusion Problems". In: *Diffusion-Fundamentals* 4.Lmc (2007), pp. 13–22. ISSN: 10120386. DOI: 10.4028/www.scientific.net/DDF.279.13.

[67] Irina V. Belova et al. "Lattice-Based Walks and the Monte Carlo Method for Addressing Mass, Thermal and Elasticity Problems". In: *Defect and Diffusion Forum* 283-286.283-286 (2009), pp. 13–23. ISSN: 1662-9507. DOI: 10.4028/www.scientific.net/DDF.283-286.13. URL: http://www.scientific.net/DDF.283-286.13.

[68] M. Suzuki. "Relationship between d-Dimensional Quantal Spin Systems and (d+1)-Dimensional Ising Systems: Equivalence, Critical Exponents and Systematic Approximants of the Partition Function and Spin Correlations". In: *Progress of Theoretical Physics* 56.5 (1976), pp. 1454–1469. ISSN: 1347-4081. DOI: 10.1143/ptp.56.1454. URL: http://dx.doi.org/10.1143/PTP.56.1454.

[69] Dominique Gobert et al. "Real-time dynamics in spin-$\frac{1}{2}$ chains with adaptive time-dependent density matrix renormalization group". In: *Phys. Rev. E* 71 (3 2005), p. 036102. DOI: 10.1103/PhysRevE.71.036102. URL: https://link.aps.org/doi/10.1103/PhysRevE.71.036102.

[70] D. Tamascelli, R. Rosenbach, and M. B. Plenio. "Improved scaling of time-evolving block-decimation algorithm through reduced-rank randomized singular value decomposition". In: *Phys. Rev. E* 91 (6 2015), p. 063306. DOI: 10.1103/PhysRevE.91.063306. URL: https://link.aps.org/doi/10.1103/PhysRevE.91.063306.

[71] C Karrasch, J H Bardarson, and J E Moore. "Reducing the numerical effort of finite-temperature density matrix renormalization group calculations". In: *New J. Phys.* 15.8 (2013), p. 083031. URL: http://stacks.iop.org/1367-2630/15/i=8/a=083031.

[72] D. Belitz and T. R. Kirkpatrick. "The Anderson-Mott transition". In: *Rev. Mod. Phys.* 66 (2 1994), pp. 261–380. DOI: 10.1103/RevModPhys.66.261. URL: https://link.aps.org/doi/10.1103/RevModPhys.66.261.

[73] D.M. Basko, I.L. Aleiner, and B.L. Altshuler. "Metal–insulator transition in a weakly interacting many-electron system with localized single-particle states". In: *Annals of Physics* 321.5 (2006), pp. 1126 –1205. ISSN: 0003-4916. DOI: https://doi.org/10.1016/j.aop.2005.11.014. URL: http://www.sciencedirect.com/science/article/pii/S0003491605002630.

[74] Yevgeny Bar Lev, Guy Cohen, and David R. Reichman. "Absence of Diffusion in an Interacting System of Spinless Fermions on a One-Dimensional Disordered Lattice". In: *Phys. Rev. Lett.* 114 (10 2015), p. 100601. DOI: 10.1103/PhysRevLett.114.100601. URL: https://link.aps.org/doi/10.1103/PhysRevLett.114.100601.

[75] Uri Gavish and Yvan Castin. "Matter-Wave Localization in Disordered Cold Atom Lattices". In: *Phys. Rev. Lett.* 95 (2 2005), p. 020401. DOI: 10.1103/PhysRevLett.95.020401. URL: https://link.aps.org/doi/10.1103/PhysRevLett.95.020401.

[76] N. Y. Yao et al. "Quasi-Many-Body Localization in Translation-Invariant Systems". In: *Phys. Rev. Lett.* 117 (24 2016), p. 240601. DOI: 10.1103/PhysRevLett.117.240601. URL: https://link.aps.org/doi/10.1103/PhysRevLett.117.240601.

[77] Mauro Schiulaz, Alessandro Silva, and Markus Müller. "Dynamics in many-body localized quantum systems without disorder". In: *Phys. Rev. B* 91 (18 2015), p. 184202. DOI: 10.1103/PhysRevB.91.184202. URL: https://link.aps.org/doi/10.1103/PhysRevB.91.184202.

[78] Z. Papić, E. Miles Stoudenmire, and Dmitry A. Abanin. "Many-body localization in disorder-free systems: The importance of finite-size constraints". In: *Annals of Physics* 362 (2015), pp. 714–725. ISSN: 0003-4916. DOI: https://doi.org/10.1016/j.aop.2015.08.024. URL: http://www.sciencedirect.com/science/article/pii/S0003491615003280.

[79] ka, familyi=s., given=Maciej M., giveni=M. M., „ and Katarzyna Czajka. "Thermodynamics of the two-dimensional Falicov-Kimball model: A classical Monte Carlo study". In: *Phys. Rev. B* 74 (3 2006), p. 035109. DOI: 10.1103/PhysRevB.74.035109. URL: https://link.aps.org/doi/10.1103/PhysRevB.74.035109.

[80] L. M. Falicov and J. C. Kimball. "Simple Model for Semiconductor-Metal Transitions: SmB_6 and Transition-Metal Oxides". In: *Phys. Rev. Lett.* 22 (19 1969), pp. 997–999. DOI: 10.1103/PhysRevLett.22.997. URL: https://link.aps.org/doi/10.1103/PhysRevLett.22.997.

[81] U. Brandt and R. Schmidt. "Exact results for the distribution of thef-level ground state occupation in the spinless Falicov-Kimball model". In: *Zeitschrift für Physik B Condensed Matter* 63.1 (1986), pp. 45–53. ISSN: 1431-584X. DOI: 10.1007/BF01312577. URL: https://doi.org/10.1007/BF01312577.

[82] Tom Kennedy and Elliott H. Lieb. "An itinerant electron model with crystalline or magnetic long range order". In: *Physica A: Statistical Mechanics and its Applications* 138.1 (1986), pp. 320–358. ISSN: 0378-4371. DOI: https://doi.org/10.1016/0378-4371(86)90188-3. URL: http://www.sciencedirect.com/science/article/pii/0378437186901883.

[83] Martin Žonda, Pavol Farkašovský, and Hana Čenčariková. "Phase transitions in the three-dimensional Falicov–Kimball model". In: *Solid State Communications* 149.45 (2009), pp. 1997–2001. ISSN: 0038-1098. DOI: https://doi.org/10.1016/j.ssc.2009.08.035. URL: http://www.sciencedirect.com/science/article/pii/S0038109809005328.

[84] Walter Metzner and Dieter Vollhardt. "Correlated Lattice Fermions in $d = \infty$ Dimensions". In: *Phys. Rev. Lett.* 62 (3 1989), pp. 324–327. DOI: 10.1103/PhysRevLett.62.324. URL: https://link.aps.org/doi/10.1103/PhysRevLett.62.324.

[85] U. Brandt and C. Mielsch. "Thermodynamics of the Falicov-Kimball model in large dimensions II". In: *Zeitschrift für Physik B Condensed Matter* 79.2 (1990), pp. 295–299. ISSN: 1431-584X. DOI: 10.1007/BF01406598. URL: https://doi.org/10.1007/BF01406598.

[86] P. G. J. van Dongen. "Exact mean-field theory of the extended simplified Hubbard model". In: *Phys. Rev. B* 45 (5 1992), pp. 2267–2281. DOI: 10.1103/PhysRevB.45.2267. URL: https://link.aps.org/doi/10.1103/PhysRevB.45.2267.

[87] Antoine Georges et al. "Dynamical mean-field theory of strongly correlated fermion systems and the limit of infinite dimensions". In: *Rev. Mod. Phys.* 68 (1 1996), pp. 13–125. DOI: 10.1103/RevModPhys.68.13. URL: https://link.aps.org/doi/10.1103/RevModPhys.68.13.

[88] G. Kotliar et al. "Electronic structure calculations with dynamical mean-field theory". In: *Rev. Mod. Phys.* 78 (3 2006), pp. 865–951. DOI: 10.1103/RevModPhys.78.865. URL: https://link.aps.org/doi/10.1103/RevModPhys.78.865.

[89] Andrey E. Antipov, Emanuel Gull, and Stefan Kirchner. "Critical Exponents of Strongly Correlated Fermion Systems from Diagrammatic Multiscale Methods". In: *Phys. Rev. Lett.* 112 (22 2014), p. 226401. DOI: 10.1103/PhysRevLett.112.226401. URL: https://link.aps.org/doi/10.1103/PhysRevLett.112.226401.

[90] T. Ribic, G. Rohringer, and K. Held. "Nonlocal correlations and spectral properties of the Falicov-Kimball model". In: *Phys. Rev. B* 93 (19 2016), p. 195105. DOI: 10.1103/PhysRevB.93.195105. URL: https://link.aps.org/doi/10.1103/PhysRevB.93.195105.

[91] Walter Kohn. "Theory of the Insulating State". In: *Phys. Rev.* 133 (1A 1964), A171–A181. DOI: 10.1103/PhysRev.133.A171. URL: https://link.aps.org/doi/10.1103/PhysRev.133.A171.

[92] Qimiao Si, Gabriel Kotliar, and Antoine Georges. "Falicov-Kimball model and the breaking of Fermi-liquid theory in infinite dimensions". In: *Phys. Rev. B* 46 (2 1992), pp. 1261–1264. DOI: 10.1103/PhysRevB.46.1261. URL: https://link.aps.org/doi/10.1103/PhysRevB.46.1261.

[93] S. R. Hassan and H. R. Krishnamurthy. "Spectral properties in the charge-density-wave phase of the half-filled Falicov-Kimball model". In: *Phys. Rev. B* 76 (20 2007), p. 205109. DOI: 10.1103/PhysRevB.76.205109. URL: https://link.aps.org/doi/10.1103/PhysRevB.76.205109.

[94] O. P. Matveev, A. M. Shvaika, and J. K. Freericks. "Optical and dc-transport properties of a strongly correlated charge-density-wave system: Exact solution in the ordered phase of the spinless Falicov-Kimball model with dynamical mean-field theory". In: *Phys. Rev. B* 77 (3 2008), p. 035102. DOI: 10.1103/PhysRevB.77.035102. URL: https://link.aps.org/doi/10.1103/PhysRevB.77.035102.

[95] ski, familyi=n., given=Romuald, giveni=R., „ and Klaus Ziegler. "Gapless metallic charge-density-wave phase driven by strong electron correlations". In: *Phys. Rev. B* 89 (7 2014), p. 075104. DOI: 10.1103/PhysRevB.89.075104. URL: https://link.aps.org/doi/10.1103/PhysRevB.89.075104.

[96] K. Binder. "Finite size scaling analysis of ising model block distribution functions". In: *Zeitschrift für Physik B Condensed Matter* 43.2 (1981), pp. 119–140. ISSN: 1431-584X. DOI: 10.1007/BF01293604. URL: https://doi.org/10.1007/BF01293604.

[97] P. DEAN. "The Vibrational Properties of Disordered Systems: Numerical Studies". In: *Rev. Mod. Phys.* 44 (2 1972), pp. 127–168. DOI: 10.1103/RevModPhys.44.127. URL: https://link.aps.org/doi/10.1103/RevModPhys.44.127.

[98] Scott Kirkpatrick and Thomas P. Eggarter. "Localized States of a Binary Alloy". In: *Phys. Rev. B* 6 (10 1972), pp. 3598–3609. DOI: 10.1103/PhysRevB.6.3598. URL: https://link.aps.org/doi/10.1103/PhysRevB.6.3598.

[99] E. Abrahams et al. "Scaling Theory of Localization: Absence of Quantum Diffusion in Two Dimensions". In: *Phys. Rev. Lett.* 42 (10 1979), pp. 673–676. DOI: 10.1103/PhysRevLett.42.673. URL: https://link.aps.org/doi/10.1103/PhysRevLett.42.673.

[100] Krzysztof Byczuk, Walter Hofstetter, and Dieter Vollhardt. "Mott-Hubbard metal-insulator transition at noninteger filling". In: *Phys. Rev. B* 69 (4 2004), p. 045112. DOI: 10.1103/PhysRevB.69.045112. URL: https://link.aps.org/doi/10.1103/PhysRevB.69.045112.

[101] Minh-Tien Tran. "Statistics of local density of states in the Falicov-Kimball model with local disorder". In: *Phys. Rev. B* 76 (24 2007), p. 245122. DOI: 10.1103/PhysRevB.76.245122. URL: https://link.aps.org/doi/10.1103/PhysRevB.76.245122.

[102] M. A. Gusmão. "Phase diagram of the Anderson-Falicov-Kimball model at half filling". In: *Phys. Rev. B* 77 (24 2008), p. 245116. DOI: 10.1103/PhysRevB.77.245116. URL: https://link.aps.org/doi/10.1103/PhysRevB.77.245116.

[103] K. Byczuk et al. "Correlated electrons in the presence of disorder". In: *The European Physical Journal Special Topics* 180.1 (2009), pp. 135–151. ISSN: 1951-6401. DOI: 10.1140/epjst/e2010-01215-2. URL: https://doi.org/10.1140/epjst/e2010-01215-2.

[104] Krzysztof Byczuk, Walter Hofstetter, and Dieter Vollhardt. "ANDERSON LOCALIZATION VS. MOTT–HUBBARD METAL–INSULATOR TRANSITION IN DISORDERED, INTERACTING LATTICE FERMION SYSTEMS". In: *International Journal of Modern Physics B* 24.12n13 (2010), pp. 1727–1755. DOI: 10.1142/S0217979210064575. eprint: https://www.worldscientific.com/doi/pdf/10.1142/S0217979210064575. URL: https://www.worldscientific.com/doi/abs/10.1142/S0217979210064575.

[105] Qimiao Si and Elihu Abrahams. "Strong Correlations and Magnetic Frustration in the High T_c Iron Pnictides". In: *Phys. Rev. Lett.* 101 (7 2008), p. 076401. DOI: 10.1103/PhysRevLett.101.076401. URL: https://link.aps.org/doi/10.1103/PhysRevLett.101.076401.

[106] J. C. Séamus Davis and Dung-Hai Lee. "Concepts relating magnetic interactions, intertwined electronic orders, and strongly correlated superconductivity". In: *Proceedings of the National Academy of Sciences* 110.44 (2013), pp. 17623–17630. ISSN: 0027-8424. DOI: 10.1073/pnas.1316512110. eprint: http://www.pnas.org/content/110/44/17623.full.pdf. URL: http://www.pnas.org/content/110/44/17623.

[107] J. Skolimowski, D. Vollhardt, and K. Byczuk. "Multitude of phases in correlated lattice fermion systems with spin-dependent disorder". In: *ArXiv e-prints* (July 2016). arXiv: 1607.07708 [cond-mat.str-el].

[108] S. Ospelkaus et al. "Localization of Bosonic Atoms by Fermionic Impurities in a Three-Dimensional Optical Lattice". In: *Phys. Rev. Lett.* 96 (18 2006), p. 180403. DOI: 10.1103/PhysRevLett.96.180403. URL: https://link.aps.org/doi/10.1103/PhysRevLett.96.180403.

[109] Laurent Sanchez-Palencia and Maciej Lewenstein. "Disordered quantum gases under control". In: *Nature Physics* 6 (Feb. 2010), 87 EP –. URL: http://dx.doi.org/10.1038/nphys1507.

[110] O. Fialko and K. Ziegler. "Anderson localization in correlated fermionic mixtures". In: *EPL (Europhysics Letters)* 85.6 (2009), p. 60003. URL: http://stacks.iop.org/0295-5075/85/i=6/a=60003.

[111] Gregor Jotzu et al. "Creating State-Dependent Lattices for Ultracold Fermions by Magnetic Gradient Modulation". In: *Phys. Rev. Lett.* 115 (7 2015), p. 073002. DOI: 10.1103/PhysRevLett.115.073002. URL: https://link.aps.org/doi/10.1103/PhysRevLett.115.073002.

[112] Daniel Greif et al. "Formation and Dynamics of Antiferromagnetic Correlations in Tunable Optical Lattices". In: *Phys. Rev. Lett.* 115 (26 2015), p. 260401. DOI: 10.1103/PhysRevLett.115.260401. URL: https://link.aps.org/doi/10.1103/PhysRevLett.115.260401.

[113] C. Ates and K. Ziegler. "Quantum phases in mixtures of Fermionic atoms". In: *Phys. Rev. A* 71 (6 2005), p. 063610. DOI: 10.1103/PhysRevA.71.063610. URL: https://link.aps.org/doi/10.1103/PhysRevA.71.063610.

[114] Ye-Hua Liu and Lei Wang. "Quantum Monte Carlo study of mass-imbalanced Hubbard models". In: *Phys. Rev. B* 92 (23 2015), p. 235129. DOI: 10.1103/PhysRevB.92.235129. URL: https://link.aps.org/doi/10.1103/PhysRevB.92.235129.

[115] Daniel Ueltschi. "Segregation in the Asymmetric Hubbard Model". In: *Journal of Statistical Physics* 116.1 (2004), pp. 681–697. ISSN: 1572-9613. DOI: 10.1023/B:JOSS.0000037231.88815.04. URL: https://doi.org/10.1023/B:JOSS.0000037231.88815.04.

[116] Guifré Vidal and Reinhard F Werner. "Computable measure of entanglement". In: *Phys. Rev. A* 65.3 (2002), p. 032314.

[117] Martin B Plenio. "Logarithmic negativity: a full entanglement monotone that is not convex". In: *Phys. Rev. Lett.* 95.9 (2005), p. 090503.

[118] Martin B. Plenio and Shashank S. Virmani. "An Introduction to Entanglement Theory". In: *Quantum Information and Coherence*. Ed. by Erika Andersson and Patrik Öhberg. Cham: Springer International Publishing, 2014, pp. 173–209. ISBN: 978-3-319-04063-9. DOI: 10.1007/978-3-319-04063-9_8. URL: https://doi.org/10.1007/978-3-319-04063-9_8.

[119] Jens Eisert, Viktor Eisler, and Zoltán Zimborás. "Entanglement negativity bounds for fermionic Gaussian states". In: *Phys. Rev. B* 97 (16 2018), p. 165123. DOI: 10.1103/PhysRevB.97.165123. URL: https://link.aps.org/doi/10.1103/PhysRevB.97.165123.

[120] K. Audenaert et al. "Entanglement properties of the harmonic chain". In: *Phys. Rev. A* 66 (4 2002), p. 042327. DOI: 10.1103/PhysRevA.66.042327. URL: https://link.aps.org/doi/10.1103/PhysRevA.66.042327.

[121] Abolfazl Bayat, Pasquale Sodano, and Sougato Bose. "Negativity as the entanglement measure to probe the Kondo regime in the spin-chain Kondo model". In: *Phys. Rev. B* 81 (6 2010), p. 064429. DOI: 10.1103/PhysRevB.81.064429. URL: https://link.aps.org/doi/10.1103/PhysRevB.81.064429.

[122] Jeongmin Shim, H.-S. Sim, and Seung-Sup B. Lee. "Numerical renormalization group method for entanglement negativity at finite temperature". In: *Phys. Rev. B* 97 (15 2018), p. 155123. DOI: 10.1103/PhysRevB.97.155123. URL: https://link.aps.org/doi/10.1103/PhysRevB.97.155123.

[123] Glen Bigan Mbeng, Vincenzo Alba, and Pasquale Calabrese. "Negativity spectrum in 1D gapped phases of matter". In: *Journal of Physics A: Mathematical and Theoretical* 50.19 (2017). ISSN: 17518121. DOI: 10.1088/1751-8121/aa6734. arXiv: 1612.05172.

[124] J. Eisert, M. Cramer, and M. B. Plenio. "Colloquium: Area laws for the entanglement entropy". In: *Rev. Mod. Phy.* 82.1 (2010), pp. 277–306. DOI: 10.1103/RevModPhys.82.277.

[125] Matthew B Hastings. "An area law for one-dimensional quantum systems". In: *J. Stat. Mech. Theory Exp.* 2007.08 (2007), P08024.

[126] Pasquale Calabrese, John Cardy, and Erik Tonni. "Entanglement Negativity in Quantum Field Theory". In: *Phys. Rev. Lett.* 109 (13 2012), p. 130502. DOI: 10.1103/PhysRevLett.109.130502. URL: https://link.aps.org/doi/10.1103/PhysRevLett.109.130502.

[127] Chia-Min Chung et al. "Entanglement negativity via the replica trick: a quantum Monte Carlo approach". In: *Phys. Rev. B* 90.6 (2014), p. 064401.

[128] Kevin M. O'Connor and William K. Wootters. "Entangled rings". In: *Phys. Rev. A* 63 (5 2001), p. 052302. DOI: 10.1103/PhysRevA.63.052302. URL: https://link.aps.org/doi/10.1103/PhysRevA.63.052302.

[129] M. C. Arnesen, S. Bose, and V. Vedral. "Natural Thermal and Magnetic Entanglement in the 1D Heisenberg Model". In: *Phys. Rev. Lett.* 87 (1 2001), p. 017901. DOI: 10.1103/PhysRevLett.87.017901. URL: https://link.aps.org/doi/10.1103/PhysRevLett.87.017901.

[130] Tobias J. Osborne and Michael A. Nielsen. "Entanglement in a simple quantum phase transition". In: *Phys. Rev. A* 66 (3 2002), p. 032110. DOI: 10.1103/PhysRevA.66.032110. URL: https://link.aps.org/doi/10.1103/PhysRevA.66.032110.

[131] Andreas Osterloh et al. "Scaling of entanglement close to a quantum phase transition". In: *Nature* 416.6881 (2002), pp. 608–610.

[132] Paolo Zanardi and Xiaoguang Wang. "Fermionic entanglement in itinerant systems". In: *J. Phys. A* 35.37 (2002), p. 7947. URL: http://stacks.iop.org/0305-4470/35/i=37/a=307.

[133] J. Eisert and M. B. Plenio. "Introduction to the basics of entanglement theory in continuous-variable systems". In: *eprint arXiv:quant-ph/0312071* (Dec. 2003). eprint: quant-ph/0312071.

[134] M. B. Plenio and S. Virmani. "An introduction to entanglement measures". In: *eprint arXiv:quant-ph/0504163* (Apr. 2005). eprint: quant-ph/0504163.

[135] Ingo Peschel and Viktor Eisler. "Reduced density matrices and entanglement entropy in free lattice models". In: *Journal of Physics A: Mathematical and Theoretical* 42.50 (2009). ISSN: 17518113. DOI: 10.1088/1751-8113/42/50/504003. arXiv: arXiv:0906.1663v3.

[136] Per-Olov Löwdin. "Quantum Theory of Many-Particle Systems. I. Physical Interpretations by Means of Density Matrices, Natural Spin-Orbitals, and Convergence Problems in the Method of Configurational Interaction". In: *Phys. Rev.* 97 (6 1955), pp. 1474–1489. DOI: 10.1103/PhysRev.97.1474. URL: https://link.aps.org/doi/10.1103/PhysRev.97.1474.

[137] Matthew B. Hastings et al. "Measuring Renyi Entanglement Entropy in Quantum Monte Carlo Simulations". In: *Phys. Rev. Lett.* 104 (15 2010), p. 157201. DOI: 10.1103/PhysRevLett.104.157201. URL: https://link.aps.org/doi/10.1103/PhysRevLett.104.157201.

[138] T.-C. Wei et al. "Connections between relative entropy of entanglement and geometric measure of entanglement". In: *eprint arXiv:quant-ph/0405002* (Apr. 2004). eprint: quant-ph/0405002.

[139] S. Friedland and G. Gour. "An explicit expression for the relative entropy of entanglement in all dimensions". In: *Journal of Mathematical Physics* 52.5 (May 2011), pp. 052201–052201. DOI: 10.1063/1.3591132. arXiv: 1007.4544 [quant-ph].

[140] Valerie Coffman, Joydip Kundu, and William K. Wootters. "Distributed entanglement". In: *Phys. Rev. A* 61 (5 2000), p. 052306. DOI: 10.1103/PhysRevA.61.052306. URL: https://link.aps.org/doi/10.1103/PhysRevA.61.052306.

[141] Scott Hill and William K. Wootters. "Entanglement of a Pair of Quantum Bits". In: *Phys. Rev. Lett.* 78 (26 1997), pp. 5022–5025. DOI: 10.1103/PhysRevLett.78.5022. URL: https://link.aps.org/doi/10.1103/PhysRevLett.78.5022.

[142] William K. Wootters. "Entanglement of Formation of an Arbitrary State of Two Qubits". In: *Phys. Rev. Lett.* 80 (10 1998), pp. 2245–2248. DOI: 10.1103/PhysRevLett.80.2245. URL: https://link.aps.org/doi/10.1103/PhysRevLett.80.2245.

[143] Asher Peres. "Separability Criterion for Density Matrices". In: *Phys. Rev. Lett.* 77 (8 1996), pp. 1413–1415. DOI: 10.1103/PhysRevLett.77.1413. URL: https://link.aps.org/doi/10.1103/PhysRevLett.77.1413.

[144] Michał Horodecki, Paweł Horodecki, and Ryszard Horodecki. "Separability of mixed states: necessary and sufficient conditions". In: *Phys. Lett.* 223.1 (1996), pp. 1 –8. ISSN: 0375-9601. DOI: https://doi.org/10.1016/S0375-9601(96)00706-2. URL: http://www.sciencedirect.com/science/article/pii/S0375960196007062.

[145] Charles H. Bennett et al. "Concentrating partial entanglement by local operations". In: *Phys. Rev. A* 53 (4 1996), pp. 2046–2052. DOI: 10.1103/PhysRevA.53.2046. URL: https://link.aps.org/doi/10.1103/PhysRevA.53.2046.

[146] Paola Ruggiero, Vincenzo Alba, and Pasquale Calabrese. "Entanglement negativity in random spin chains". In: *Phys. Rev. B* 94 (3 2016), p. 035152. DOI: 10.1103/PhysRevB.94.035152. URL: https://link.aps.org/doi/10.1103/PhysRevB.94.035152.

[147] Nicholas E. Sherman et al. "Nonzero-temperature entanglement negativity of quantum spin models: Area law, linked cluster expansions, and sudden death". In: *Phys. Rev. E* 93 (2 2016), p. 022128. DOI: 10.1103/PhysRevE.93.022128. URL: https://link.aps.org/doi/10.1103/PhysRevE.93.022128.

[148] K. Audenaert, M. B. Plenio, and J. Eisert. "Entanglement Cost under Positive-Partial-Transpose-Preserving Operations". In: *Phys. Rev. Lett.* 90 (2 2003), p. 027901. DOI: 10.1103/PhysRevLett.90.027901. URL: https://link.aps.org/doi/10.1103/PhysRevLett.90.027901.

[149] Pasquale Calabrese and John Cardy. "Entanglement entropy and quantum field theory". In: *J. Stat. Mech. Theory Exp.* 2004.06 (2004), P06002.

[150] Pasquale Calabrese, John Cardy, and Erik Tonni. "Finite temperature entanglement negativity in conformal field theory". In: *J. Phys. A* 48.1 (2015), p. 015006. URL: http://stacks.iop.org/1751-8121/48/i=1/a=015006.

[151] Paola Ruggiero, Erik Tonni, and Pasquale Calabrese. "Entanglement entropy of two disjoint intervals and the recursion formula for conformal blocks". In: (2018). arXiv: 1805.05975. URL: http://arxiv.org/abs/1805.05975.

[152] Gil Refael and Joel E Moore. "Entanglement entropy of random quantum critical points in one dimension". In: *Phys. Rev. Lett.* 93.26 (2004), p. 260602.

[153] Guifre Vidal et al. "Entanglement in quantum critical phenomena". In: *Phys. Rev. Lett.* 90.22 (2003), p. 227902.

[154] Daniele Binosi et al. "Increasing entanglement through engineered disorder in the random Ising chain". In: *Phys. Rev. B* 76.14 (2007), p. 140405.

[155] Ingo Peschel and Viktor Eisler. "Reduced density matrices and entanglement entropy in free lattice models". In: *J. Phys. A* 42.50 (2009), p. 504003.

[156] Nicholas E. Sherman et al. "Nonzero-temperature entanglement negativity of quantum spin models: Area law, linked cluster expansions, and sudden death". In: *Phys. Rev. E* 93 (2 2016), p. 022128. DOI: 10.1103/PhysRevE.93.022128. URL: https://link.aps.org/doi/10.1103/PhysRevE.93.022128.

[157] Frank Pollmann et al. "Theory of Finite-Entanglement Scaling at One-Dimensional Quantum Critical Points". In: *Phys. Rev. Lett.* 102 (25 2009), p. 255701. URL: https://link.aps.org/doi/10.1103/PhysRevLett.102.255701.

[158] Pasquale Calabrese, John Cardy, and Erik Tonni. "Entanglement entropy of two disjoint intervals in conformal field theory". In: *J. Stat. Mech. Theory Exp.* 2009.11 (2009), P11001. URL: http://stacks.iop.org/1742-5468/2009/i=11/a=P11001.

[159] Pasquale Calabrese, John Cardy, and Erik Tonni. "Entanglement entropy of two disjoint intervals in conformal field theory: II". In: *J. Stat. Mech. Theory Exp.* 2011.01 (2011), P01021. URL: http://stacks.iop.org/1742-5468/2011/i=01/a=P01021.

[160] Ting Yu and JH Eberly. "Sudden death of entanglement". In: *Science* 323.5914 (2009), pp. 598–601.

[161] Muzzamal I Shaukat, Eduardo Castro, Hugo Terças, et al. "Entanglement sudden death and revival in quantum dark-soliton qubits". In: *arXiv:1801.08894* (2018).

[162] Tobias J. Osborne and Michael A. Nielsen. "Entanglement in a simple quantum phase transition". In: *Phys. Rev. A* 66 (3 2002), p. 032110. DOI: 10.1103/PhysRevA.66.032110. URL: https://link.aps.org/doi/10.1103/PhysRevA.66.032110.

[163] Davide Cassi. "Phase transitions and random walks on graphs: A generalization of the Mermin-Wagner theorem to disordered lattices, fractals, and other discrete structures". In: *Phys. Rev. Lett.* 68 (24 1992), pp. 3631–3634. DOI: 10.1103/PhysRevLett.68.3631. URL: https://link.aps.org/doi/10.1103/PhysRevLett.68.3631.

[164] Alessandro Codello and Giulio D'Odorico. "$O(N)$". In: *Phys. Rev. Lett.* 110 (14 2013), p. 141601. DOI: 10.1103/PhysRevLett.110.141601. URL: https://link.aps.org/doi/10.1103/PhysRevLett.110.141601.

[165] Michael E Peskin and Daniel V Schroeder. "Quantum field theory". In: *The Advanced Book Program, Perseus Books Reading, Massachusetts* (1995).

[166] Viktor Eisler and Zoltán Zimborás. "On the partial transpose of fermionic Gaussian states". In: *New J. Phys.* 17.5 (2015), p. 053048. URL: http://stacks.iop.org/1367-2630/17/i=5/a=053048.

[167] Viktor Eisler and Zoltán Zimborás. "Entanglement negativity in two-dimensional free lattice models". In: *Phys. Rev. B* 93 (11 2016), p. 115148. DOI: 10.1103/PhysRevB.93.115148. URL: https://link.aps.org/doi/10.1103/PhysRevB.93.115148.

[168] G. Vidal. "Classical Simulation of Infinite-Size Quantum Lattice Systems in One Spatial Dimension". In: *Phys. Rev. Lett.* 98 (7 2007), p. 070201. DOI: 10.1103/PhysRevLett.98.070201. URL: https://link.aps.org/doi/10.1103/PhysRevLett.98.070201.

[169] C. Karrasch, J. H. Bardarson, and J. E. Moore. "Finite-Temperature Dynamical Density Matrix Renormalization Group and the Drude Weight of Spin-1/2 Chains". In: *Phys. Rev. Lett.* 108 (22 2012), p. 227206. DOI: 10.1103/PhysRevLett.108.227206. URL: https://link.aps.org/doi/10.1103/PhysRevLett.108.227206.

[170] Steven R. White. "Minimally Entangled Typical Quantum States at Finite Temperature". In: *Phys. Rev. Lett.* 102 (19 2009), p. 190601. DOI: 10.1103/PhysRevLett.102.190601. URL: https://link.aps.org/doi/10.1103/PhysRevLett.102.190601.

[171] Thomas Barthel, Ulrich Schollwöck, and Steven R. White. "Spectral functions in one-dimensional quantum systems at finite temperature using the density matrix renormalization group". In: *Phys. Rev. B* 79 (24 2009), p. 245101. DOI: 10.1103/PhysRevB.79.245101. URL: https://link.aps.org/doi/10.1103/PhysRevB.79.245101.

[172] N. D. Mermin and H. Wagner. "Absence of Ferromagnetism or Antiferromagnetism in One- or Two-Dimensional Isotropic Heisenberg Models". In: *Phys. Rev. Lett.* 17 (22 1966), pp. 1133–1136. DOI: 10.1103/PhysRevLett.17.1133. URL: https://link.aps.org/doi/10.1103/PhysRevLett.17.1133.

[173] David A. Huse et al. "Localization-protected quantum order". In: *Phys. Rev. B* 88.1 (2013), p. 014206. ISSN: 1098-0121. DOI: 10.1103/PhysRevB.88.014206. URL: http://link.aps.org/doi/10.1103/PhysRevB.88.014206https://link.aps.org/doi/10.1103/PhysRevB.88.014206.

[174] Jonas A. Kjäll, Jens H. Bardarson, and Frank Pollmann. "Many-Body Localization in a Disordered Quantum Ising Chain". In: *Phys. Rev. Lett.* 113 (10 2014), p. 107204. DOI: 10.1103/PhysRevLett.113.107204. URL: http://link.aps.org/doi/10.1103/PhysRevLett.113.107204.

[175] Anushya Chandran et al. "Many-body localization and symmetry-protected topological order". In: *Phys. Rev. B* 89 (14 2014), p. 144201. DOI: 10.1103/PhysRevB.89.144201. URL: https://link.aps.org/doi/10.1103/PhysRevB.89.144201.

[176] Bela Bauer and Chetan Nayak. "Area laws in a many-body localized state and its implications for topological order". In: *J. Stat. Mech. Theor. Exp.* 09 (2013). URL: http://stacks.iop.org/1742-5468/2013/i=09/a=P09005.

[177] David Pekker et al. "Hilbert-Glass Transition: New Universality of Temperature-Tuned Many-Body Dynamical Quantum Criticality". In: *Phys. Rev. X* 4 (1 2014), p. 011052. DOI: 10.1103/PhysRevX.4.011052. URL: https://link.aps.org/doi/10.1103/PhysRevX.4.011052.

[178] Yasaman Bahri et al. "Localization and topology protected quantum coherence at the edge of hot matter". In: *Nat. Comm.* 6 (2015), p. 7341. URL: http://dx.doi.org/10.1038/ncomms8341.

[179] S. A. Parameswaran, Andrew C. Potter, and Romain Vasseur. "Eigenstate phase transitions and the emergence of universal dynamics in highly excited states". In: *Ann. Phys. (Berl.)* 529.7 (2017), p. 1600302. ISSN: 00033804. DOI: 10.1002/andp.201600302. URL: http://arxiv.org/abs/1610.03078http://dx.doi.org/10.1002/andp.201600302http://doi.wiley.com/10.1002/andp.201600302.

[180] I. V. Gornyi, A. D. Mirlin, and D. G. Polyakov. "Interacting Electrons in Disordered Wires: Anderson Localization and Low-T Transport". In: *Phys. Rev. Lett.* 95 (20 2005), p. 206603. DOI: 10.1103/PhysRevLett.95.206603. URL: http://link.aps.org/doi/10.1103/PhysRevLett.95.206603.

[181] , familyi=v., given=Marko, giveni=M., „ Toma ž Prosenek, familyi=v., given=Peter, giveni=P., „ and. "Many-body localization in the Heisenberg XXZ magnet in a random field". In: *Phys. Rev. B* 77 (6 2008), p. 064426. DOI: 10.1103/PhysRevB.77.064426. URL: https://link.aps.org/doi/10.1103/PhysRevB.77.064426.

[182] Jens H. Bardarson, Frank Pollmann, and Joel E. Moore. "Unbounded Growth of Entanglement in Models of Many-Body Localization". In: *Phys. Rev. Lett.* 109 (1 2012), p. 017202. DOI: 10.1103/PhysRevLett.109.017202. URL: http://link.aps.org/doi/10.1103/PhysRevLett.109.017202.

[183] Ehud Altman and Ronen Vosk. "Universal dynamics and renormalization in many body localized systems". In: *Annu. Rev. Condens. Matter Phys.* 6.1 (2014), pp. 383–409. ISSN: 1947-5454. DOI: 10.1146/annurev-conmatphys-031214-014701. URL: www.annualreviews.orghttp://www.annualreviews.org/doi/10.1146/annurev-conmatphys-031214-014701http://arxiv.org/abs/1408.2834http://dx.doi.org/10.1146/annurev-conmatphys-031214-014701.

[184] David J. Luitz, Nicolas Laflorencie, and Fabien Alet. "Many-body localization edge in the random-field Heisenberg chain". In: *Phys. Rev. B* 91 (8 2015), p. 081103. DOI: 10.1103/PhysRevB.91.081103. URL: http://link.aps.org/doi/10.1103/PhysRevB.91.081103.

[185] Soumya Bera et al. "Many-Body Localization Characterized from a One-Particle Perspective". In: *Phys. Rev. Lett.* 115 (4 2015), p. 046603. DOI: 10.1103/PhysRevLett.115.046603. URL: http://link.aps.org/doi/10.1103/PhysRevLett.115.046603.

[186] Yevgeny Bar Lev, Guy Cohen, and David R. Reichman. "Absence of Diffusion in an Interacting System of Spinless Fermions on a One-Dimensional Disordered Lattice". In: *Phys. Rev. Lett.* 114 (10 2015), p. 100601. DOI: 10.1103/PhysRevLett.114.100601. URL: https://link.aps.org/doi/10.1103/PhysRevLett.114.100601.

[187] Soumya Bera et al. "Density Propagator for Many-Body Localization: Finite-Size Effects, Transient Subdiffusion, and Exponential Decay". In: *Phys. Rev. Lett.* 118 (19 2017), p. 196801. DOI: 10.1103/PhysRevLett.118.196801. URL: https://link.aps.org/doi/10.1103/PhysRevLett.118.196801.

[188] Fabien Alet and Nicolas Laflorencie. "Many-body localization: an introduction and selected topics". In: (2017). arXiv: 1711.03145. URL: http://arxiv.org/abs/1711.03145.

[189] A. Smith et al. "Disorder-Free Localization". In: *Phys. Rev. Lett.* 118 (26 2017), p. 266601. DOI: 10.1103/PhysRevLett.118.266601. URL: https://link.aps.org/doi/10.1103/PhysRevLett.118.266601.

[190] A. Smith et al. "Absence of Ergodicity without Quenched Disorder: From Quantum Disentangled Liquids to Many-Body Localization". In: *Phys. Rev. Lett.* 119 (17 2017), p. 176601. DOI: 10.1103/PhysRevLett.119.176601. URL: https://link.aps.org/doi/10.1103/PhysRevLett.119.176601.

[191] Marlon Brenes et al. "Many-Body Localization Dynamics from Gauge Invariance". In: *Phys. Rev. Lett.* 120 (3 2018), p. 030601. DOI: 10.1103/PhysRevLett.120.030601. URL: https://link.aps.org/doi/10.1103/PhysRevLett.120.030601.

[192] Michael Schreiber et al. "Observation of many-body localization of interacting fermions in a quasirandom optical lattice". In: *Science* 349.6250 (2015), pp. 842–845. ISSN: 0036-8075. DOI: 10.1126/science.aaa7432.

[193] M. Ovadia et al. "Evidence for a Finite-Temperature Insulator". In: *Sci. Rep.* 5 (2015), 13503 EP–. URL: http://dx.doi.org/10.1038/srep13503.

[194] J. Smith et al. "Many-body localization in a quantum simulator with programmable random disorder". In: *Nat. Phys.* advance online publication (2016). ISSN: 1745-2481. URL: http://dx.doi.org/10.1038/nphys3783.

[195] Jae yoon Choi et al. "Exploring the many-body localization transition in two dimensions". In: *Science* 352.6293 (2016), pp. 1547–1552. ISSN: 0036-8075. DOI: 10.1126/science.aaf8834.

[196] Pranjal Bordia et al. "Coupling Identical one-dimensional Many-Body Localized Systems". In: *Phys. Rev. Lett.* 116 (14 2016), p. 140401. DOI: 10.1103/PhysRevLett.116.140401. URL: http://link.aps.org/doi/10.1103/PhysRevLett.116.140401.

[197] A. Lukin et al. "Probing entanglement in a many-body-localized system". In: *ArXiv e-prints* (May 2018). arXiv: 1805.09819 [cond-mat.quant-gas].

[198] Zhang J. et al. "Observation of a discrete time crystal". In: *Nature* 543 (2017), p. 217. DOI: 10.1038/nature21413.

[199] Choi Soonwon et al. "Observation of discrete time-crystalline order in a disordered dipolar many-body system". In: *Nature* 543 (2017), p. 221. DOI: 10.1038/nature21426.

[200] K. Binder and A. P. Young. "Spin glasses: Experimental facts, theoretical concepts, and open questions". In: *Rev. Mod. Phys.* 58 (4 1986), pp. 801–976. DOI: 10.1103/RevModPhys.58.801. URL: https://link.aps.org/doi/10.1103/RevModPhys.58.801.

[201] Pierre Pfeuty. "The one-dimensional Ising model with a transverse field". In: *Ann. Phys.* 57.1 (1970), pp. 79 –90. ISSN: 0003-4916. DOI: https://doi.org/10.1016/0003-4916(70)90270-8. URL: http://www.sciencedirect.com/science/article/pii/0003491670902708.

[202] Ulrich Schollwöck. "The density-matrix renormalization group in the age of matrix product states". In: *Ann. Phys.* 326.1 (2011), pp. 96 –192. ISSN: 0003-4916. DOI: https://doi.org/10.1016/j.aop.2010.09.012. URL: http://www.sciencedirect.com/science/article/pii/S0003491610001752.

[203] M. Suzuki. "Relationship between d-Dimensional Quantal Spin Systems and (d+1)-Dimensional Ising Systems: Equivalence, Critical Exponents and Systematic Approximants of the Partition Function and Spin Correlations". In: *Progr. Theor. Phys.* 56.5 (1976), pp. 1454–1469. ISSN: 1347-4081. DOI: 10.1143/ptp.56.1454. URL: http://dx.doi.org/10.1143/PTP.56.1454.

[204] See supplemental material for further numerical details, and convergence tests of the eigenstate order.

[205] Ronen Vosk and Ehud Altman. "Many-Body Localization in One Dimension as a Dynamical Renormalization Group Fixed Point". In: *Phys. Rev. Lett.* 110 (6 2013), p. 067204. DOI: 10.1103/PhysRevLett.110.067204. URL: https://link.aps.org/doi/10.1103/PhysRevLett.110.067204.

[206] Philipp Hauke et al. "Probing entanglement in adiabatic quantum optimization with trapped ions". In: *Frontiers in Physics* 3 (2015), p. 21. DOI: 10.3389/fphy.2015.00021. URL: https://www.frontiersin.org/article/10.3389/fphy.2015.00021.

[207] Tobias Graß et al. "Quantum annealing for the number-partitioning problem using a tunable spin glass of ions". In: *Nat. Commun.* 7 (2016), p. 11524. URL: http://dx.doi.org/10.1038/ncomms11524http://10.0.4.14/ncomms11524.

[208] R. Blatt and C. F. Roos. "Quantum simulations with trapped ions". In: *Nat. Phys.* 8.4 (2012), pp. 277–284. ISSN: 17452473. DOI: 10.1038/nphys2252. eprint: 0905.0118.

[209] P. Jurcevic et al. "Quasiparticle engineering and entanglement propagation in a quantum many-body system". In: *Nature* 511.7508 (2014), pp. 202–205. ISSN: 0028-0836. URL: http://dx.doi.org/10.1038/nature13461.

[210] R. Barends et al. "Digitized adiabatic quantum computing with a superconducting circuit". In: *Nature* 534 (2016), p. 222. URL: http://dx.doi.org/10.1038/nature17658.

[211] L. A. Pena Ardila, Markus Heyl, and Andre Eckardt. In: *In preparation* ().

[212] B. P. Lanyon et al. "Universal Digital Quantum Simulation with Trapped Ions". In: *Science* 334 (2011), p. 57. DOI: 10.1126/science.1208001.

[213] E. A. Martinez et al. "Real-time dynamics of lattice gauge theories with a few-qubit quantum computer". In: *Nature* 534 (May 2016), p. 516. DOI: 10.1038/nature18318. URL: http://tinyurl.sfx.mpg.de/uqgk.

[214] J. Zhang et al. "Observation of a discrete time crystal". In: *Nature* 543.7644 (2017), pp. 217–220. ISSN: 14764687. DOI: 10.1038/nature21413. arXiv: 1609.08684.

[215] N. Y. Yao et al. "Discrete Time Crystals: Rigidity, Criticality, and Realizations". In: *Phys. Rev. Lett.* 118 (3 2017), p. 030401. DOI: 10.1103/PhysRevLett.118.030401. URL: https://link.aps.org/doi/10.1103/PhysRevLett.118.030401.

[216] Vedika Khemani et al. "Phase Structure of Driven Quantum Systems". In: *Phys. Rev. Lett.* 116 (25 2016), p. 250401. DOI: 10.1103/PhysRevLett.116.250401. URL: https://link.aps.org/doi/10.1103/PhysRevLett.116.250401.

[217] Achilleas Lazarides, Arnab Das, and Roderich Moessner. "Equilibrium states of generic quantum systems subject to periodic driving". In: *Phys. Rev. E* 90 (1 2014), p. 012110. DOI: 10.1103/PhysRevE.90.012110. URL: https://link.aps.org/doi/10.1103/PhysRevE.90.012110.

[218] Achilleas Lazarides, Arnab Das, and Roderich Moessner. "Fate of Many-Body Localization Under Periodic Driving". In: *Phys. Rev. Lett.* 115 (3 2015), p. 030402. DOI: 10.1103/PhysRevLett.115.030402. URL: https://link.aps.org/doi/10.1103/PhysRevLett.115.030402.

[219] Dominique Gobert et al. "Real-time dynamics in spin-$\frac{1}{2}$ chains with adaptive time-dependent density matrix renormalization group". In: *Phys. Rev. E* 71 (3 2005), p. 036102. DOI: 10.1103/PhysRevE.71.036102. URL: https://link.aps.org/doi/10.1103/PhysRevE.71.036102.

Declaration of Authorship

Erklärung:

Hiermit versichere ich, Younes JAVANMARD, dass ich die vorliegende Arbeit ohne unzuläßige Hilfe Dritter und ohne Benutzung anderer als der angegebenen Hilfsmittel angefertigt habe; die aus fremden Quellen direkt oder indirekt übernommenen Gedanken sind als solche kenntlich gemacht. Die Arbeit wurde bisher weder im Inland noch im Ausland in gleicher oder ähnlicher Form einer anderen Prüfungsbehörde vorgelegt.

Diese Arbeit wurde unter der wissenschaftlichen Betreuung von Prof. Dr. Jens H. Bardarson und Prof. Dr. Roderich Moessner am Max-Planck Institut für Physik komplexer Systeme in Dresden angefertigt. Ich erkläre hiermit, dass keine früheren erfolglosen Promotionsverfahren stattgefunden haben. Ich erkenne die Promotionsordnung der Fakultät für Mathematik und Naturwissenschaften der Technische Universität Dresden an.

Unterschrift:

Dresden, den: